(NASA-CR-135129) LASER ABSORPTION PHENOMENA
IN FLOWING GAS DEVICES Final Technical
Report (Avco-Everett Research Lab.) 125 p
HC A06/MF A01 CSCL 20E

N78-18411

Unclas
G3/36 15152

LASER ABSORPTION PHENOMENA
IN FLOWING GAS DEVICES

FINAL TECHNICAL REPORT

P.K. Chapman and J.H. Otis

Contract No. NAS3-18559
June 1976

prepared for

NASA-LEWIS RESEARCH CENTER
21000 Brookpark Road
Cleveland, Ohio 44135

AVCO EVERETT RESEARCH LABORATORY, INC.

A SUBSIDIARY OF AVCO CORPORATION

LASER ABSORPTION PHENOMENA IN FLOWING GAS DEVICES

FINAL TECHNICAL REPORT

by

P. K. Chapman and J. H. Otis

AVCO EVERETT RESEARCH LABORATORY, INC.
a Subsidiary of Avco Corporation
Everett, Massachusetts 02149

Contract No. NAS3-18559

June 1976

prepared for

NASA-LEWIS RESEARCH CENTER
21000 Brookpark Road
Cleveland, Ohio 44135

ABSTRACT

A theoretical and experimental investigation is presented of inverse Bremsstrahlung absorption of CW CO_2 laser radiation (wavelength $10.6\,\mu$m) in flowing gases seeded with alkali metals. In order to motivate this development, some simple models are described of several space missions which could use laser-powered rocket vehicles. Design considerations are given for a test cell to be used with the Avco Everett Research Laboratory, Inc., HPL-10 welding laser, using a diamond window for admission of laser radiation at power levels in excess of 10 kW. A detailed analysis of absorption conditions in the test cell is included. The experimental apparatus and test set-up are described and the results of experiments presented. Injection of alkali seedant and steady-state absorption of the laser radiation were successfully demonstrated, but problems with the durability of the diamond windows at higher powers prevented operation of the test cell as an effective laser-powered thruster. Improved designs for diamond window holders are now available and should be used in future experiments of this type.

TABLE OF CONTENTS

LIST OF ILLUSTRATIONS

I. INTRODUCTION: THE CONCEPT OF LASER PROPULSION

At the present time, rocket propulsion systems for space applications may be divided into two categories: (1) conventional chemical rocket engines, which typically exhibit specific impulses in the range of 270 to 400 seconds; and (2) low thrust engines (e. g., electric propulsion systems), which have intrinsically high specific impulses, of the order of thousands of seconds. For many space missions the optimum combination of mass ratio efficiency and energy efficiency requires a specific impulse lying between these extremes.

As a particular example, the present high cost of launch to earth orbit is due in large part to the fact that the engines employed exhibit specific impulses which are considerably less than optimum. The consequent high mass ratios are important not so much because of the high propellant utilization per pound of payload but because quite sophisticated boost vehicle structure is required if there is to be a positive payload.

When the mission permits, one useful approach to the problem of reducing vehicle costs is to provide for the recovery, refurbishment and multiple reuse of one or more stages. This is, of course, the approach taken in the space shuttle, in which the basic vehicle construction cost is not lower than that of present launch vehicles but is intended to be amortized over a relatively large number (approximately 100) of missions.

A different but perhaps complementary attack on this problem is to reduce the mass ratio by increasing the thrust generated per unit mass of propellant expended. A method of this type which has often been considered (for example in studies of the aerospace plane) is the use of an air breathing booster, which, in principle, avoids the mass penalty of carrying oxidizer in the boost stage. The engineering complexities involved have, however, impeded the practical utilization of this system, at least for space launch applications.

The concept of laser propulsion, as proposed originally by Kantrowitz et al.[1,2] represents a new departure which, if shown to be feasible, could provide a major improvement in the economics of space operations.[3] In boost application of this system, a powerful ground based laser is the power source for the vehicle, which rides up the beam, obtaining propulsive thrust from laser induced breakdown and heating of a working fluid.

At first sight the most significant feature of this system is that the energy source for boost remains on the ground. It should be noted, however, that in conventional propulsion systems the cost of the (chemical) energy required for boost (i. e., direct fuel cost) is relatively small. More important advantages of laser propulsion are that the choice of working fluid for

propulsion is not constrained by the requirements of chemical combustion, and that the temperatures reached in laser-induced breakdown are typically much higher than in combustion. Use of a high operating temperature and a propellant of low molecular weight should allow the achievement of a much higher exhaust velocity: it may in fact be possible to tailor the specific impulse to the mission under consideration.

In designing a laser powered thruster for a given mission, use of an excessively high specific impulse exacts penalties in terms of the laser power requirements and in the overall energy efficiency of the system, as well as possibly introducing design problems for the engine itself. Furthermore, since the cost of the propellants themselves will generally be a small component of the total mission cost, the primary purpose of a low mass ratio is to minimize the structural complexity of the vehicle. It may be preferable to use a propellant which is dense and readily storeable (e. g. water) rather than one of minimum molecular weight (e. g. , liquid hydrogen), even at the expense of some increase in overall mass ratio. As discussed in Section II these considerations will generally lead to a mass ratio which is in excess of about 2.5, regardless of the mission. The structural materials and techniques employed in such a vehicle may nevertheless be more closely analogous to those in conventional aircraft construction than to present launch vehicle practice and it is this which offers the greatest opportunity for cost reductions.

The principal price paid for the remarkable potential performance of the laser propulsion system is that, to a larger extent than with conventional vehicles, the entire launch operation must be tackled from an integrated systems viewpoint. For example, the boost must be completed while the vehicle is within range of the laser station, taking into account laser propagation characteristics in the atmosphere, a fact which may constrain the boost trajectory. For any given mission the range limitation also may impose a lower limit on the acceleration employed and hence directly affect the required thrust of the engine. Further, since the exhaust power of any rocket propulsion system is proportional to the product of thrust and exhaust velocity, the range limit, due to beamspread as well as atmospheric absorption, can directly influence the power output required from the ground-based laser. Present indications are that the trade off between vehicle performance and laser power favors a capital intensive system in which the major part of the required investment is devoted to the laser and associated power supply. It thus appears that laser propulsion is particularly appropriate to high volume boost applications in which the cost per launch is a more significant factor than the capital investment: this characteristic is shared with the shuttle.

Another area in which laser propulsion may offer important advantages is that of orbit to orbit transfer. At least three different approaches to this problem are conceivable:

1. Direct laser irradiation from the ground of an engine aboard a spacecraft whose orbit passes near the laser station.

Using receiving optics deployed in space, this system could be applied to spacecraft having perigee altitudes up to at least 500 kilometers, but there are serious constraints, depending upon the latitude of the laser station, on both the initial orbits which are applicable and the final orbits which can be achieved.

2.   Use of a mirror in an orbit which passes over the laser station to redirect the radiation to a spacecraft at a longer range. This system relaxes somewhat the orbital constraints but narrows the available burn windows. A variant of this technique which may eventually prove useful consists of a focussing mirror which is itself in a geosynchronous orbit and which redirects the radiation to an ascending interorbital tug. The feasibility of this system depends on minimizing the laser beamspread due to atmospheric effects. In order that a mirror in geosynchronous orbit be a reasonable size (less than 100 meters in diameter) the beamspread must be of the order of a microradian. Adaptive optic techniques may perhaps be capable of approaching this performance, [4] compensating for turbulent degradation of the beam and thermal blooming in the atmosphere.

3.   Use of a laser station which is itself in orbit. Since in this approach the entire system is outside the atmosphere, the range at which laser propulsion is feasible depends only on the diffraction limit of the output optics and the size of the receiving optics. This approach clearly offers much greater flexibility. For example, a high power laser in geosynchronous orbit could be used, not only to bring up an orbital tug from low orbit to synchronous orbit, but to inject deep space vehicles to interplanetary trajectories. As in the case of launch from Earth, the advantages of this system are, firstly, that the mass of the power generating system for each vehicle does not have to be lifted through the gravitational potential, and, secondly, that the specific impulse of the engine employed can be tailored to the mission at hand. Determination of the cost-optimum specific impulse for orbit-to-orbit applications requires consideration of the cost of bringing propellants from earth to low orbit as well as of capital costs such as that of the laser station. If the space shuttle is used for the Earth launch phase, it is expected that the optimum for geosynchronous missions will be somewhat in excess of a thousand seconds, giving relatively short transfer times to synchronous orbit (up to several days), together with a tug mass ratio which is less than 2. A system of this type may become particularly attractive if and when a major solar power station is established in space.

Most of the mission analyses which have been carried out to date at AERL, Inc., have been concerned with launch from Earth to orbit. In order to motivate the design of the test cell which is discussed in this report,

some simple analyses of this type are sketched in Section II. Orbit-to-orbit applications have been considered elsewhere[5] The physics of absorption of laser radiation in flowing gases is considered in Section III, leading to the specification of design parameters for the test cell. Development of the test cell itself together with supporting instrumentation is discussed in Section IV and the results of experiments carried out are given in Section V.

II. BOOST APPLICATIONS OF LASER PROPULSION

1. BACKGROUND

In both the military and civilian sectors of the national space program, one of the greatest challenges of this decade is the reduction of the costs associated with space operations such as launch to low orbit, orbit-to-orbit transfer, etc. While it is true that, at present, direct operational costs are often a relatively small fraction of the total cost of a given space mission (for example, payload hardware costs frequently exceed launch costs by more than an order of magnitude), reduction of the basic cost of transportation to space can have a disproportionate influence in improving the overall economics of space flight programs.

It should be noted at the outset that space flight is not an inherently expensive operation. The energy which must be imparted to a pound of payload to place it in low orbit is less than 4 kWh, which is an order of magnitude less than the energy consumed in carrying a pound of payload around the world in a jet transport aircraft. In principle, operations involving launch to and recovery from low orbit are energetically cheaper than long-haul aircraft operations. If the energy required to orbit could be obtained from a ground-based electric utility and applied efficiently, the cost would be in the vicinity of 10 ¢ per pound of payload. The difference between this figure and present launch costs (> $800/lb) is one measure of the improvements which are conceptually possible in the technology of space flight.

The range of activities which are economically feasible in space is a very sensitive function of launch costs. At present, the utilization of space consists almost entirely of the gathering and transmission of information, using reconnaissance, communication, navigation and geodetic, meteorological, Earth resources survey, and scientific satellites. The reason for this is simply that information is one of the few commodities whose value per pound is high enough to justify the current space transportation costs. The development of economical launch and recovery systems will allow a major increase in the scope and utility of information services from space (e.g., commercial direct-broadcast television, quick-look reconnaissance in tactical military situations, etc.), but such services will then be only a part of the exploitation of the unique resources of the virgin territory of Earth orbit. As one example, interest in space will broaden to include such areas as the manufacture in free fall of materials and components for terrestrial systems.

The expansion of space activities which will follow reduction in launch costs has very significant implications for the overall cost-effectiveness of the program. In the first place, when mission opportunities

are few, it is necessary that the probability of success on a given mission be high, and system costs are, of course, a very steeply increasing function of the required reliability. There will always be space missions (e.g., those for which the launch windows are narrow and infrequent) and particular spacecraft subsystems (e.g., safety-critical systems on manned missions) which demand high reliability, but, for the great majority of routine space operations, the cost-effectiveness trade will shift in the direction of replacement or repair of defective systems when chea and simple access to orbit is available. This can provide an opportunity for very substantial reductions in payload costs.

Secondly, the payloads for space missions now consist primarily of complex and costly instrumentation. In the future, there will be a requirement for many payloads which are intrinsically far less expensive, including structural materials for space stations and other large orbital assemblies, and bulk cargo such as consumables for logistic support, materials for space manufacturing operations, and fuel for orbit-to-orbit tugs. This factor alone is sufficient to ensure that average payload costs will decrease dramatically with launch costs.

Thirdly, economies of scale will become effective as launch costs are lowered. Most spacecraft are now special-purpose systems and their development costs must be amortized over a very few missions. Further, the number of units produced is often too small to allow the learning curve to affect manufacturing costs. The economies from this source following an increase in the frequency of mission opportunities can be enhanced by a modular approach to the design of spacecraft systems, a trend which is just now beginning: an example is NASA's Small Astronomy Satellite, a basic bus vehicle which provides control, orientation, command and telemetry facilities for a variety of instrumentation on different missions.

The importance of ready access to space is recognized in the current U.S. commitment to the development of the space shuttle, a vehicle which should reduce direct launch costs to between $160 and $350 per pound of payload, depending on the utilization of the vehicle and the nature of the mission. The shuttle also offers additional opportunities for reducing payload costs: (1) it provides a benign launch environment, which may simplify payload instrumentation; (2) it will provide personnel for on-orbit checkout, erection, deployment and, if necessary, repair of satellite systems, or for operation of equipment in the payload bay; and (3) it will, in many cases, allow the recovery, refurbishment and multiple reuse of satellite payloads.

While the shuttle should provide a major improvement in the cost-effectiveness of space operations, economically viable shuttle payloads will remain, for the foreseeable future, limited to relatively high-value items. In order to allow the broad expansion of space activities which is required if the full potential of space technology is to be realized (and which is in fact required to justify the development costs of the shuttle itself), what is needed is a cheap and effective means of placing in orbit those payloads which are of lower intrinsic value. Space operations cannot become a routine part of

the economic life of this country, nor can space technology play its full part in the defense of the free world, until a launch system is available offering direct costs well below $100 per pound.

The concept of laser propulsion offers the remarkable possibility of launch to orbit using ground-based power. The purpose of this section is to discuss the mission performance aspects of a laser powered launch vehicle, on the assumption that the engine design problems can be solved. As will be shown, a laser powered launch vehicle must be considered as being, not competitive with the shuttle, but complementary to it. Extrapolation of the state-of-the-art in laser design indicates that payloads to orbit of order several tons are not unreasonable, but that provision of a much heavier lift capability than this would require an excessive capital investment in the laser station, and might also encounter laser propagation limitations in the atmosphere. Thus the earliest potential space application of laser propulsion appears to be in the unmanned launch of relatively small payloads. It is fortunate that many of the lower-value payloads for which a cheap launch capability is necessary fall into this category. Freed from the need to be used as a freight vehicle the shuttle can then be used for those higher-value payloads for which its direct launch costs are not prohibitive. It is also possible that the down cargo capability of the shuttle could be used effectively as a means of returning the boost engines and other components of the laser powered launch vehicles for refurbishment and reuse. The laser powered launch system and the shuttle appear to be adapted to complementary mission functions, providing the possibility of an overall launch capability which is much more cost-effective than could be achieved with either system alone.

2. RECTILINEAR BOOST TO ESCAPE

In conventional chemical rocket boosters, the efficiency with which the energy of the fuel and oxidizer is converted into kinetic energy of the vehicle is usually only of indirect interest, a more important criterion of performance being efficiency in the utilization of propellant mass. Similarly, the power in the exhaust of the engine is usually only significant in terms of losses and attendant cooling problems. The reason for this situation is that the chemical energy of typical propellants is cheap (a few cents per kilowatt hour) compared to other elements of the system, but the specific impulse obtainable from them is low (< 450 seconds, in vacuum), which requires multi-stage vehicles for launch to orbital velocity, with high overall mass ratios and sophisticated structural design.

The design of a laser-powered boost vehicle for launch to Earth orbit requires, first of all, a specification of the required exhaust velocity (or range of exhaust velocities), as this will determine the operating temperature of the engine and strongly affect design of the concentrator and of

the window for admission of received laser radiation to the thrust chamber.
The costs associated with laser powered boost depend also on: (i) the ex-
haust power P of the engine, as this is proportional to the laser power and
hence fixes the capital cost of the laser installation; (ii) the energy expended
during boost, which determines the laser gas processing cost, the cost of
electrical energy consumed by the laser, and some other items such as the
refurbishment costs of the laser power supply capacitor bank; (iii) the mass
ratio of the vehicle, which affects most strongly its required structural
sophistication and the fraction of the mass at burnout which is payload; and
(iv) the choice of working fluid for the engine. All these parameters depend
on the exhaust velocity program which is used.

In order to form an estimate of the required exhaust power and spe-
cific impulse in an operational laser-powered boost engine, we consider
here first the problem of acceleration from rest to escape velocity along a
rectilinear trajectory. It is assumed that the thrust axis of the engine is
aligned with the trajectory; i.e., none of the thrust is used to support the
component of weight of the vehicle normal to the trajectory. Apart from
simplicity, the principal rationale for this condition is that in more realistic
trajectories, to sub-escape velocities, a gravity turn can actually effect
a useful rotation of the velocity vector, raising the perigee of the orbit
which is achieved, so there is little to be gained from investigating means
for counteracting it.

Neglecting losses, the exhaust power of the engine is (see glossary
for definition of symbols, page 111).

$$P = -1/2 \, \dot{m} \, c^2 \tag{II-1}$$

and the equation of motion along the trajectory is, neglecting aerodynamic
drag,

$$ma = m(\dot{v} + g_{\parallel}) = -\dot{m} \, c = \frac{2P}{c} \tag{II-2}$$

where the right hand side is obtained from Eq. (II-1). Here

$$g_{\parallel} = g \cos \gamma \tag{II-3}$$

is the instantaneous component of gravitation along the trajectory. If the
Earth were flat, $g_{\parallel}$ would be constant along a rectilinear trajectory, but
the ranges to be considered here are sufficient to require taking into account
the effects of variations in the direction and magnitude of gravitation along
some such trajectories.

In order to minimize the exhaust power P it is desirable to make
$g_{\parallel}$ as small as possible, reducing the gravity losses while permitting as
leisurely an ascent as range constraints will allow. For a rectilinear tra-
jectory, the flight path angle γ should be as large as possible: the max-
imum feasible value is expected to be in the vicinity of 60°, due to atmo-
spheric absorption of the laser radiation at high zenith angles.

In accelerating along a rectilinear trajectory away from the Earth, the flight path angle decreases with time due to the change in direction of the local vertical, and this effect can offset the reduction in gravitational force with altitude. Figure II-1 shows the component of g along the trajectory as a function of range, for various initial flight path angles γ_0 (the curves are derived in Appendix A). Fortuitously, $g_{\parallel}$ is almost constant out to ranges of several thousand kilometers, if $\gamma_0 \approx 60°$.

For the best possible rectilinear trajectory, we therefore take

$$g_{\parallel} \approx g_0 \cos 60 = 1/2\, g_0 = \text{constant} \tag{II-4}$$

The absolute minimum value of P can be obtained by setting up a variational problem based on Eq. (II-2) which yields the power-optimal acceleration program. [6] This results in an acceleration which increases linearly with time, but the power savings effected in this way are generally minor and are obtained at the expense of requiring significantly higher exhaust velocities than in the case to be considered here, in which, to simplify engine design, c is assumed constant. With this constraint, Eq. (II-2) gives

$$\frac{\dot{m}}{m} = -\frac{1}{c}\,(v + g_{\parallel}) \tag{II-5}$$

or, integrating,

$$\ln \frac{m}{m_0} = \frac{1}{c}\,(v + g_{\parallel}\, t) \tag{II-6}$$

In particular, the mass ratio is given by

$$R_1 = \frac{m_0}{m_1} = \exp\left[\frac{v_1 + g_{\parallel}\,\tau}{c}\right] \tag{II-7}$$

The duration τ of boost may also be found from Eq. (II-2):

$$-\int_0^\tau \dot{m}\,dt = m_0 - m_1 = m_1(R_1 - 1) = \frac{2P}{c^2}\,\tau = \frac{m_1 a_1 \tau}{c} \tag{II-8}$$

or

$$\tau = \frac{c}{a_1}\,(R_1 - 1) \tag{II-9}$$

so that Eq. (II-7) may be written as

$$\ln R_1 = \frac{v_1}{c} + \frac{g_{\parallel}}{a_1}\,(R_1 - 1) \tag{II-10}$$
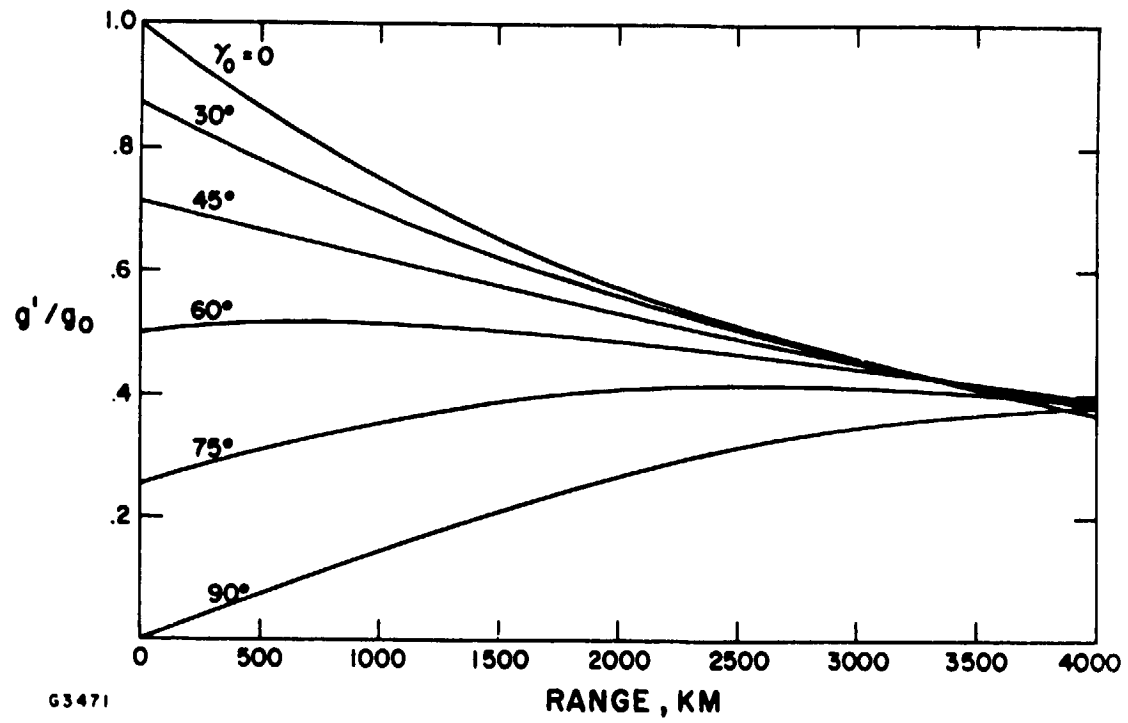
Fig. II-1   Tangential g Component, Rectilinear Trajectories

G3471

The exhaust velocity required to give a mass ratio R_1 is thus

$$c = \frac{v_1 \hat{a}_1}{\hat{a}_1 \ln R_1 - R_1 + 1} \qquad (\text{II-11})$$

where

$$\hat{a}_1 = a_1 / g_{\parallel} \qquad (\text{II-12})$$

the range ρ_1 covered during boost may be found by noting that, if P and c are constant, so is $\dot{m}$, so that

$$m = m_o + \dot{m}\tau = m_o(1 - t/\tau_o) \qquad (\text{II-13})$$

where

$$\tau_o = \frac{-m_o}{\dot{m}} = \frac{R_1 m_1 c^2}{2P} = \frac{R_1 c}{a_1} \qquad (\text{II-14})$$

Equation (II-6) may thus be written

$$v = \frac{d\rho}{dt} = -g_{\parallel} t - c \ln(1 - t/\tau_o) \qquad (\text{II-15})$$

or; integrating,

$$\rho_1 = -1/2 \, g_{\parallel} \, \tau^2 - c \int_0^\tau \ln(1 - t/\tau_o) \, dt$$

$$= -1/2 \, g_{\parallel} \, \tau^2 + c \, \tau_o \, [1 + (1 - t/\tau_o)(\ln(1 - t/\tau_o) - 1)]$$

$$= -1/2 \, g_{\parallel} \, \tau^2 + \frac{c \, \tau_o}{R_1} [R_1 - \ln R_1 - 1] \qquad (\text{II-16})$$

from Eq. (II-13) at $t = \tau$. Also, from Eq. (II-13),

$$\tau_o = \tau \frac{R_1}{R_1 - 1} \qquad (\text{II-17})$$

and, from Eq. (II-7)

$$c = (v_1 + g_{||} \tau)/\ln R_1. \qquad (II-18)$$

Inserting these in Eq. (II-16) gives

$$\rho_1 = \frac{v_1(R_1 - \ln R_1 - 1)\,\tau}{(R - 1)\ln R} + 1/2\; g_{||}\; \tau^2 \left[\frac{2(R_1 - \ln R_1 - 1}{(R_1 - 1)\ln R_1} - 1 \right] \qquad (II-19)$$

It is convenient to normalize this equation by writing

$$\hat{\tau} = \frac{\tau\, g_{||}}{v_1} \qquad (II-20)$$

$$\hat{\rho}_1 = \frac{2\, g_{||}}{v_1^2}\, \rho_1 \qquad (II-21)$$

which gives

$$\left[\frac{2(R_1 - \ln R_1 - 1)}{(R_1 - 1)\ln R_1} - 1 \right] \tau^2 + \frac{2(R_1 - \ln R_1 - 1)}{(R_1 - 1)\ln R_1}\, \hat{\tau} - \hat{\rho}_1 = 0 \qquad (II-22)$$

With the value of $\hat{\tau}$ obtained from this equation, the specific exhaust power (i.e., the exhaust power divided by the mass of the vehicle at burnout) may be obtained from Eq. (II-14):

$$\frac{P}{m_1} = \frac{R_1\, c^2}{2\, \tau_o} = \frac{(R_1 - 1)\, c^2}{2\, \tau} = \frac{(R_1 - 1)\,(v_1 + g_{||}\, \tau)^2}{2\, \tau \ln^2 R_1}$$

$$= 1/2\; v_1\, g_{||}\, \frac{(R_1 - 1)\,(1 + \hat{\tau})^2}{\hat{\tau} \ln^2 R_1} \qquad (II-23)$$

These equations allow the specific exhaust power to be calculated as a function of range and mass ratio if the final velocity v_1 is specified. If, however, the mission is to escape velocity, then v_1 is a function of ρ_1.

Specifically, since (for $\gamma_o = 60°$) the geocentric radius at ρ_1 is (see Appendix A)

$$r_1 = \sqrt{r_o^2 + \rho_1^2 + \rho_1 r_o} \qquad (II-24)$$

the escape velocity there is given by

$$v_1^2 = \frac{2 g_o r_o^2}{\sqrt{r_o^2 + \rho_1^2 + \rho_1 r_o}}$$

(II-25)

Inserting this in Eq. (II-21),

$$\hat{\rho}_1 = \frac{g_{\parallel}}{g_o} \left(\frac{\rho_1}{r_o}\right) \left[1 + \frac{\rho_1}{r_o} + \left(\frac{\rho_1}{r_o}\right)^2\right]^{1/2} \approx \frac{1}{2} \left(\frac{\rho_1}{r_o}\right) \left[1 + \frac{\rho_1}{r_o} + \left(\frac{\rho_1}{r_o}\right)^2\right]^{1/2}$$

(II-26)

Before using these results to calculate the power requirements, notice that, for any given mass ratio, there is a maximum range for which boost is possible. In the first place, real solutions of Eq. (II-22) for $\hat{\tau}$ exist only if

$$\hat{\rho}_1 \leq \frac{q^2}{1 - 2q}$$

(II-27)

where

$$q = \frac{R_1 - \ln R_1 - 1}{(R_1 - 1) \ln R_1}$$

(II-28

The physical significance of this effect will be seen after considering another possible range limit. From Eqs. (II-9), (II-20) and (II-18)

$$\hat{\tau} = \frac{g_{\parallel}}{v_1} \frac{c}{a_1} (R_1 - 1) = g_{\parallel} \frac{(1 + \hat{\tau})(R_1 - 1)}{a_o R_1 \ln R_1}$$

(II-29)

From Eq. (II-2), the lift-off acceleration will be zero when $a_o = g_{\parallel}$. Under this condition, Eq. (II-29) gives

$$\hat{\tau} = \frac{R_1 - 1}{R_1 \ln R_1 - R_1 + 1}$$

(II-30)

This expression can now be used in Eq. (II-22) to calculate the maximum value of $\hat{\rho}_1$ for which the lift-off acceleration is positive. The results are shown in Fig. II-2, in the curve labeled "lift-off limit". If the range for boost is greater than this at a given mass ratio, the equation of motion permits a maneuver in which the vehicle falls back until its mass decreases sufficiently for the acceleration to become positive, but this will not generally be an acceptable departure technique. In any case, if the
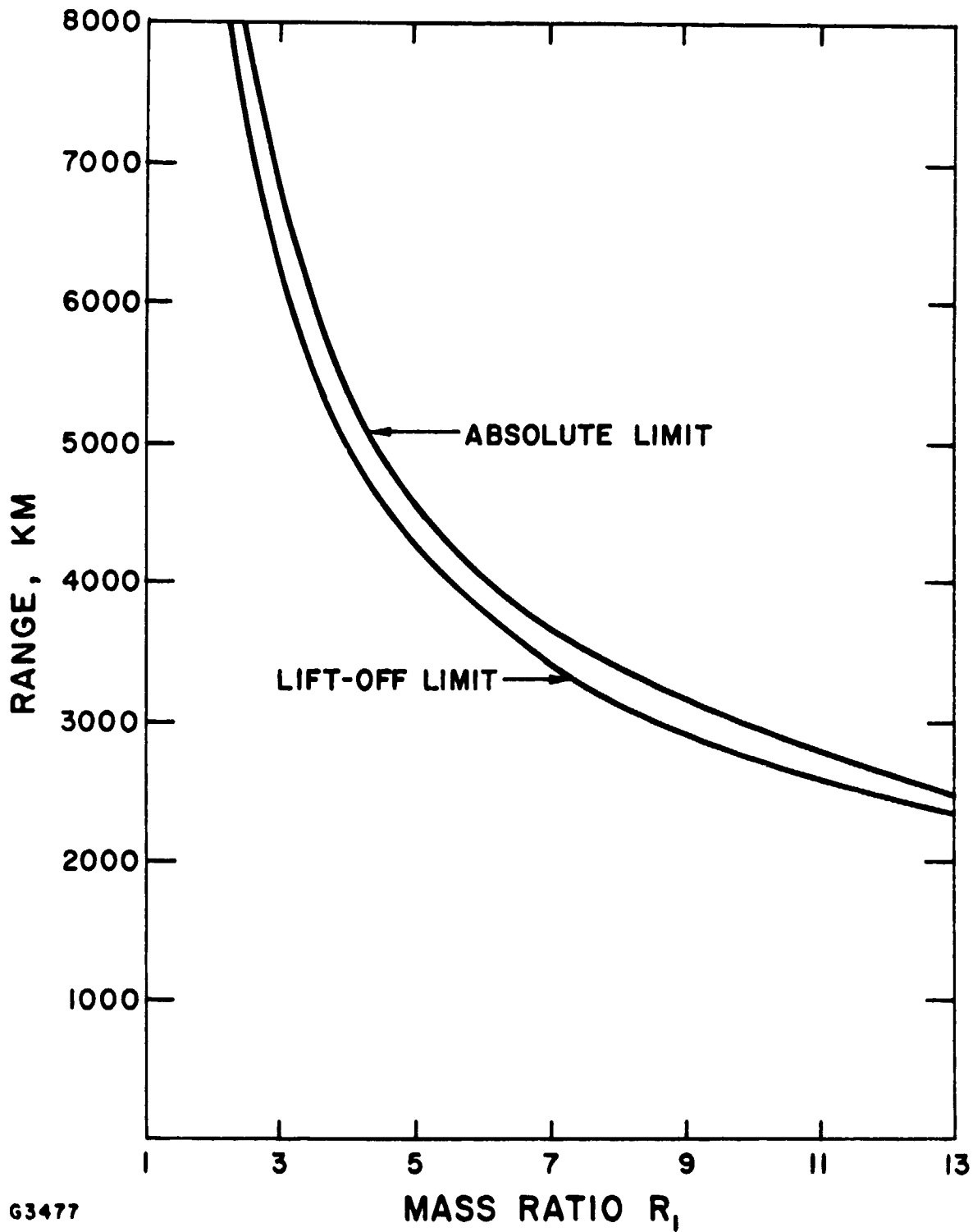
Fig. II-2   Limiting Range vs Mass Ratio for Rectilinear Launch to Escape

range for boost is too great, it becomes impossible to overcome the initial negative acceleration and reach the required velocity within the specified mass ratio, and this is the meaning of the limit (Eq. (II-27)). The range implied by this equation is also shown as a function of mass ratio in Fig. II-2, where it is labeled "absolute limit".

In general, these range limits are too large to be of practical significance in launch to escape velocity, except perhaps at very high mass ratios.

Figure II-3 shows the specific exhaust power required as a function of the mass ratio, for several ranges. Note that mass ratios below about 2.5 or 3 exact a considerable power penalty, but the curves are quite flat for higher mass ratios.

The specific exhaust power is shown as a function of the range traversed during boost for mass ratios of 3 and 5 in Fig. II-4. The range for minimum power is 3000 to 4000 km. At shorter ranges, the power is higher because the boost duration is shorter; at longer ranges, gravity losses exact an increasing penalty as the average acceleration decreases.

The specific impulse which is needed for given range and mass ratio may be calculated from Eq. (II-18). The results are shown in Fig. II-5 for ranges of 500 km and 2000 km, bracketing the probable values required in an operational system.

The conclusions which may be drawn from this analysis are as follows:

1. For rectilinear launch-to-escape, the mass ratio of the vehicle should be larger than 3, so as to minimize both the exhaust power and specific impulse requirements.

2. The specific impulse needed will generally be less than 1200 seconds.

3. The range during boost should be as large as possible, probably between 1000 and 3000 km. The feasibility of operating at ranges of this order is under study[6], but discussion of the requirements (adaptive laser output optics, engine collector design, etc.) is beyond the scope of the present report.

4. It is possible to launch to escape a vehicle weighing one metric ton using an exhaust power of about 300 MW, but specific powers of 400 - 500 MW/ton will probably be required when all design compromises (mass ratio, specific impulse, range, etc.) have been made.
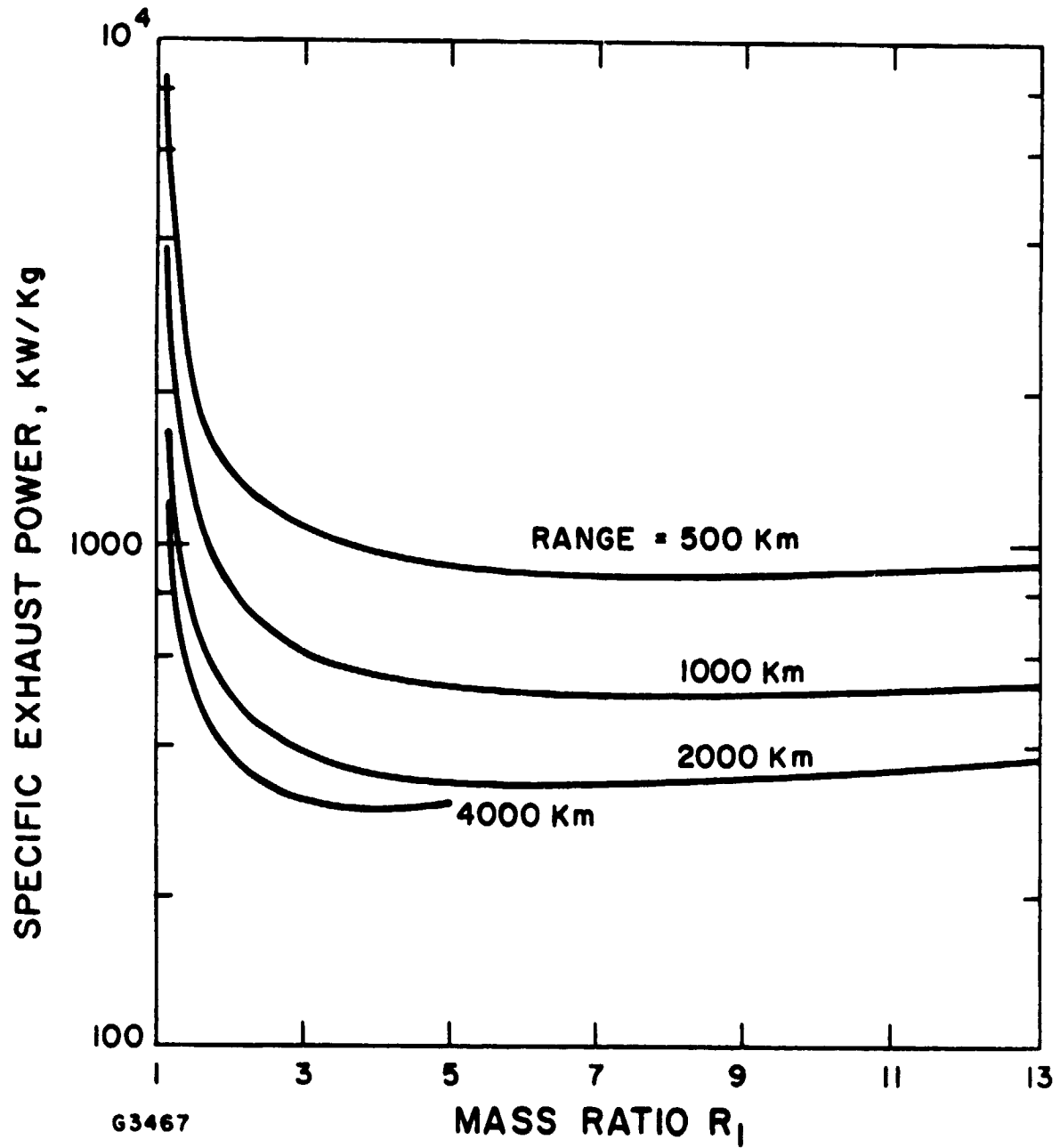
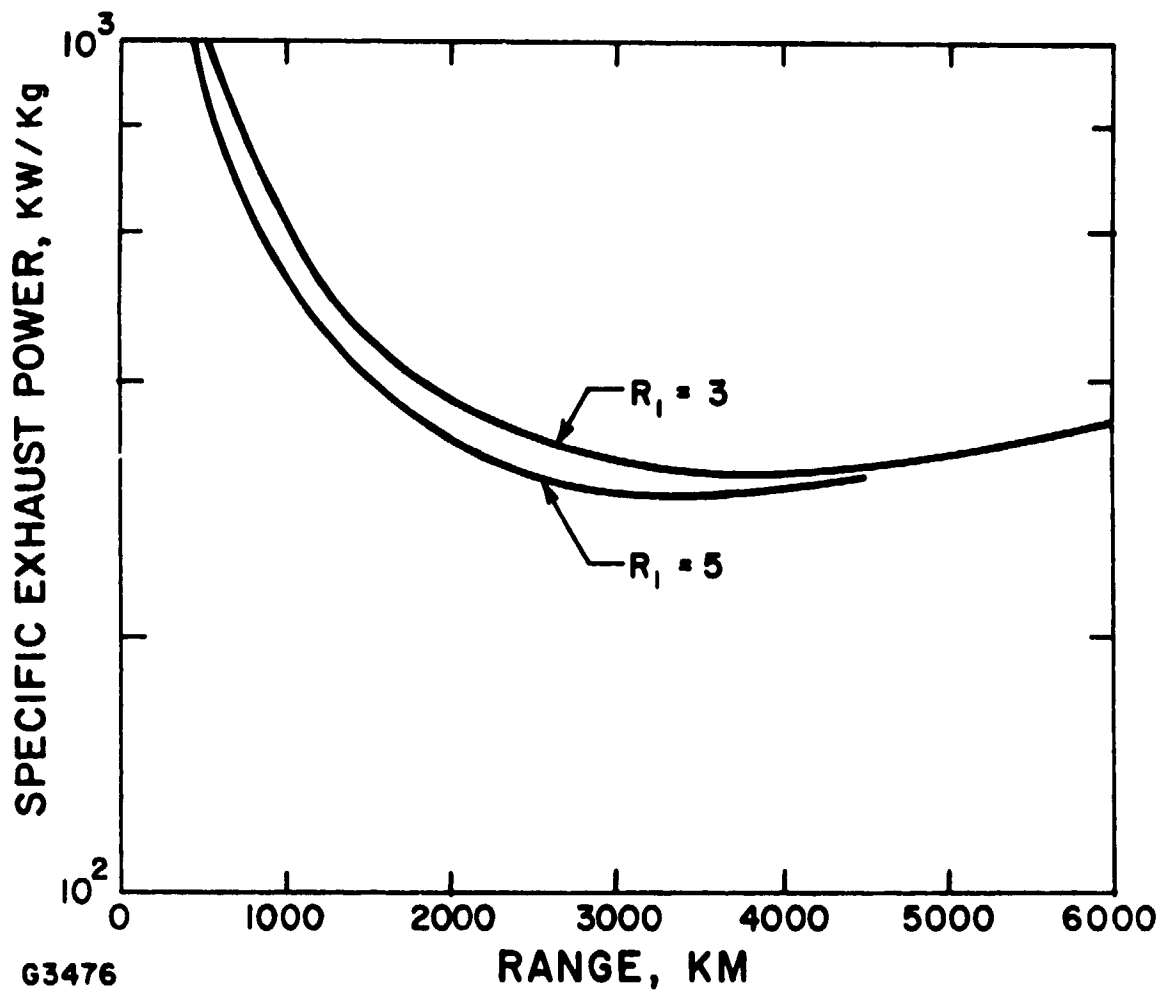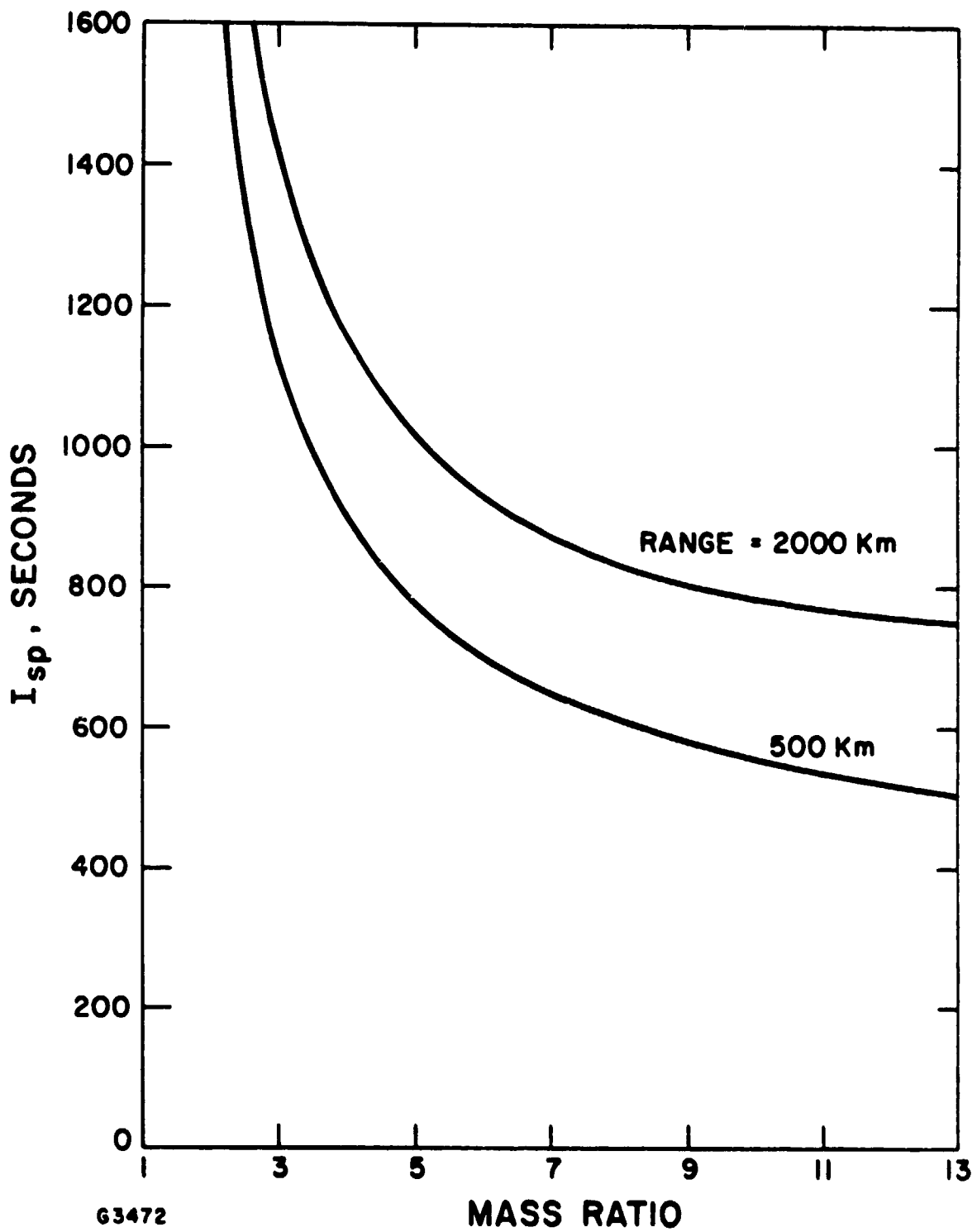Fig. II-3   Power Requirements for Launch to Escape

Fig. II-4   Exhaust Power vs Range for Launch to Escape

G3476

-17-

Fig. II-5   Specific Impulse vs Mass Ratio, Rectilinear Launch to Escape

Launch to escape is, of course, one of the most demanding missions for which range-limited, laser-powered boost might be used. Launch to low orbit, requiring lower final velocity, is expected to require considerably less power and lower specific impulse.

3. RECTILINEAR BOOST TO ORBITAL VELOCITY

In order to display as simply as possible the lower power and specific impulse requirements associated with launch to orbit, consider again the rectilinear boost problem of the previous section, but assume that the velocity to be reached at range ρ_1 is the minimum velocity which, at that point, will give an orbit with a perigee radius greater than the radius of the Earth. In other words, Eq. (II-25) is to be replaced by the vis viva integral[7] for an orbit of apogee radius r_1 and perigee r_0:

$$V_1^2 = \mu \left(\frac{2}{r_1} - \frac{2}{r_1 + r_0} \right) = 2\mu \frac{r_0}{r_1(r_1 + r_0)} \tag{II-31}$$

where r_1 is given as a function of the range ρ_1 by Eq. (II-24).

This procedure ignores the problem that if the vehicle at burnout is to be at apogee of its subsequent orbit, the velocity there must be perpendicular to the local vertical. However, a gravity turn and/or the use of thrust can rotate the velocity vector in more realistic ascent trajectories, and the present analysis gives a simple lower bound to the mission requirements.

Using Eq. (II-31) in Eq. (II-21) gives

$$\hat{\rho}_1 = \frac{2 g_{\parallel}}{2 g_0 r_0^3} (r_1 + r_0) r_1 \rho_1 \approx \frac{g_{\parallel}}{g_0} \left[\left(\frac{r_1}{r_0} \right) + 1 \right] \left(\frac{r_1}{r_0} \right) \left(\frac{\rho_1}{r_0} \right)$$

$$\approx \frac{1}{2} \left(\frac{\rho_1}{r_0} \right) \left[1 + \left(\frac{\rho_1}{r_0} \right) + \left(\frac{\rho_1}{r_0} \right)^2 \right]^{1/2} \left[\left(1 + \left(\frac{\rho_1}{r_0} \right) + \left(\frac{\rho_1}{r_0} \right)^2 \right)^{1/2} + 1 \right]$$

$$\tag{II-32}$$

There is again an absolute limiting range at which it is possible to reach the velocity required by the mission, at a given mass ratio. The value is obtained by solving Eq. (II-32) for ρ_1 using Eq. (II-27) for ρ_1. There is also again a slightly more stringent range limit, based on requiring a positive lift-off acceleration, which is obtained by using Eq. (II-30) in Eq. (II-22) to give ρ_{11} and then solving Eq. (II-32). The results are shown in Fig. II-6. The limits are more practically significant than in the case of launch-to-escape: this type of effect could provide a lower bound to the power required to launch to orbit at constant specific impulse, even when more realistic trajectories are used.
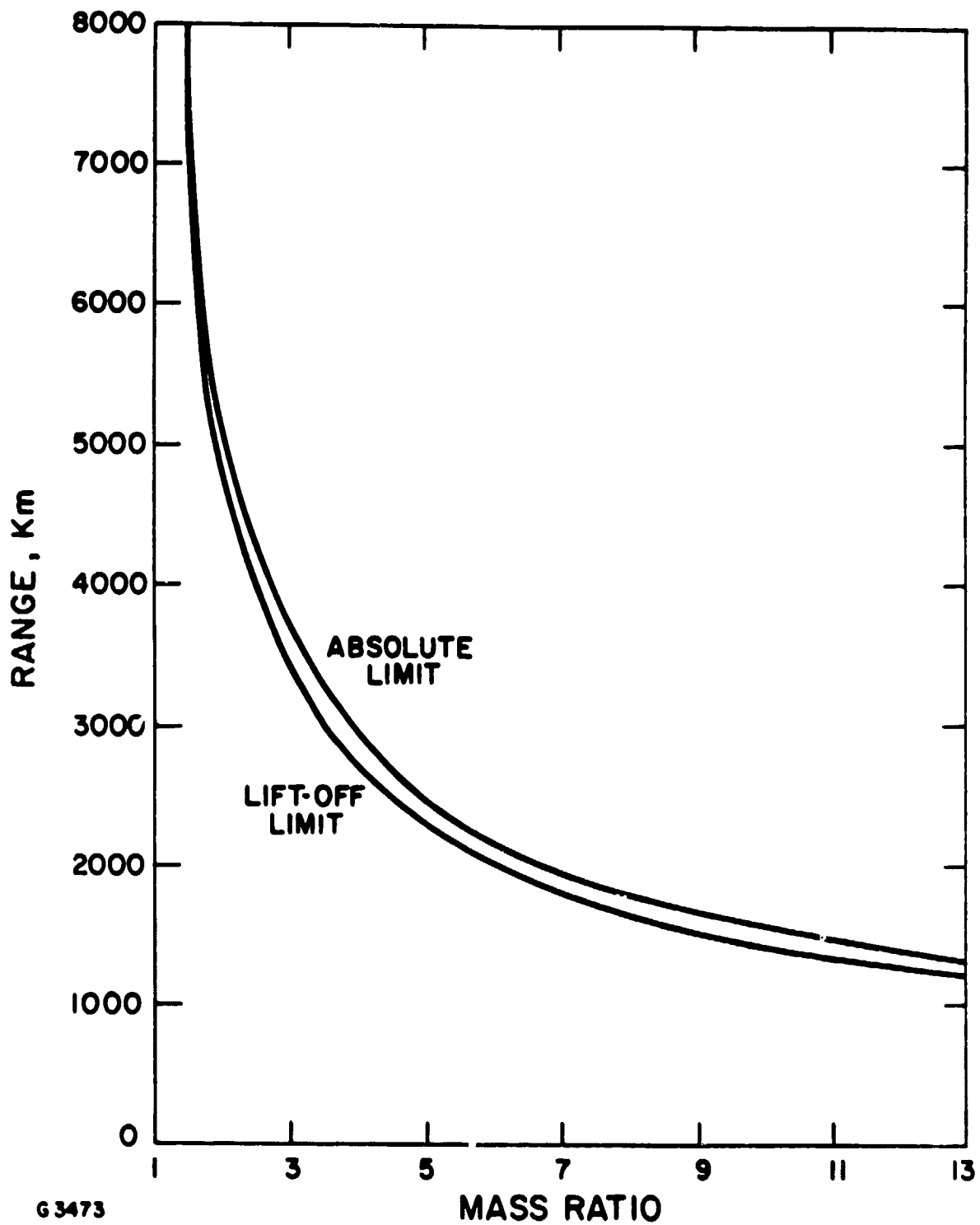
Fig. II-6 Limiting Range vs Mass Ratio for Rectilinear Launch to Orbital Velocity

G 3473

The value of ρ_1 from Eq. (II-30) may now be used in Eq. (II-22) to give the normalized time for boost, and then Eqs. (II-23) and (II-18), give the specific exhaust power and specific impulse. As shown in Fig. II-7, the power requirements exhibit the steep rise below a mass ratio of about three which was found in the case of escape, but comparison with Fig. II-3 shows that the power requirements for launch to orbit, for a given range and mass ratio, are about a factor of three lower than for escape.

The exhaust power is shown as a function of range in Fig. II-8. In general (except at very low mass ratios) the curves do not reach the minimum before the range limit of Fig. II-6 is met.

Finally, the specific impulse required is shown as a function of the mass ratio for two different ranges in Fig. II-9. As is to be expected, lower exhaust velocities are needed for this less demanding mission.

While much work remains to be done to obtain realistic laser-powered ascent trajectories to orbit, it appears that exhaust powers of the order of 100 MW for each metric ton of payload may be feasible, and that a specific impulse of less than 800 seconds will be adequate.

4. LAUNCH-TO-ORBIT AT CONSTANT SPECIFIC FORCE

We consider here a specific trajectory for launch-to-Earth orbit. The purpose of this analysis is only to demonstrate that ascent trajectories to stable orbit meeting constraints imposed by laser propulsion can be found, and to derive preliminary estimates of the exhaust power and exhaust velocity which would be required. As will be shown, it is possible to complete orbital insertion within a range of the laser station which is small compared to the radius of the Earth and it is therefore an adequate first approximation to assume that the Earth is flat.

The trajectory to be studied consists, firstly, of a vertical ascent to an altitude y_1 and velocity v_1. At this point the vehicle pitches through 90° and thrusts horizontally until orbital velocity is achieved.

To simplify the analysis further, it is assumed that the laser-powered engine delivers a constant specific force throughout the ascent. The variation in exhaust velocity and mass flow rate required to give this result is readily found from the equation of motion Eq. (II-2), (repeated here for convenience)

$$ma = -\dot{m}c = \frac{2P}{c} \tag{II-33}$$

If a is constant

$$mc = \frac{2P}{a} = \text{constant} \tag{II-34}$$
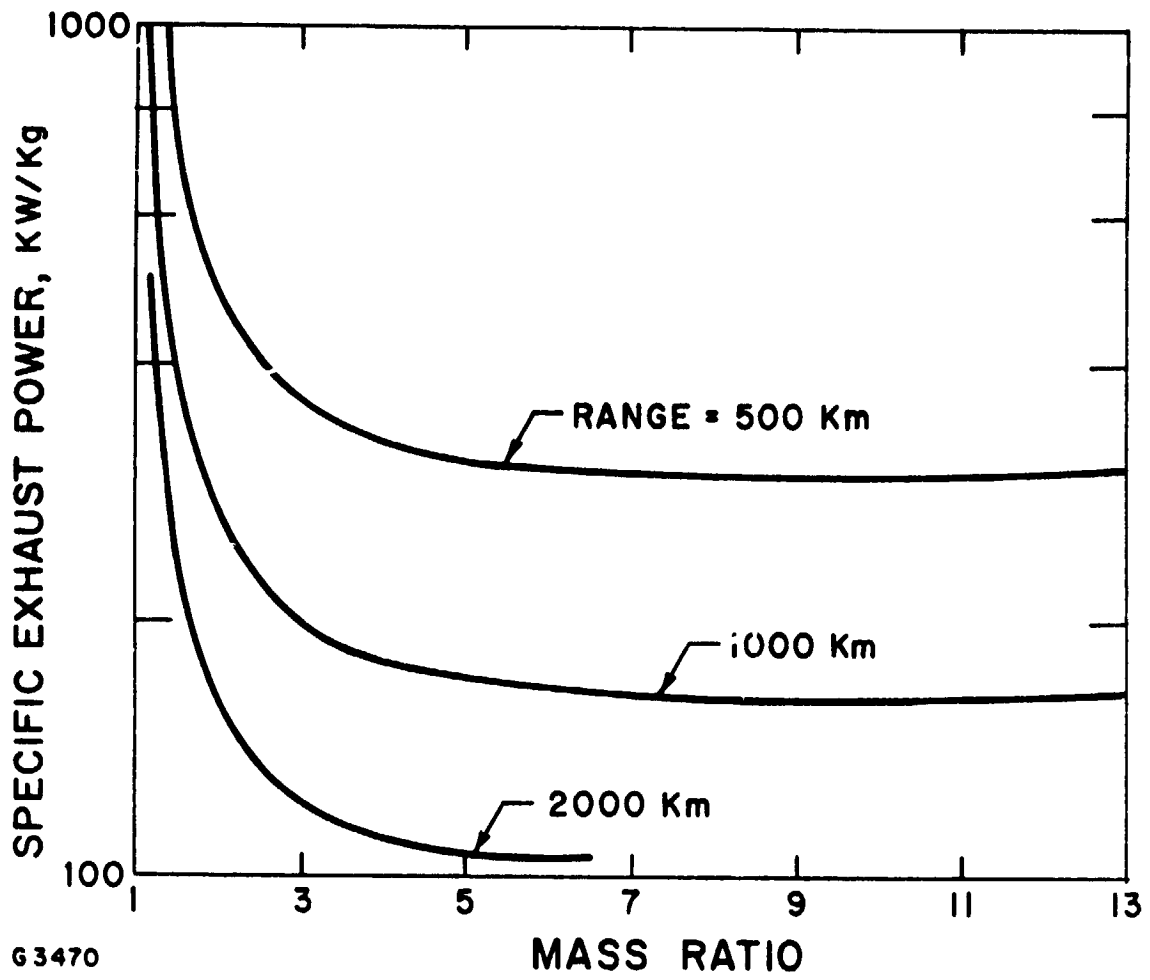
Fig. II-7   Power Requirements for Rectilinear Launch to Orbital Velocity

G3470
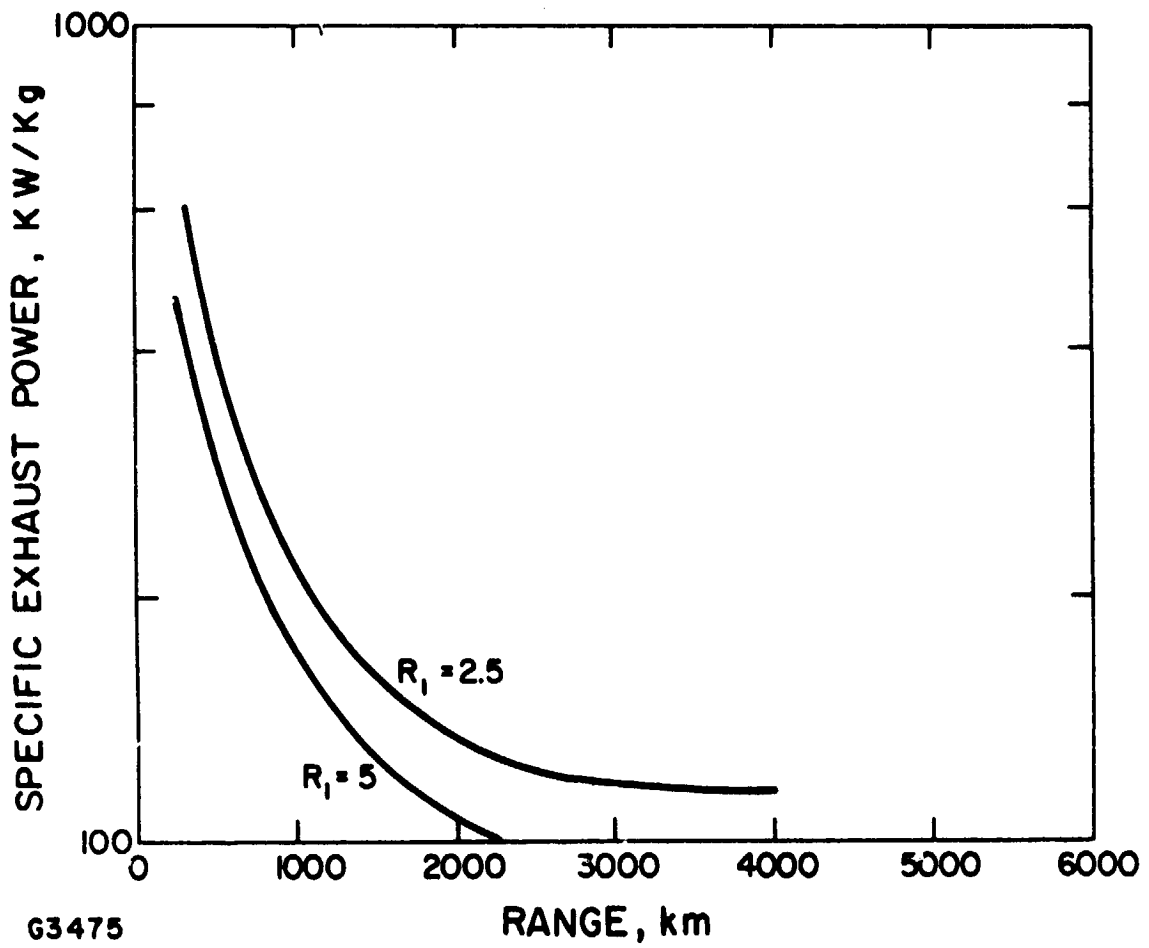
Fig. II-8   Exhaust Power vs Range for Rectilinear Launch to Orbital
             Velocity
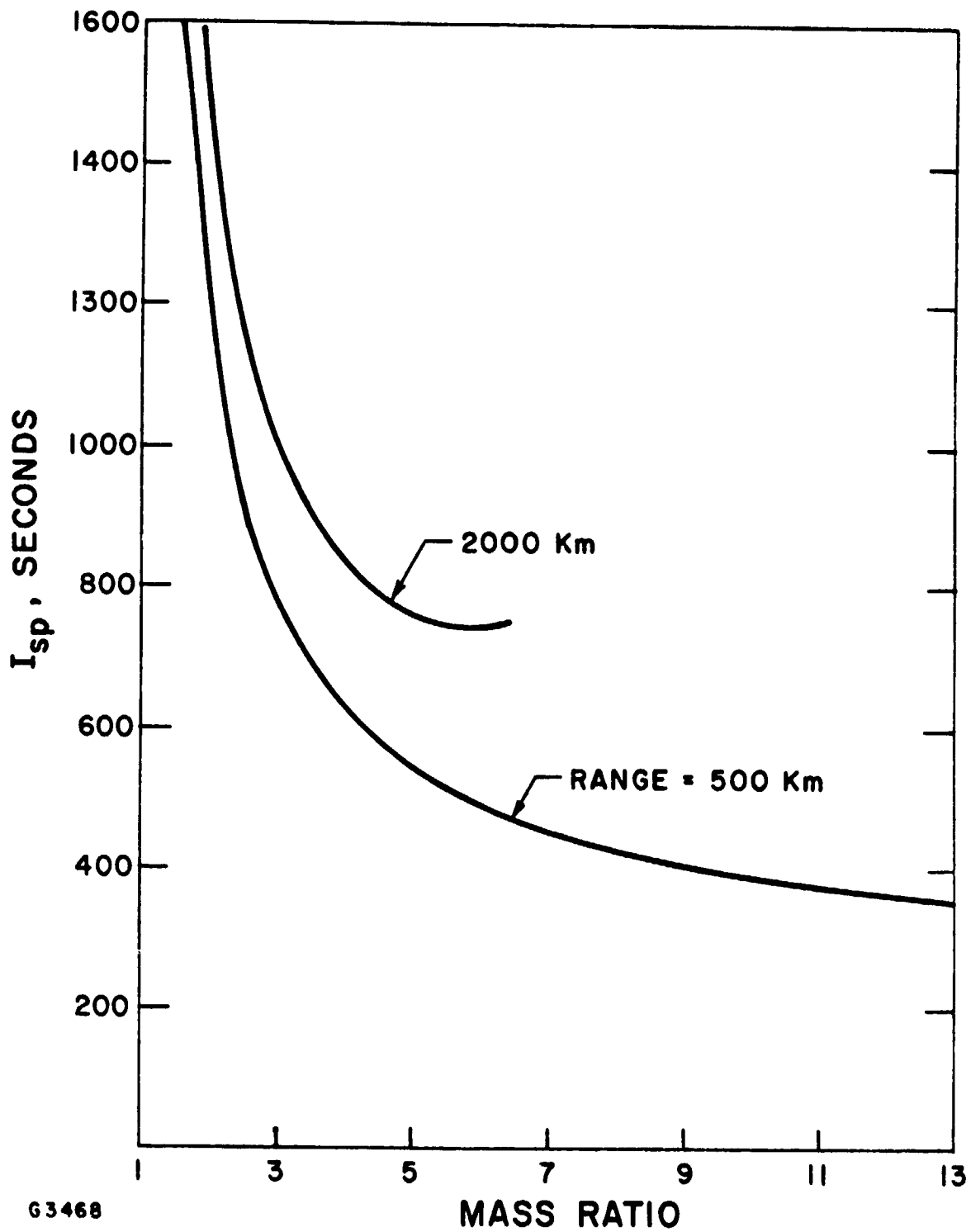
Fig. II-9   Specific Impulse vs Mass Ratio, Rectilinear Launch to Orbital
Velocity

and, differentiating

$$m\dot{c} = -\dot{m}c = ma \qquad \text{(II-35)}$$

so that the exhaust velocity increases linearly with time:

$$c = c_o + at \qquad \text{(II-36)}$$

During the first (vertical) phase of the ascent,

$$\ddot{y} = a - g_o = \frac{d}{dy}(1/2\,\dot{y}^2) \qquad \text{(II-37)}$$

so

$$1/2\,\dot{y}_1^{\,2} = (a - g_o)\,y_1 \qquad \text{(II-38)}$$

After y_1 is reached, the vertical motion of the vehicle is a coast against gravity, reaching zero vertical velocity after a further time

$$\tau = \frac{\dot{y}_1}{g_o} \qquad \text{(II-39)}$$

when the altitude is

$$y_2 = y_1 + 1/2\,\frac{\dot{y}_1^{\,2}}{g_o} = \hat{a}\,y_1 = \frac{\hat{a}}{2\,g_o(\hat{a}-1)}\,\dot{y}_1^{\,2} \qquad \text{(II-40)}$$

from Eq. (II-36), with

$$\hat{a} = a/g_o \qquad \text{(II-41)}$$

During this phase, the vehicle is thrusting horizontally, the equation of motion being simply

$$\ddot{x} = a \qquad \text{(II-42)}$$

and the horizontal velocity reached when the vertical velocity stops is

$$\dot{x} = a\tau = \frac{a\,\dot{y}_1}{g_o} = \hat{a}\,\dot{y}_1 \qquad \text{(II-43)}$$

If orbit insertion is to occur at this time, we must have

$$\dot{y}_1 = \frac{1}{\hat{a}}\,V_{co} \qquad \text{(II-44)}$$

and, from Eq. (II-34)

$$y_2 = \frac{V_{co}^2}{2\,\hat{a}(\hat{a} - 1)\,g_o} \tag{II-45}$$

The horizontal distance traversed before insertion is

$$x_2 = 1/2\,\frac{V_{co}^2}{a} = 1/2\,\frac{V_{co}^2}{\hat{a}\,g_o} = y_2 \tan\theta_2 \tag{II-46}$$

There is thus only one specific force which achieves insertion at a given zenith angle. If we assume $\theta_2 \approx 60^\circ$, because of laser propagation limitations, we will have

$$\hat{a} \approx 1 + \tan 60^\circ = 2.73 \text{ gees.} \tag{II-47}$$

The trajectory thus gives a gentle ride to orbit. From Eq. (II-46), the down range distance is then

$$x_2 \approx 1167 \text{ km} \tag{II-48}$$

and

$$y_2 = x_2 \cos\theta \approx 674 \text{ km} \tag{II-49}$$

The range at this time is then

$$\rho_2 = 1348 \text{ km.} \tag{II-50}$$

Since the range is given by

$$\rho_2 = \sqrt{x_2^2 + y_2^2} = \frac{V_{co}^2}{2\,g_o\,\hat{a}}\left[1 + \frac{1}{(\hat{a} - 1)^2}\right]^{1/2} \tag{II-51}$$

it is clear that the range is minimized by making $\hat{a}$ (and hence θ) as large as feasible.

The altitude at completion of the vertical ascent is, from Eq. (II-40)

$$y_1 = 247 \text{ km} \tag{II-52}$$

and the velocity then is, from Eq. (II-44)

$$\dot{y}_1 = 2.9 \text{ km/sec} \tag{II-53}$$

The total time taken for boost is

$$\tau_2 = \frac{\dot{y}_1}{a - g_o} + \frac{\dot{y}_1}{g_o} = \frac{V_{co}}{g_o}\left(\frac{1}{\hat{a}(\hat{a} - 1)} + \frac{1}{\hat{a}}\right)$$

$$= \frac{V_{co}}{g_o(\hat{a} - 1)} = \frac{V_{co}}{g_o \tan 60^o} = 465 \text{ seconds} \tag{II-54}$$

From Eq. (II-28), the overall mass ratio for boost is

$$R_2 = \frac{m_o}{m_2} = \frac{c_2}{c_o} = \frac{c_o + a\tau_2}{c_o} = 1 + \frac{V_{co}}{c_o}\frac{\hat{a}}{(\hat{a} - 1)} \tag{II-55}$$

So the initial exhaust velocity required is

$$c_o = \frac{V_{co}}{(R_2 - 1)}\frac{a}{(a - 1)} \tag{II-56}$$

and the final exhaust velocity is

$$c_2 = R_2 c_o = \frac{V_{co}R_2}{(R_2 - 1)}\frac{\hat{a}}{\hat{a} - 1} \tag{II-57}$$

The specific exhaust power is given directly by the equation of motion at burnout

$$\frac{P}{m_1} = 1/2\, a\, c_2 = 1/2\, g_o V_{co}\frac{\hat{a}^2}{\hat{a} - 1}\frac{R_2}{R_2 - 1} \tag{II-58}$$

This expression is plotted in Fig. II-10. Once again it appears that any mass ratio in excess of about 3 is acceptable. As an example, for a mass ratio of 5 the exhaust power requirement for launch to this fairly low orbit (altitude 675 km) is about 200 MW/metric ton. Boost is accomplished within 1350 km of the laser station: the power may thus be compared with that required for rectilinear boost vs minimum orbital velocity, which with this range limitation, is about 140 MW/metric ton, from Fig. II-8. It is clear that the trajectory presented here is by no means optimized.
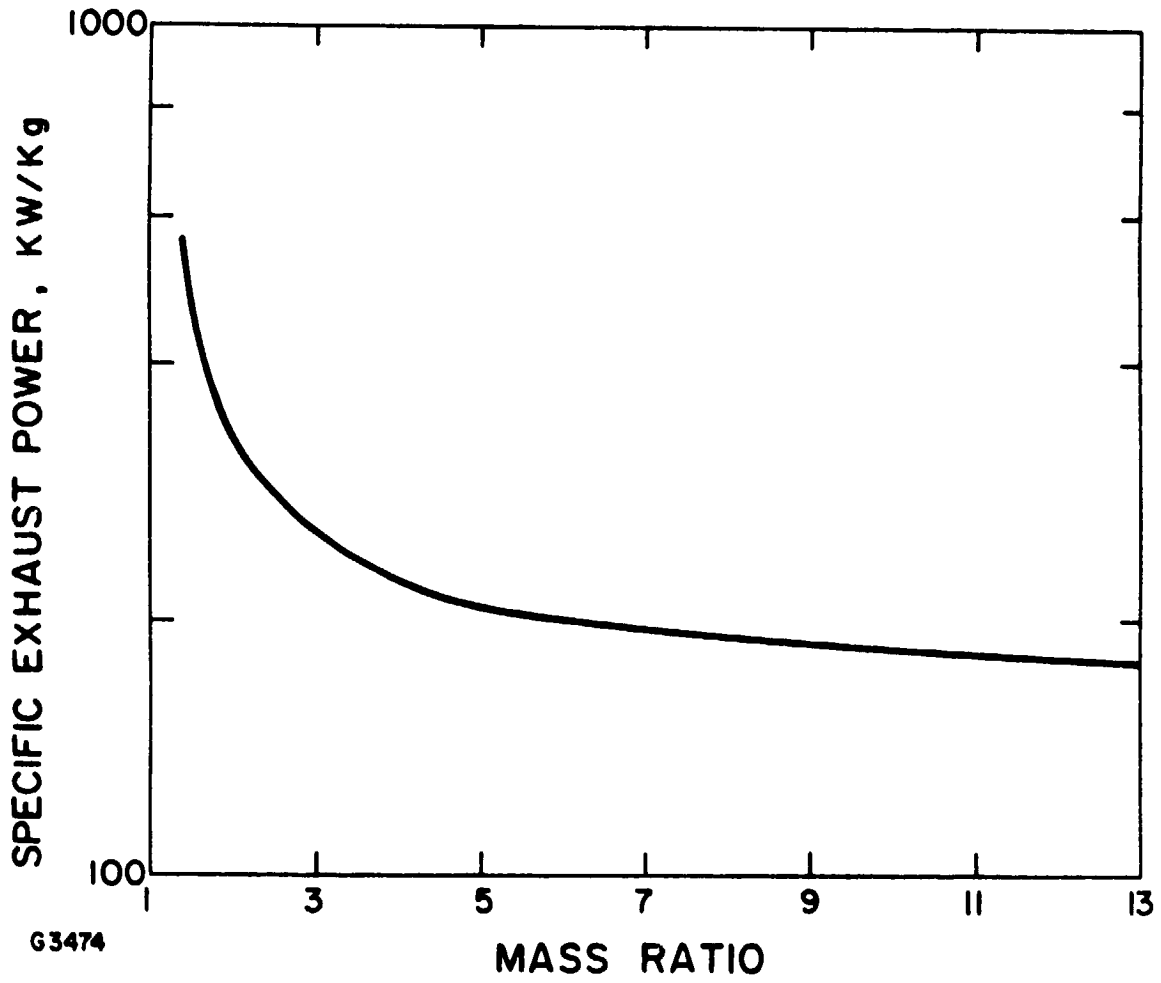
Fig. II-10   Exhaust Power Requirements, Launch to Orbit at Constant
             Specific Force

The initial and final specific impulses, obtained from Eqs. (II-47) and (II-48) are shown as functions of the mass ratio in Fig. II-11. The wide range of specific impulse and the relatively high values are principal disadvantages of launch at constant specific force.

Another disadvantage of this launch trajectory is that the angle between the thrust axis and the beam is not constant - in fact, it changes abruptly through 90° at the end of the vertical ascent phase. This fact, together with the high, variable specific impulse, could be expected to complicate greatly the design of the propulsion system if this ascent profile were seriously to be considered. The primary use of this analysis is thus as an existence proof that the basic dynamical constraints of laser propulsion systems do not preclude launch to stable, low orbit at reasonable ranges.

Ascent trajectory analysis for laser-powered launch systems is continuing under other programs. Of particular interest are trajectories which maintain a constant angle between the laser beam and the thrust axis, and in which the specific impulse of the engine is constant. It is expected that it will prove possible to launch to low orbit ($\approx$ 500 km) with specific exhaust powers of order 150 MW/metric ton and using a specific impulse of 800 seconds or less.
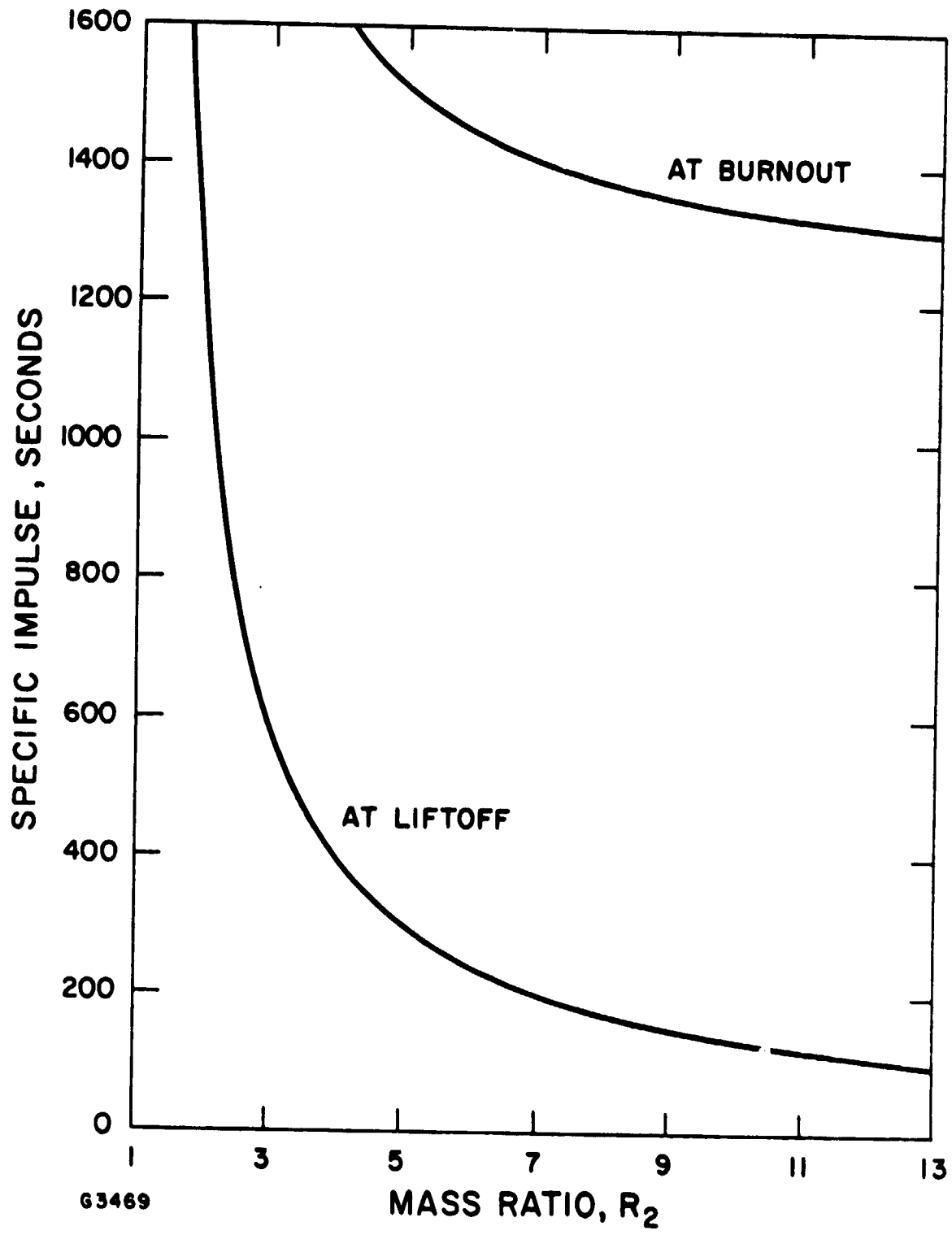
Fig. II-11   Specific Impulse vs Mass Ratio for Launch to Orbit at Constant Specific Force

III. ABSORPTION OF LASER RADIATION IN A WORKING FLUID

1. INTRODUCTION

According to the analyses presented in the previous sections, boost applications of laser propulsion may require specific impulses in the range 500 to 1200 seconds of thereabouts. Depending upon the molecular weight of the selected propellant, this may require thrust chamber temperatures up to $4000^{\circ}K$ or higher. In order to heat a working fluid to these temperatures by absorption of laser radiation the following absorption mechanisms have been proposed:

1. Use of a solid heat exchanger which is heated directly by radiation, the gas passing through it being heated by conduction. This technique is probably limited by the structural properties of solid heat exchangers to temperatures of order $2500^{\circ}K$.

2. Use of a dust or other aerosol suspended in the gas in the thrust chamber to make it opaque. While some refractory dusts, such as carbon or tungsten, may allow the achievement of high operating temperatures, it is difficult to maintain a reasonable compromise between operating temperatures and average molecular weight of the exhaust products with this technique.

3. Use of a molecular absorber. It is generally possible to find molecules exhibiting strong absorption bands at the wavelength of any particular laser. For a CO_2 laser (wavelength $10.6\ \mu$), a well known example of such a substance is sulfur hexafluoride (SF_6). Very short absorption lengths can be obtained with low concentrations of such molecular absorbers, at least at low temperatures. The principal problem with the use of these substances in laser propulsion systems is thermal dissociation of the molecule at the required operating temperature in the thrust chamber. While this effect may limit the temperatures which can be attained, it also offers the attractive possibility of finding a molecular absorber which provides the required opacity in the thrust chamber but which dissociates by the time that it passes through the throat. During the subsequent expansion and cooling the dissociation products may recombine with other constituents of the working fluid. In this way it may be possible to provide an exhaust which is transparent to the incoming laser radiation. This possibility certainly warrants further investigation, especially for use in single port engines (see below).

4. Use of inverse bremsstrahlung absorption. If sufficient free electrons can be provided in the thrust chamber, inverse

bremsstrahlung can produce absorption lengths of the order of several centimeters. In principle, the necessary concentration of electrons can be achieved by seeding the working fluid with a seedant of low ionization potential such as an alkali metal. While the stability of the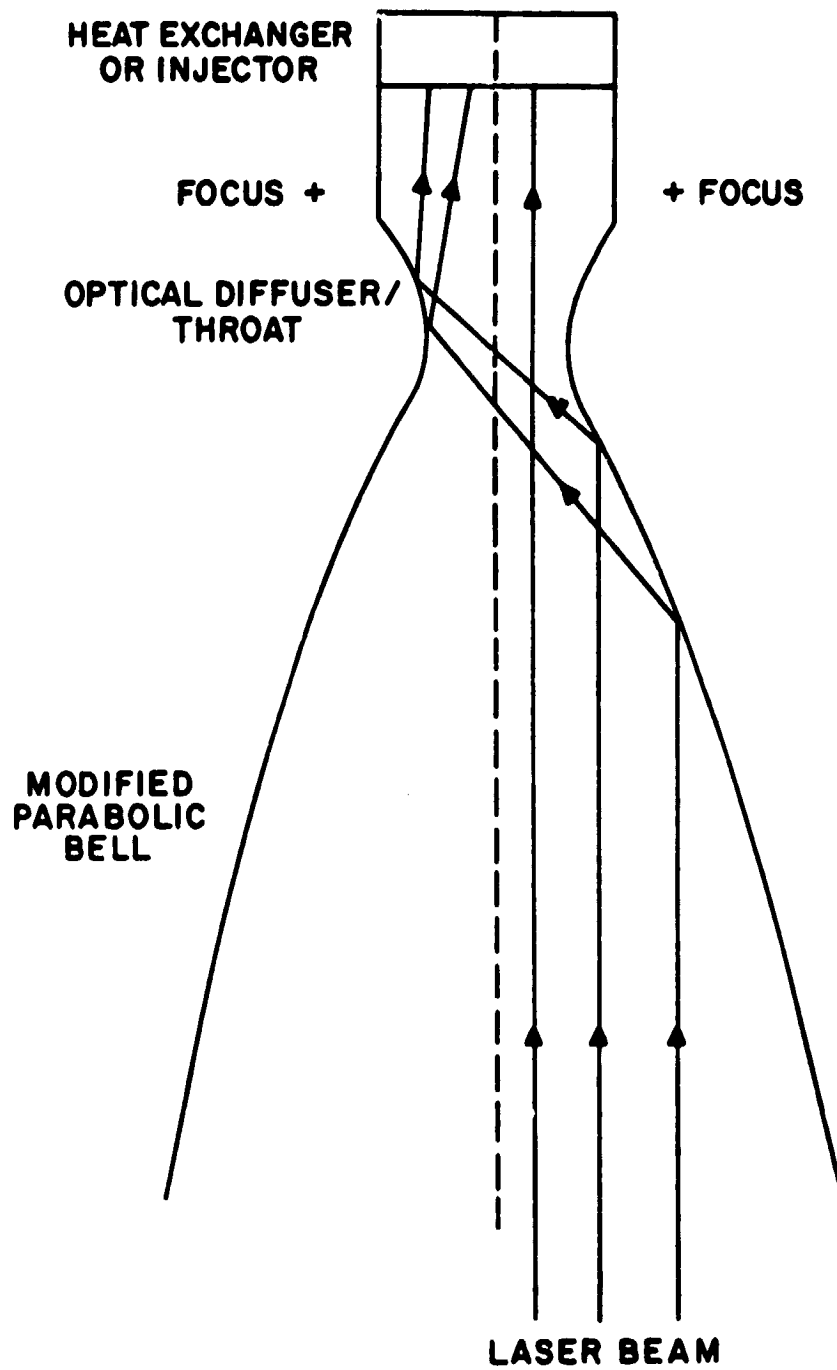 absorption region in such systems requires investigation, it may thus be possible to provide bulk heating of the seeded working fluid at the operating temperature in the thrust chamber. There is, however, another use of inverse bremsstrahlung absorption, which is to provide localized heating in a breakdown region. The temperatures reached in laser induced breakdown are typically very high (greater than $10,000^\circ K$) so that it would in general be necessary to provide turbulent mixing with new propellant downstream from the absorption region, in order to cool the gases to the desired operating temperature. An advantage of this technique is that it may be unnecessary to seed the propellant, as breakdown will occur in the focal region of a powerful laser in any medium if the flux density is sufficiently high.

The project reported here was a first investigation of the use of inverse bremsstrahlung steady state absorption for a laser-powered thruster.

Apart from the choice of absorption mechanism, a second major problem facing the designer of a laser powered rocket engine is that of admitting the laser radiation to the thrust chamber. Two solutions to this problem are conceptually possible. In the first the laser radiation enters the thrust chamber up the exhaust; such engines will be called single port engines. In the second type of engine (two port engine) a separate window is provided for admission of the laser radiation.

Figure III-1 is an outline of one possible single port engine configuration. The exhaust bell is a surface of revolution formed by rotating a parabola about a line which is parallel to but not coincident with the axis. As an optical reflector, this surface would produce a ring focus inside the throat, as shown. Use of a reflecting surface inside the throat can provide any desired flux density distribution in the thrust chamber itself. With this design it is possible to meet the optical requirements of the laser radiation collector as well as the gas dynamic requirements (expansion ratio, etc.) of the engine exhaust bell, in the same structure.

Engines of this type are clearly adapted to missions in which it is possible for the thrust axis to remain almost collinear with the laser beam (for example the rectilinear launch to escape discussed in Section II-2). It may be possible to use any of the absorption mechanisms listed above with single port engines, although the feasibility of aerosol absorption might depend upon finding a dust which evaporated at the desired operating temperature so as to render the exhaust transparent. As noted above molecular absorption may be particularly well suited to single port engines. Inverse bremsstrahlung absorption may be used if the kinetics of recombination,

HEAT EXCHANGER
OR INJECTOR

FOCUS +   + FOCUS

OPTICAL DIFFUSER/
THROAT

MODIFIED
PARABOLIC
BELL

LASER BEAM

G3568

Fig. III-1   Single-Port Engine

-33-

as the gas temperature drops in the exhaust, are sufficiently rapid to reduce substantially the electron population in the throat, or shortly thereafter. Of the various absorption mechanisms, inverse bremsstrahlung absorption probably offers the highest operating temperature capability and hence highest specific impulse in single port engines.

Two-port engines offer greater flexibility in the missions for which they can be used because the laser radiation collector is separate from the engine bell and hence can be designed so that large angles between the thrust axis and the laser beam may be accommodated. In such engines it is necessary to provide a separate window to the thrust chamber which is transparent to the incoming laser radiation and which can withstand the temperatures and pressures within the thrust chamber to which it is exposed. Recent progress at AERL, Inc.[8] has indicated that aerodynamic windows can be designed to withstand thrust chamber pressures of up to at least 20 atmospheres, and it is probable that such windows would be used in an operational engine. The experiments reported here were however based on the use of a solid window, constructed from a small polished diamond chip.

Type IIA diamond is an excellent material for the construction of windows to transmit high power 10.6 μ laser radiation. The advantages of diamond include the following factors:[9] (1) for natural or artificial stones having a low nitrogen content, the absorption length at the wavelength of interest may be of the order of meters; (2) the thermal conductivity is very high (exceeding that of copper by a factor of 4 at room temperature and a factor of 20 at liquid nitrogen temperature), so that edge cooling of the window is feasible; (3) the material is, of course, very strong, so that large pressure differentials may be supported by thin windows; and (4) the flux density which may be transmitted appears to be in excess of 10^7 watts per square centimeter, and may in fact be limited not by the diamond itself, but by breakdown at the surface due to contaminants or in the gas near the window. This last factor means that small and relatively cheap windows may be used to transmit quite large powers, by operation near a focus. The high refractive index of diamond causes a relatively large surface reflectivity (17% at 10.6 μ for normal incidence), but this can be corrected, if necessary, by operating the window at the Brewster angle with respect to the laser beam (which of course requires that the beam be plane polarized) or by grinding the window to form a half-wave etalon (so that it becomes in effect its own anti-reflection coating).

At the time this project was initiated the simplicity of a solid window appeared to justify use of a diamond chip for this purpose. While it was of course recognized that, because of their cost, diamond windows would not provide an acceptable solution for engines of a larger size, in the range of operational interest, they would allow early experiments to be undertaken at small scale and at low power levels. As noted above progress since that time in both aerodynamic windows and single port engines has been such that one of these techniques would probably now be given priority over the use of a diamond window.
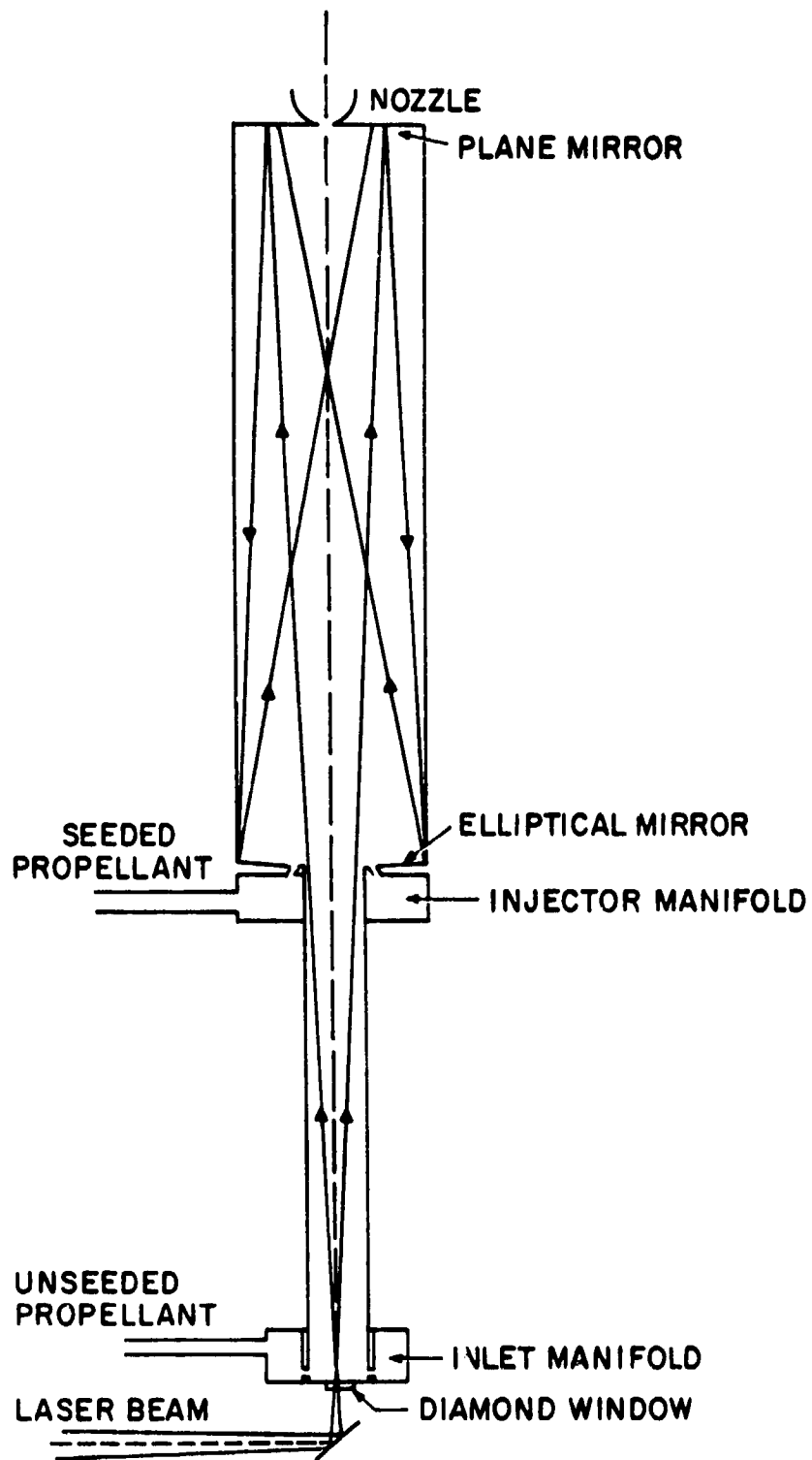
2. TEST CELL LAYOUT AND OPTICAL DESIGN

As a first application of the diamond window to laser propulsion a design study was undertaken for an engine to operate at a power level of 10-15 kW using the AERL HPL-10 CW CO_2 welding laser. For numerical estimates, a specific impulse design goal in excess of 800 seconds was adopted. The engine was to be operated at a temperature and seed concentration such that the absorption length due to inverse Bremsstrahlung in the thrust chamber was of the order of the chamber dimensions, so as to provide bulk heating of the working fluid. However, a self starting capability could be provided by bringing the beam to a focus inside the chamber; note that this could also be achieved by using an electrical spark. To start up the engine, seeded propellant flows through the chamber so that when the laser is switched on breakdown occurs at the focus. As the gas heats the absorption region expands to fill the chamber. If the absorption length in the chamber is sufficiently small the radiation reaching the focus will be so attenuated as to suppress breakdown there, once the engine is in its steady state operating condition.

At a power level of 15 kW, the clear aperture required in the diamond window is less than 1 millimeter. Such windows are readily obtainable and relatively cheap (up to several hundred dollars at the beginning of this project, depending on the optical finish desired; now of order $1500). However, the window must be isolated from the high operating temperature in the thrust chamber.

The first conceptual mechanization which was proposed is shown in Fig. III-2. To minimize convective heat transfer to the window it is mounted in a heat sink at the end of the window isolation tube. Unseeded propellant is blown over the inside of the window, to keep the surface clean and aid in cooling it, and then passes up the isolation tube to the thrust chamber. This gas flow serves the secondary purpose of minimizing the diffusion of seeded propellant into the isolation tube, which could cause breakdown there. Conductive heat transfer to the window can be prevented, if necessary, by cooling the isolation tube. To minimize radiative heating of the window and window assembly it is important that laser radiation entering the thrust chamber be trapped there, and not allowed to escape back down the isolation tube after one or two reflections. For this purpose advantage may be taken of the annular beam intensity distribution which is characteristic of lasers using unstable resonators.

In this design the laser beam is converging as it enters the window, coming to a first focus just inside. The beam, now diverging, passes up the isolation tube and into the chamber where it is reflected from a plane mirror forming the aft end. Because the beam is annular little radiation enters the nozzle. The forward end of the chamber is an annular mirror (ideally elliptical but a spherical mirror would be adequate in this small engine) and the geometry is so chosen that the hole in the beam is larger than the exit of the isolation tube. The curved mirror brings the radiation to a second focus, on the chamber axis about 2/3 the chamber length away

NOZZLE

PLANE MIRROR

SEEDED
PROPELLANT

ELLIPTICAL MIRROR

INJECTOR MANIFOLD

UNSEEDED
PROPELLANT

INLET MANIFOLD

LASER BEAM

DIAMOND WINDOW

D8963

Fig. III-2   Two-Port Thrust Chamber with Two Internal Mirrors

-36-

from the forward end. The optical path length inside the chamber is thus about 2.7 times the chamber length before coming to a focus.

Seeded propellant is injected around the exit of the isolation tube so as to insure good mixing. In steady state operation, the absorption length in the chamber is expected to be about 0.6 times the chamber length so that the beam will be attenuated by a factor of 5 before reaching the aft end of the chamber and by a factor of 100 before reaching the chamber focus.

One of the disadvantages of this design is that it contains mirrors which are directly exposed to the hot gases inside the thrust chamber. However, the mirrors are required primarily only during startup, since 80% of the beam power is absorbed in the first pass through the chamber, during steady state operation. While it was not expected that the propellants to be employed will seriously contaminate the mirrors, it is possible that the mirrors would require cleaning between runs.

Because of the use of hydrogen as a propellant, and of alkaline metals as seedants, it was necessary in practice to mount the test chamber in a sealed tank, as described in Section IV. Opening this tank and purging it of seedant was a time-consuming process, necessitating the removal of the apparatus from the HPL-10 CO_2 welding laser facility. In order to allow inspection of the test chamber mirrors, and replacement if necessary, without disassembly a simplified design was proposed which is shown in Fig. III-3. It differs from the previous design only in that the laser beam is brought to a focus for start-up after a single reflection within the chamber. As discussed in the next section the shorter optical path length within the chamber was expected to reduce the probability of stable operation in a bulk absorption mode. However, the operational problems with the 2-mirror design were considered to be of more significance.

For completeness an alternative design is shown in Fig. III-4, in which the mirrors needed to bring the beam to a focus are outside the thrust chamber and are exposed only to cool, unseeded propellant. This design was more complicated to build and would have introduced difficulties in the inspection and cleaning of mirrors. It was, therefore, rejected for the present program in favor of the single internal mirror design.

3. STABILITY OF THE ABSORPTION REGION

a. Engine with Two Internal Mirrors (Fig. III-2)

Consider the optical diagram of Fig. III-5, in which extraneous components of the engine have been deleted and the transverse dimension has been exaggerated for clarity. A basic requirement for stability of the absorption region near the chamber focus is that, as it expands up the laser beam, it should encounter a decreasing flux density. While this condition may not be sufficient to ensure stability, its violation will result in the breakdown region running along the beam, perhaps until it reaches the window focus, resulting in destruction of the diamond window.

UNSEEDED
PROPELLANT

SEEDED
PROPELLANT

LASER BEAM

NOZZLE

DIAMOND
WINDOW

INLET
MANIFOLD

INJECTOR
MANIFOLD

FOCUSSING
MIRROR
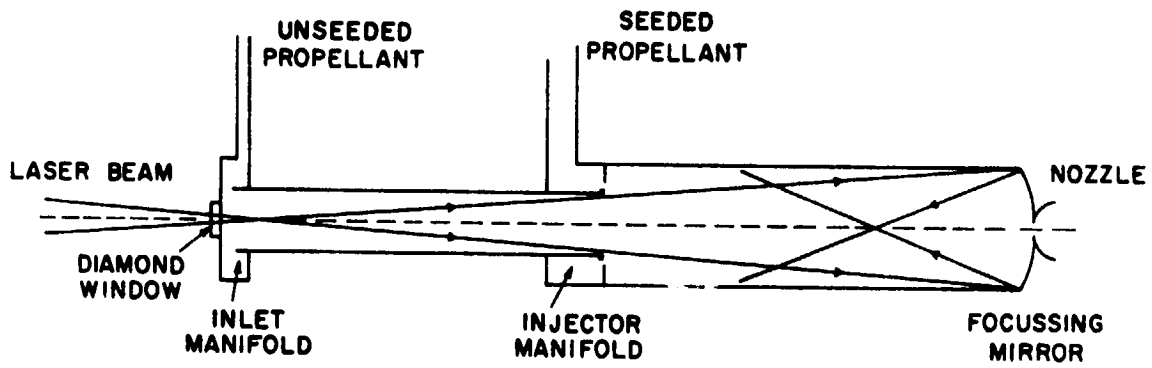
G3569

Fig. III-3   Two-Port Thrust Chamber with Single Internal Mirror
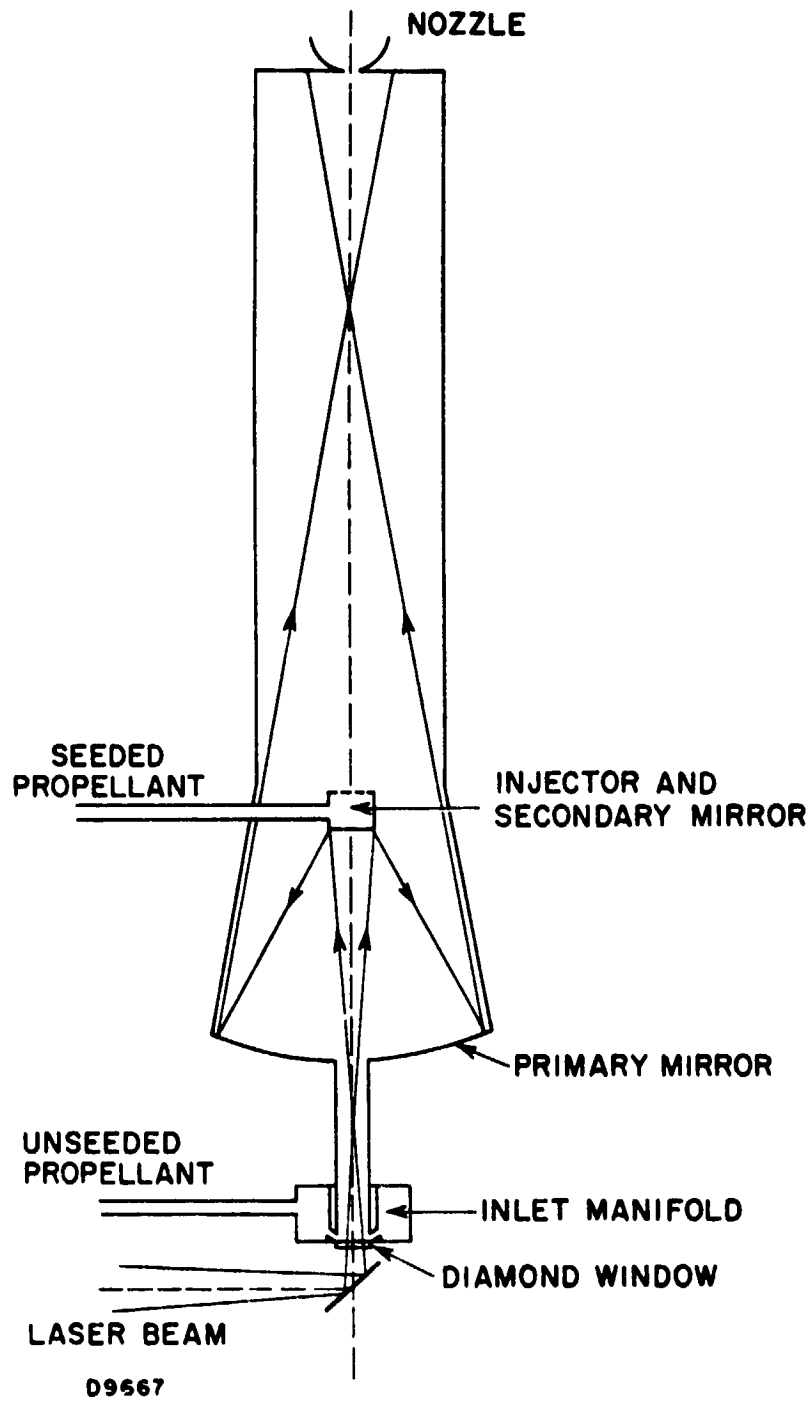
Fig. III-4   Two-Port Thrust Chamber with External Mirrors

D9667
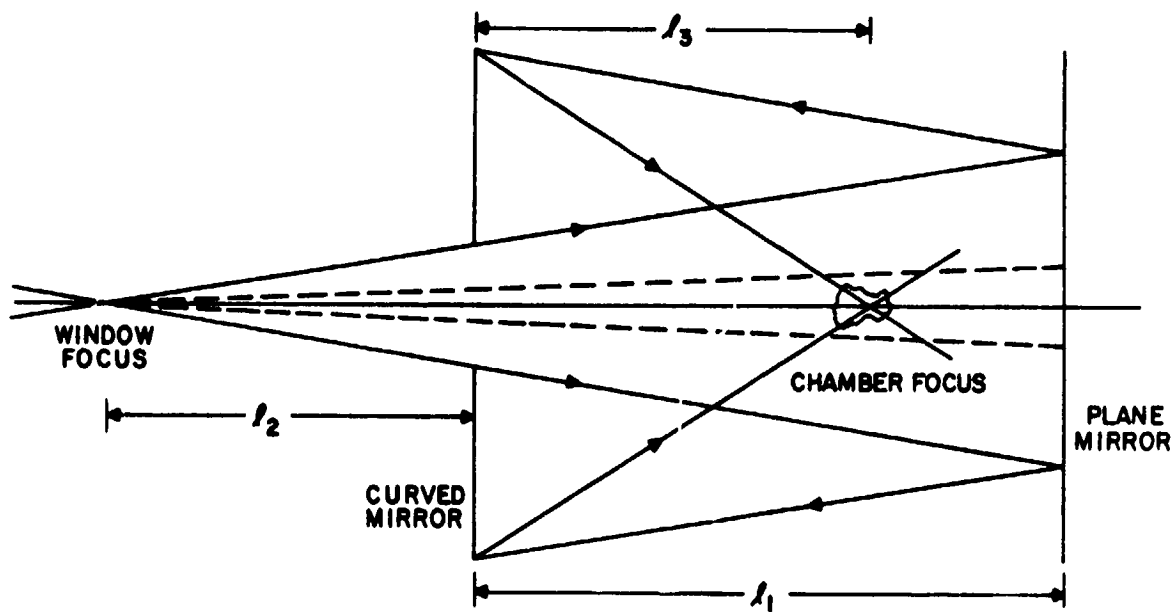
G3570

Fig. III-5   Optical Schematic of Two-Mirror Engine

The central region of the laser beam, where the flux density is low, is shown dotted in the figure for the first pass of the beam through the thrust chamber. As long as the absorption region is small, as shown, virtually all the flux reaching it is from the third-pass beam, reflected from the curved mirror. The situation is thus quite similar to a breakdown at a simple focus of a one-pass beam, and the above stability condition is clearly met.

In order to approximate conditions as the absorption region expands, we may calculate first the mean flux density distribution within the chamber in the absence of breakdown. At a station x within the chamber (measured aft from the curved mirror, in units in which the chamber length is one), the cross-sectional area of the first-pass beam is, from the geometry of Fig. III-5,

$$ A = \pi y_c^2 \frac{(\ell_2 + x)^2}{(\ell_2 + 2)^2} \tag{III-1} $$

where y_c is the radius of the thrust chamber and ℓ_2 is the length of the window isolation tube (as a fraction of the chamber length).

The cross-sectional area of the second-pass beam at this point is:

$$ A_2 = \pi y_c^2 \frac{(\ell_2 + 2 - x)^2}{(\ell_2 + 2)^2} \tag{III-2} $$

and the area of the third-pass beam, converging to a focus at $x = x_F$, is:

$$ A_3 = \pi y_c^2 \left(1 - \frac{x}{x_F}\right)^2 \left(1 - \frac{x}{x_F}\right)^2 \tag{III-3} $$

Neglecting losses at reflection, and ignoring the direction of propagation, the total average flux density at x, from all three beams, is

$$ I = P_o \left(\frac{1}{A_1} + \frac{1}{A_2} + \frac{1}{A_3}\right) = \Gamma I_c \tag{III-4} $$

where P_o is the laser power leaving the window focus,

$$ I_c = \frac{P_o}{\pi y_c^2} \tag{III-5} $$

is the average flux on the curved mirror, and

$$\Gamma = (\ell_2 + 2)^2 \left(\frac{1}{(\ell_2 + x)^2} + \frac{1}{(\ell_2 + 2 - x)^2} \right) + \frac{1}{(1 - \frac{x}{x_F})^2} \quad \text{(III-6)}$$

is the flux concentration factor.

If the intensity distribution were uniform across the beam, the flux density given by Eq. (III-4) would be the value on axis. More realistically, it is the average flux density, in the absence of breakdown, in that region of the thrust chamber which is traversed by all three beams.

The flux concentration factor Γ is plotted as a function of x in Fig. III-6, for $x_F = 2/3$ and for several values of the window isolation tube length. As one would expect, in the region near the chamber focus the flux density is dominated by the converging third-pass beam, and conditions there are similar to a simple one-pass focus. At first sight, it appears from the figure that an instability is present if the window isolation tube is too short (less than about 1.5 times the chamber length) and if the absorption zone expands too far towards $x = 0$. In order to evaluate this possibility, it is however necessary to consider extinction of the second and third-pass beams by the absorption zone, and also the nature of the absorption process.

Breakdown is initiated at high flux densities near the focus and the breakdown front propagates initially back up the third-pass beam by means of a detonation wave. However, the flux density required to maintain a detonation wave is of order 10^7 watts/cm^2[10]. Even if the laser power level within the chamber were as high as 15 kW, this implies that the detonation wave will not propagate past the point where the diameter of the third-pass beam is of order 0.5 mm. Beyond this point, the absorption front proceeds by means of a deflagration wave, which, in favorable circumstances (low gas flow and readily ionizable medium, conditions which exist in the test cell) may be sustained down to flux densities of order 10^4 watts/cm^2[10] which, for the HPL-10 welding laser, implies beam diameters of order 1 cm, comparable to the dimensions of the test cell.

If the absorption region is expanding so as to fill the converging third-pass beam and is essentially opaque, it blocks an increasingly large central portion of the second and third-pass beams: its effect is thus to enlarge the central, low-flux region in the third-pass beam without reducing the flux density in the periphery. However, it is clear from Fig. III-5 that the second and third-pass beams are completely extinguished when the front reaches the point where the first- and third-pass beams have the same diameter. From Eqs. (III-1) and (III-3), this occurs when

$$1 - \frac{x}{x_F} = \frac{\ell_2 + x_F}{\ell_2 + 2}$$
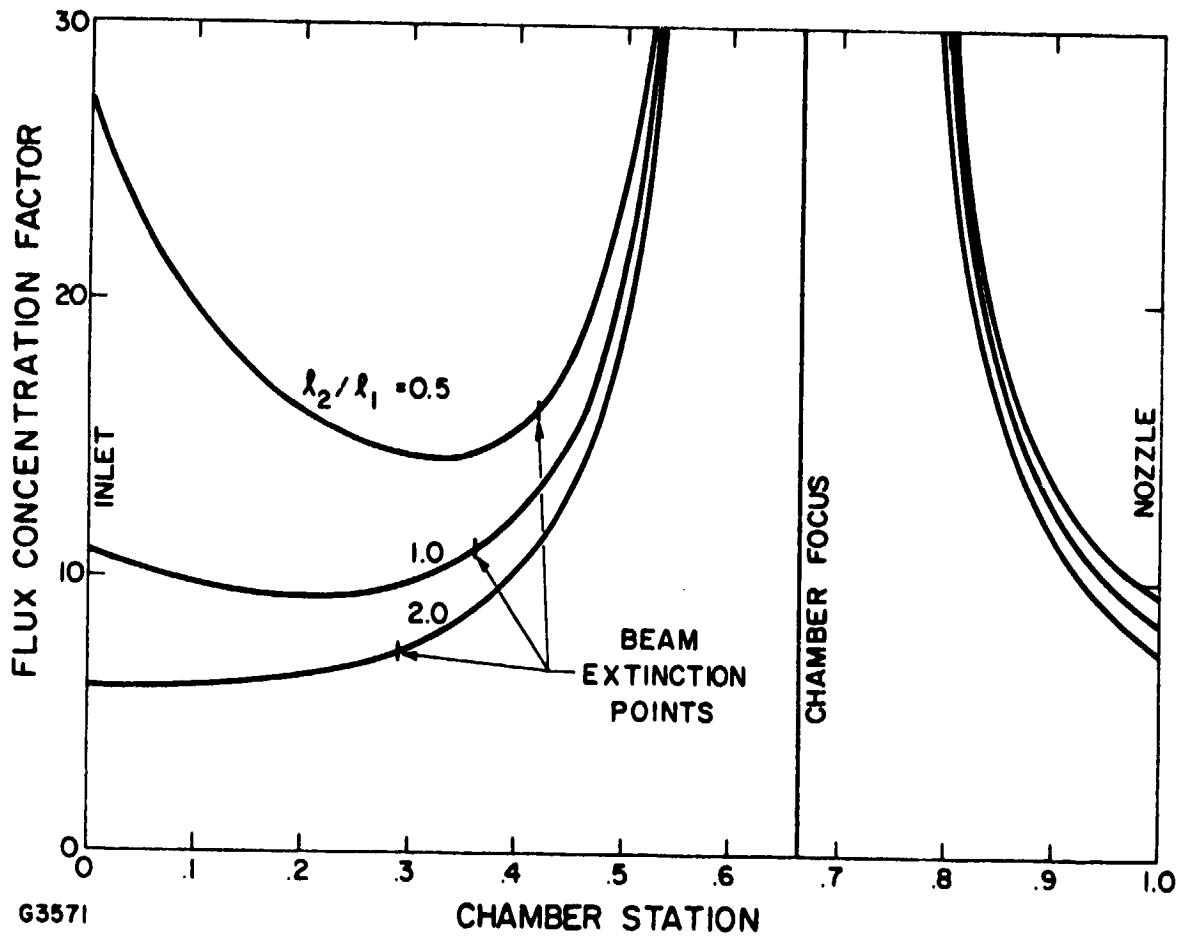
Fig. III-6   Chamber Flux Concentration, Two-Mirror Engine

or

$$x = \frac{2x_F}{2 + x_F + \ell_2} \tag{III-7}$$

For typical values of ℓ_2, this will lie in the range of $0.3 < x < 0.4$. The points are shown as "Beam Extinction Points" in Fig. III-6, and it is seen that, in all cases, they lie closer to the focus than the minimum in the flux concentration curves in the absence of breakdown.

If the deflagration front reaches the beam extinction point, it is now definitely in a region where the flux density, being due now only to the diverging first-pass beam, increases with decreasing x. The instability is therefore expected to exist, regardless of the length of the window isolation tube (although this affects the flux density gradient and hence the strength of the instability).

If the breakdown region is not localized in the high-flux region near the chamber focus, prevention of propagation of the absorption front up to the window focus thus relies on the seedant concentration gradient encountered as the front approaches the exit of the window isolation tube, around which the seedant is injected. The flux densities in the distal portion of the window isolation tube are expected to be too low to support a deflagration wave in clear unseeded gas (hydrogen or helium) and it is this condition on which preservation of the diamond window ultimately depends. The problem of instability in engines of this type would clearly have to be considered again if operation at higher power levels were considered, where the detonation wave region around the chamber focus was larger.

b. <u>Engine with One Internal Mirror (Fig. III-3)</u>

Figure III-7 is a schematic of this simplified engine, with the transverse dimension again exaggerated for clarity. Once again, the stability is like that of a simple one-pass laser focus if the absorption region is within the low-flux central region of the first-pass beam.

The area of the first-pass beam at station x is now given by

$$A_1 = \pi y_c^2 \frac{(\ell_2 + x)^2}{(\ell_2 + 1)^2} \tag{III-8}$$

and that of the second-pass, focussing beam is

$$A_2 = \pi y_c^2 \frac{(x - x_F)^2}{(1 - x_F)^2} \tag{III-9}$$

-44-
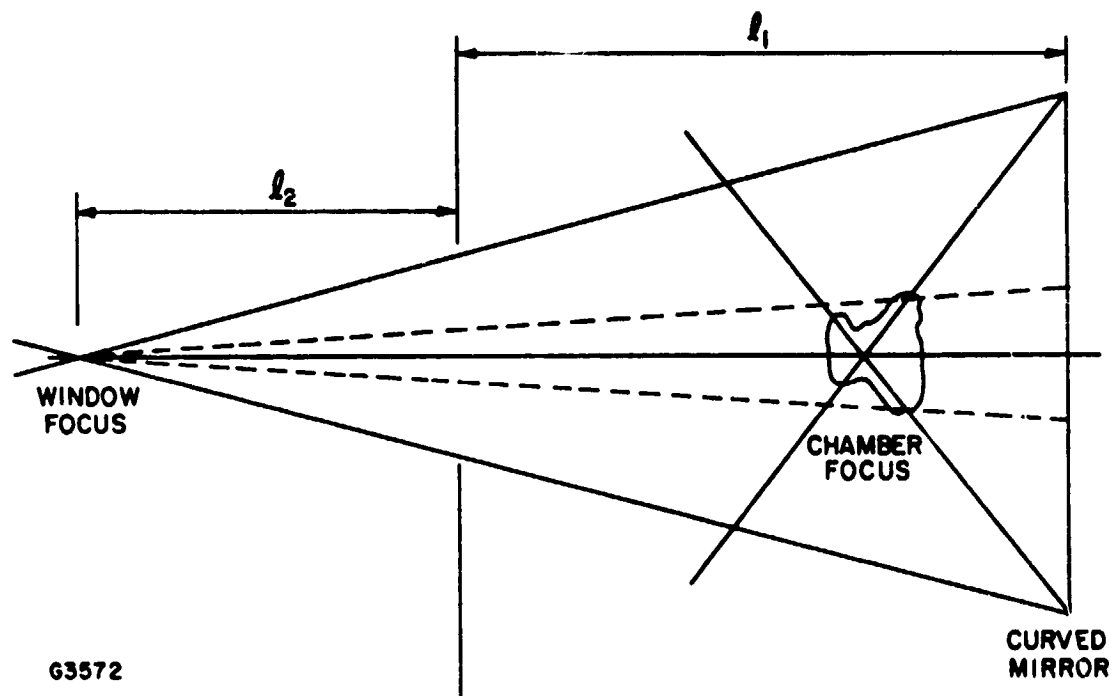
Fig. III-7   Optical Schematic of Single-Mirror Engine

The flux concentration factor is thus

$$\Gamma = \frac{(\ell_2 + 1)^2}{(\ell_2 + x)^2} + \left(\frac{1 - x_F}{x - x_F}\right) \qquad \text{(III-10)}$$

and is plotted in Fig. III-8, for several values of the window isolation tube to chamber length ratio. The flux density is more strongly concentrated near the focus and lower elsewhere in the chamber than in the two-mirror engine, because of the shorter focal length of the mirror. This should give more reliable initiation of breakdown. The initial detonation wave will propagate up the second pass beam, towards the nozzle, and the other side of the absorption zone, if it is nearly opaque, will be exposed only to the first pass beam. It is dubious whether the flux density at this point, in the experiments to be described here, will ever be sufficient to support a deflagration wave; but if it is, the absorption zone can be expected to propagate back up the diverging first-pass beam. Protection of the diamond window will then depend on extinction of the deflagration wave by the seedant concentration gradient near the exit of the window isolation tube, as in the two-mirror engine.

There appears to be a somewhat higher probability of a localized, high-temperature absorption zone (rather than bulk absorption) in the single-mirror test chamber. However, it is not clear that this is an undesirable operating condition. As noted above, the possibility that the mirrors might require cleaning between runs was a major factor in the decision to build for test purposes a single-mirror design, in which cleaning was operationally far simpler.

c. External-Mirror Engine (Fig. III-3)

Since this mirror is a single-pass system, it is expected that laser-induced breakdown will result in a hot spark at the focus, as in other simple laser breakdown experiments. The stability problems discussed above do not arise but bulk absorption is quite improbable.

4. CHOICE OF PROPELLANT, SEEDANT AND OPERATING CONDITIONS

In order to minimize the operating temperature required for a given specific impulse, the obvious choice of working fluid in these engines is hydrogen or helium. Because of its lower cost and simpler cryogenic tankage, hydrogen is clearly preferable for an operational engine, but, as discussed below, it is possible that helium would be advantageous in the first test engine.

The thermal losses are discussed in Sections III.5.c and III.6 where it is shown that, at low power levels, it is essential that the physical size of the engine be minimized, so that reasonable operating efficiency may be achieved. For the present engine, taking into account constructional
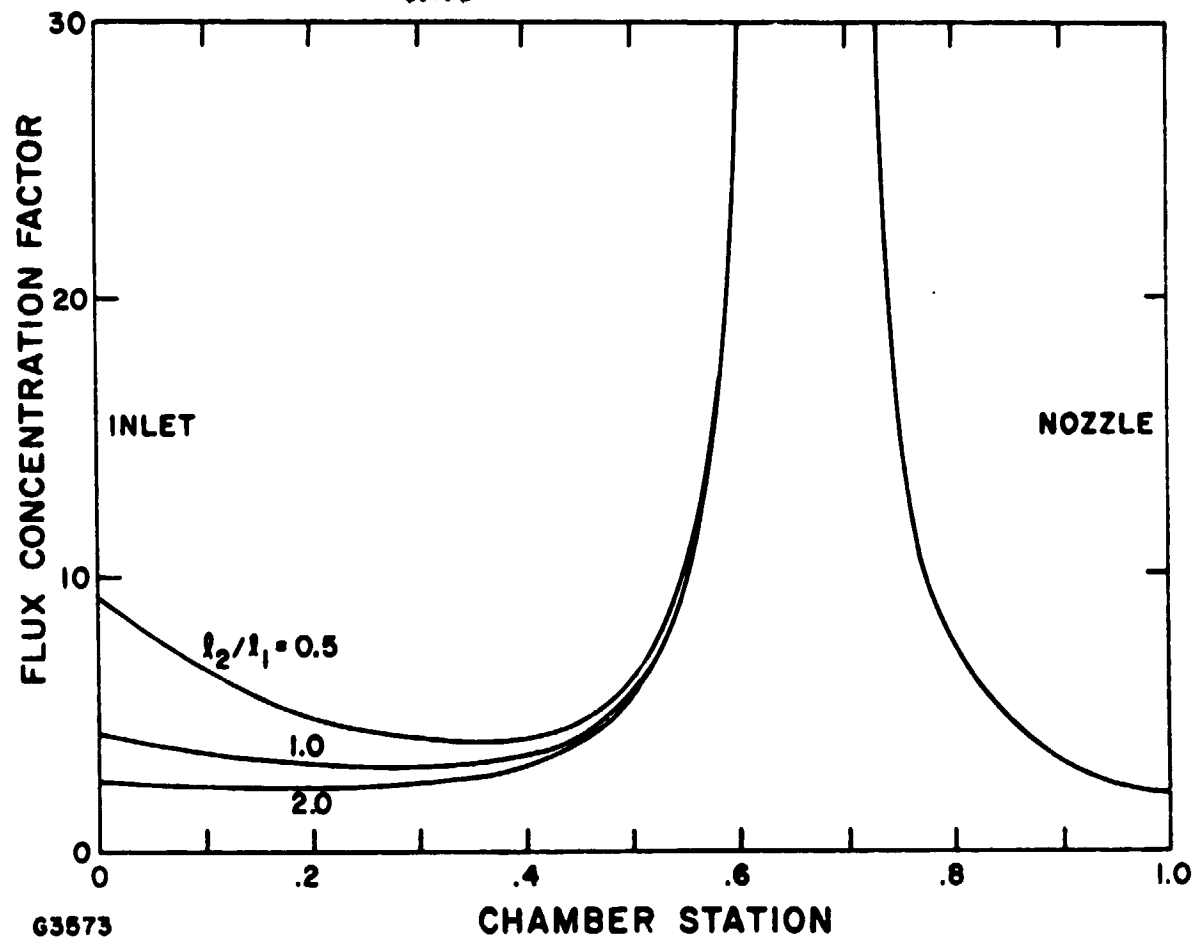
Fig. III-8   Chamber Flux Concentration, Single-Mirror Engine

difficulties, this means that a seedant must be chosen which gives an absorption length of the order of centimeters.

Cesium is commonly used as a seedant when free electrons are desired in a gas mixture, because its ionization potential (3.9 ev) is the lowest of any element. However, the situation is somewhat complicated in the present case because the operating temperature needed in a rocket engine to give a specified exhaust velocity depends on the average molecular weight of the propellants and hence on the atomic weight as well as the concentration of seedant. Cesium has a relatively high atomic weight (133) and it is possible that other seedants, with higher ionization potentials but lower atomic weights, might allow the desired performance to be achieved at a lower chamber temperature. The following discussion of the physics involved in the steady state absorption of laser radiation by inverse bremsstrahlung and flowing gases is adapted from that given in Ref. 11.

5. CESIUM-SEEDED HYDROGEN ENGINE: PARTIAL PRESSURE AND IONIZATION OF CESIUM

The absorption mechanism to be employed is inverse Bremsstrahlung. Taking into account only absorption by electrons in the field of ions, the absorption length y is given by[12]

$$y^{-1} = 8.799 \times 10^{11} \, p_s^2 \, \beta^2 \, T^{-5} \, (1 - e^{-T_b/T}) \tag{III-11}$$

where β is the fraction of cesium atoms which are ionized, p_s is the partial pressure of cesium (in atmospheres) in the absence of ionization, and

$$T_b = h\nu/k = 1359°K \tag{III-12}$$

where ν is the laser frequency, h is Planck's constant, and k is Boltzmann's constant. The term in T_b takes account of losses by stimulated emission.

In equilibrium, the ionization is controlled by the Saha equation[13]

$$\frac{\beta^2}{1-\beta} = 3.287 \times 10^{-7} \, \frac{T}{p_s}^{5/2} \, e^{-T_i/T} \tag{III-13}$$

where $T_i = 45\ 178°K$ is the ionization temperature of cesium, corresponding to an ionization potential of 3.89 eV.

If p_s from this equation is substituted in Eq. (III-11), one obtains

$$\left(\frac{1}{\beta} - 1\right)^2 = 10.52 \, \gamma^{-1} \, T^{-5/2} \, e^{2T_i/T} / \left(1 - e^{-T_b/T}\right) \qquad \text{(III-14)}$$

which, for a given y, allows the required ionization to be calculated as a function of temperature. The corresponding p_s may then be obtained from (Eq. (III-13). The results are plotted in Fig. III-9, for y = 2 cm, 4 cm and 8 cm. Since electron-neutral inverse Bremsstrahlung has been neglected, these curves may slightly over-estimate the required cesium concentration at the lower end of the temperature range.

a. Dissociation of Hydrogen

A complication arises if the propellant is hydrogen, because the range of chamber temperatures of interest is that in which hydrogen is partially dissociated. Assuming a matched expansion in the nozzle, the thrust produced by the engine is

$$F = 2P/c = C_F p_c A_t \qquad \text{(III-15)}$$

where P is the power in the exhaust, c is the exhaust velocity, p_c is the chamber pressure, A_t is the nozzle throat area, and C_F is the thrust coefficient. The diameter of the nozzle throat is then

$$d_t = \left[\frac{8P}{\pi C_F p_c c}\right]^{1/2} \qquad \text{(III-16)}$$

and the time taken for a particular small sample of gas to pass through the nozzle may be roughly estimated as

$$\tau \simeq d_t/c \simeq \left[\frac{8P}{\pi C_F p_c c^3}\right]^{1/2} \qquad \text{(III-17)}$$

As an example, assume

$$P \simeq 10 \text{ kW}$$

$$c \simeq 8 \text{ kM/sec}$$

$$p_c \simeq 30 \text{ atm}$$

$$C_F \simeq 1.7$$
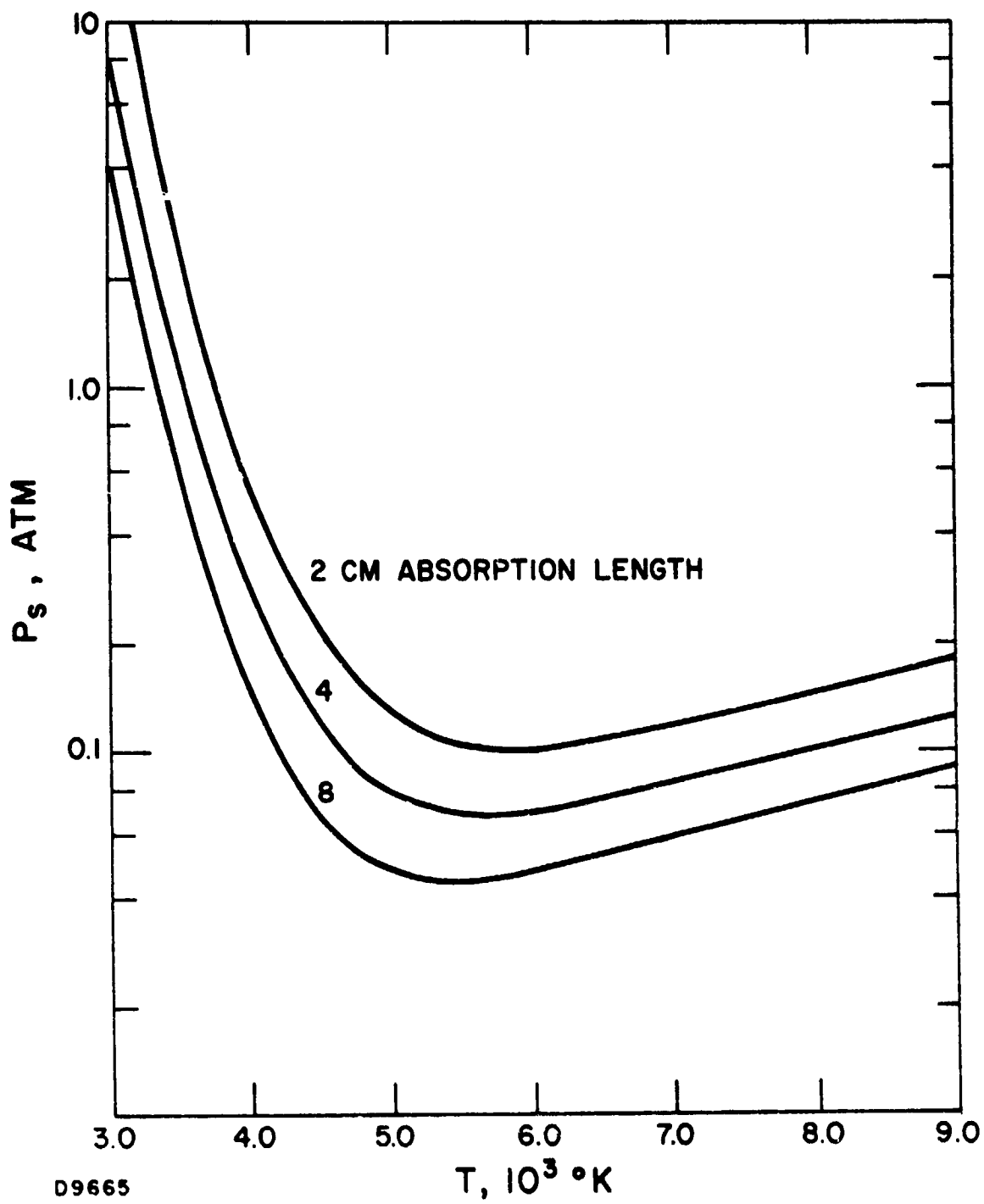
Fig. III-9   Opacity Map for Cesium

which gives

$$F \simeq 2.5 \ 10^5 \text{ dynes} \simeq 0.5 \text{ lb}$$

$$d_t \simeq 0.8 \text{ mm}$$

$$\tau \simeq 0.1 \ \mu s \tag{III-18}$$

The nozzle is thus so small and the time scale for the expansion of gas in the exhaust so short that little recombination of the dissociated hydrogen can be expected. The enthalpy added to the gas in the form of dissociation energy is thus largely wasted.

In equilibrium, the fraction $\beta*$ of hydrogen atoms which are dissociated is given by[13]

$$\frac{\beta*^2}{1-\beta*} = 4.477 \ \frac{T}{P_1}^{3/2} \ e^{-T_d/T} \ 1-e^{-T_v/T} \tag{III-19}$$

where p_1 is the partial pressure of hydrogen, in atmospheres, before dissociation and

$$T_v = 6325^{\circ}K$$

$$T_d = 52,000^{\circ}K \tag{III-20}$$

representing the vibrational and dissociation energies of the hydrogen molecule, respectively. After dissociation, the hydrogen partial pressure (atoms + molecules) is

$$P_2 = (n_a + n_m) \ kT = (2\beta* + 1 - \beta*) \ n_1 \ kT$$

$$= (1 + \beta*) \ p_1 \tag{III-21}$$

where n_1 is the number density of molecules before dissociation and n_a, n_m are the number densities of atoms and molecules after dissociation. Similarly, the partial pressure of cesium (partially ionized) is $(1 +\beta) \ p_s$, so the chamber pressure is

$$p_c = (1 + \beta) \ p_s + (1 + \beta *) \ p_1 \tag{III-22}$$

which allows Eq. (III-19) to be written

$$\left(\frac{1}{\beta*2} - 1\right)^{-1} = 4.477 \frac{T^{3/2} (1-e^{-T_v/T}) e^{-T_d/T}}{P_c - (1 + \beta) P_s} \tag{III-23}$$

For typical chamber pressures (>20 atm), the cesium partial pressures shown in Fig. III-9 have a negligible effect on the dissociation of hydrogen, which is shown as a function of temperature in Fig. III-10 for $p_c = 20$ atm and 30 atm.

b. **Exhaust Velocity and Dissociation Losses**

The total enthalpy in the thrust chamber is

$$H_c = \sum_i (E_i + N_i \epsilon_i) + p_c V_c \tag{III-24}$$

where E_i is the total internal energy of species i, N_i is the total number in the chamber of this species, ϵ_i is the dissociation or ionization energy, and V_c is the chamber volume.

The total mass of gas in the chamber is

$$m = \rho V_c$$
$$= \frac{V_c}{RT} \sum_i M_i P_i \tag{III-25}$$

where ρ is the gas density, R is the gas constant, M_i and p_i are the atomic (or molecular) weight and partial pressure of species i. The enthalpy/unit mass is then

$$h_c = H_c/m = \frac{RT}{\sum\limits_i M_i P_i} \left[p_c + \frac{1}{V_c} \sum_i (E_i + N_i \epsilon_i)\right] \tag{III-26}$$

The species present are

      i) Hydrogen molecules

      ii) Hydrogen atoms

     iii) Cesium atoms

     iv) Cesium ions

      v) Electrons
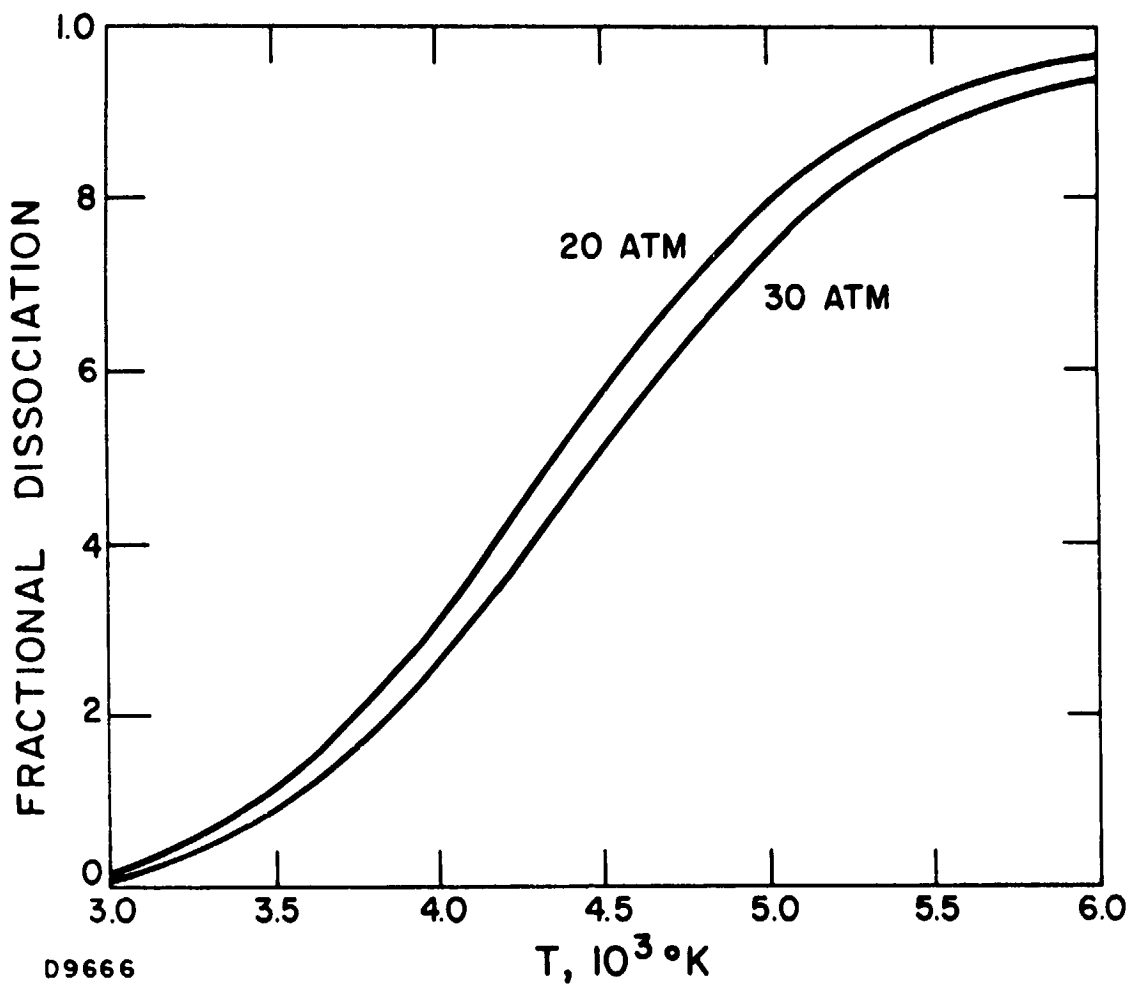
Fig. III-10   Dissociation of Hydrogen

Taking these in order, we have

$$i) \quad E_1 = N_1 kT \left[\frac{5}{2} + \frac{T_v}{T} \left(e^{T_v/T} - 1 \right)^{-1} \right] \qquad \text{(III-27a)}$$

$$\epsilon_1 = 0 \qquad \text{(III-27b)}$$

where T_v is given by Eq. (III-20).

$$ii) \quad E_2 = \frac{3}{2} N_2 kT \qquad \text{(III-28a)}$$

$$\epsilon_2 = 2.239 \text{ eV}$$

$$= kT_d' \qquad \text{(III-28b)}$$

where

$$T_d' = 26,000^\circ K \qquad \text{(III-28c)}$$

The value of T_d' is half that of T_d (Eq. (III-20)), because the dissociation energy is divided between the two atoms produced.

$$iii) \quad E_3 = \frac{3}{2} N_3 kT \qquad \text{(III-29a)}$$

$$\epsilon_3 = 0 \qquad \text{(III-29b)}$$

$$iv) \quad E_4 = \frac{3}{2} N_4 kT \qquad \text{(III-30a)}$$

$$\epsilon_4 = kT_i \qquad \text{(III-30b)}$$

Here $T_i = 45,178^\circ K$, as in Eq. (III-13), because the cesium ionization energy is accounted for by assuming it is all carried by the ions.

$$v) \quad E_5 = \frac{3}{2} N_5 kT \qquad \text{(III-31a)}$$

$$\epsilon_5 = 0 \qquad \text{(III-31b)}$$

In these expressions

$$N_1 kT = (1-\beta^*) p_1 V_c$$

$$N_2 kT = 2\beta^* p_1 V_c$$

$$N_3 kT = (1-\beta)p_s V_c$$

$$N_4 kT = \beta p_s V_c$$

$$N_5 kT = \beta p_s V_c \qquad\qquad \text{(III-32)}$$

$$\frac{1}{V_c} \sum_i (E_i + N_i \epsilon_i) = \left[(1-\beta^*)\left(\frac{5}{2} + \frac{T_v}{T}\left(e^{T_v/T} -1 \right)^{-1} + 2\beta^*\left(\frac{3}{2} + \frac{T_d'}{T} \right) \right) \right] p_1$$

$$+ \left[\frac{3}{2} + \left(\frac{3}{2} + \frac{T_i}{T} \right)\beta \right] p_s \qquad\qquad \text{(III-33)}$$

The partial pressures of the various species are obtained from Eq. (III-32), to give

$$\sum_i M_i p_i = \left[2(1-\beta^*) + 2\beta^* \right] p_1 + M_s(1 - \beta + \beta) p_s$$

$$= 2p_1 + M_s p_s \qquad\qquad \text{(III-34)}$$

where $M_s = 132.9$ is the atomic weight of the seedant and terms involving the atomic weight of the electron have been neglected.

Inserting these results in Eq. (III-26), the chamber enthalpy/unit mass is

$$h_c = \frac{RT}{2p_1 + M_s p_s} \left\{ p_c + \left[(1-\beta^*)\left(\frac{5}{2} + \frac{T_v}{T}\left(e^{T_v/T} -1 \right)^{-1} \right) + 2\beta^*\left(\frac{3}{2} + \frac{T_d'}{T} \right) \right] p_1 \right.$$

$$\left. + \left[\frac{3}{2} + \left(\frac{3}{2} + \frac{T_i}{T} \right)\beta \right] p_s \right\} \qquad\qquad \text{(III-35)}$$

It is now assumed that the vibrational and dissociation energy of the hydrogen freezes at the chamber temperature during the expansion in the nozzle. This is a worst-case condition, valid for sufficiently small nozzles. For simplicity, a matched expansion into a good vacuum is assumed, so that the exit temperature $T_e \approx 0$. Since cesium recombination is a rapid process, it is assumed that $\beta \approx 0$ at the nozzle exit.

Under these conditions, the enthalpy/unit mass at the exit consists only of the frozen energy, which may be obtained from Eq. (III-35) by picking out the terms in T_v and T_d':

$$h_e = \frac{R}{2p_1 + M_s p_s}\left[(1-\beta^*)\, T_v\Big/\left(e^{T_v/T}-1\right) + 2\beta^* T_d'\right]p_1 \qquad \text{(III-36)}$$

The ideal exhaust velocity (i.e., neglecting other losses) is then

$$c^2 = 2(h_c - h_e)$$

$$= \frac{2RT}{2p_1 + M_s p_s}\left\{p_c + \frac{1}{2}(5+\beta^*)\,p_1 + \left[\frac{3}{2}+\left(\frac{3}{2}+\frac{T_i}{T}\right)\beta\right]p_s\right\} \qquad \text{(III-37)}$$

In this equation, p_1 may be eliminated by means of Eq. (III-22), to yield

$$c^2 = \frac{2RT}{2p_c + (M_s\,(1+\beta^*) - 2\,(1+\beta)p_s}\left(\frac{1}{2}(7+3\beta^*)p_c\right.$$

$$\left. + \left\{\left[\left(\frac{T_i}{T}+1\right)\beta^*+\frac{T_i}{T}-1\right]\beta - (1-\beta^*)\right\}p_s\right) \qquad \text{(III-38)}$$

which allows the exhaust velocity to be plotted as a function of chamber temperature, using the values of β, β^* and p_s obtained from Eq. (III-14), Eq. (III-23) and Eq. (III-13). The results are shown in Fig. III-11, for several values of chamber pressure and design absorption length. Curve IV shows the exhaust velocity achieved with hydrogen alone, neglecting the seedant altogether (i.e., it is the performance which might be obtained if pure hydrogen was heated by some other means). The rapid drop-off in exhaust velocity as the chamber temperature is lowered, when cesium is present, is due to the rapid increase in the concentration of seedant which is required, as shown in Fig. III-9.

Figure III-12 shows the mass fraction of seedant in the engine, which is readily obtained as

$$\dot m_s/(\dot m_s + \dot m_1) = M_s\, p_s/(2p_1 + M_s\, p_s) \qquad \text{(III-39)}$$

where $\dot m_s$ and $\dot m_1$ are the mass flow rates of cesium and hydrogen, respectively. Without large increases in chamber pressure, the lowest temperature which can be used with a 2 cm absorption length is 3250°K, when the exhaust is in fact all cesium.

A different presentation of these data is useful in scaling the physical size of the engine. Equation (III-38) may be written

$$\left[K_1 - K_2\beta\right]p_s = \left(7 + 3\beta^* - \frac{2T^*}{T}\right)p_c \qquad \text{(III-40)}$$

-56-
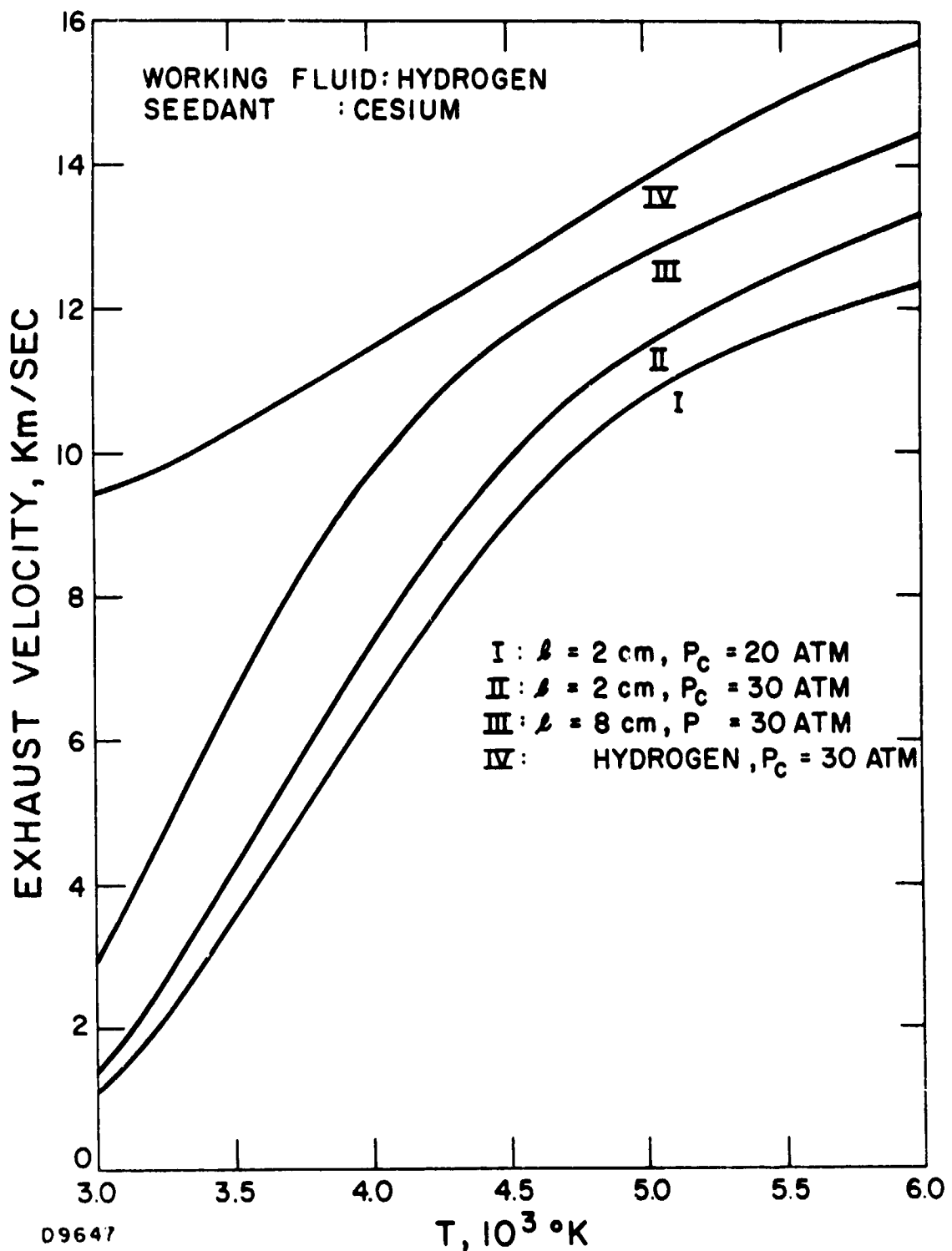
Fig. III-11   Exhaust Velocity vs Temperature
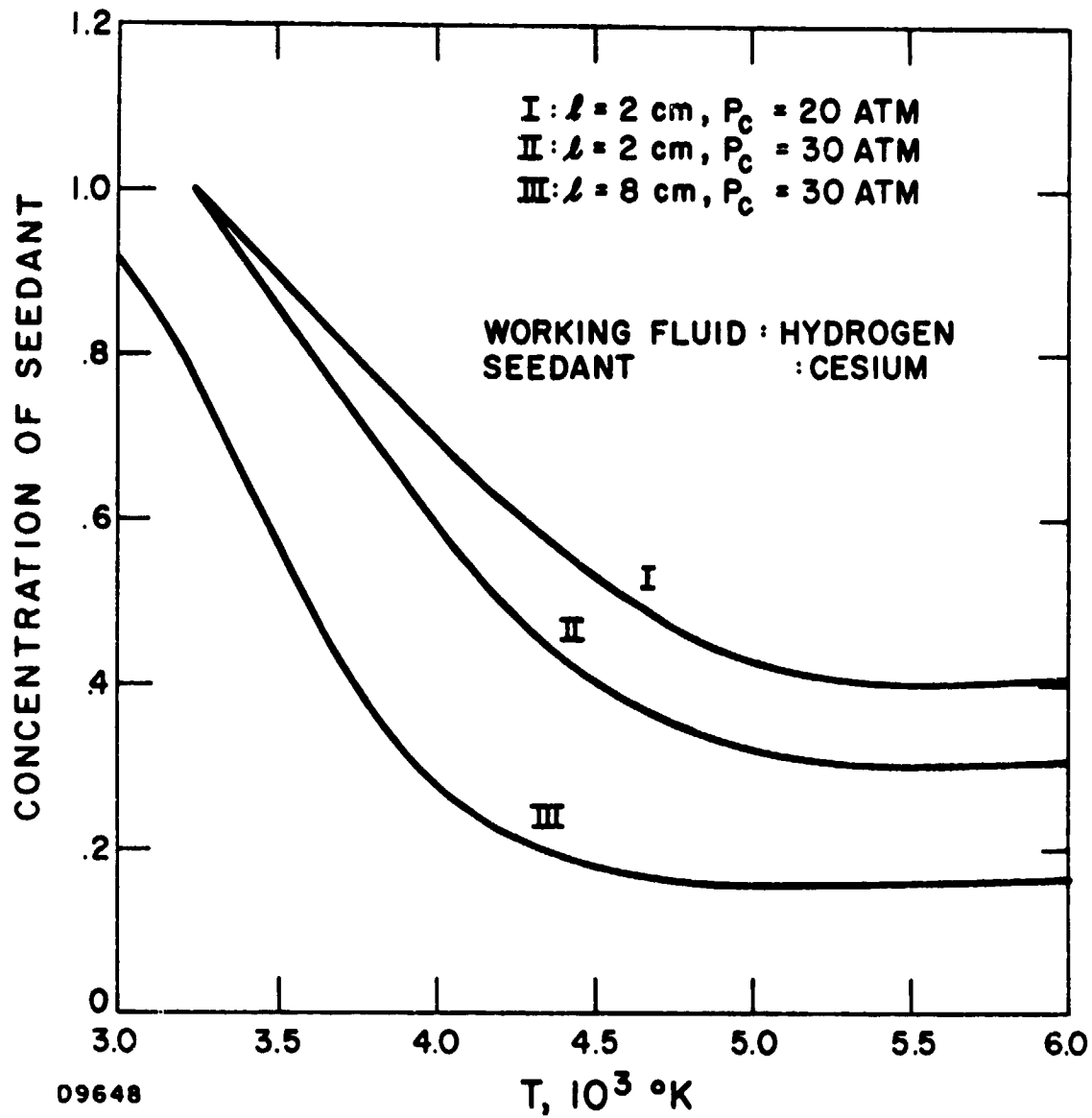
Fig. III-12   Seedant Mass Fraction

09648

-58-

where

$$T* = c^2/R \tag{III-41}$$

$$K_1 = (M_s (1 + \beta*) - 2)\frac{T*}{T} + 2 (1 - \beta*) \tag{III-42}$$

$$K_2 = 2\left[(T* + T_i)/T - 1 + \left(\frac{T_i}{T} + 1\right)\beta*\right] \tag{III-43}$$

Substituting for p_s from Eq. (III-13),

$$\left[K_1 - K_2\beta\right](1 - \beta)/\beta^2 = 3.042 \times 10^6\, p_c\left(7 + 3\beta* - \frac{2T*}{T}\right)T^{-5/2}e^{T_i/T}$$

$$= df\, K_3 \tag{III-44}$$

or

$$(K_2 - K_3)\beta^2 - (K_1 + K_2)\beta + K_1 = 0 \tag{III-45}$$

This equation allows calculation of the degree of ionization of the seedant which is required to achieve a given exhaust velocity, as a function of the chamber temperature. Equations (III-13) and (III-14) then give the corresponding values of seedant partial pressure and the absorption length.

Figure III-13 shows the absorption length required to achieve a specific impulse of 800 seconds as a function of temperature, for a chamber pressure of 30 atm. Since the thrust chamber dimensions must be at least of the order of the absorption length, it is clear that small engines of this performance must operate at high temperatures.

The corresponding partial pressure of seedant is shown in Fig. III-14 as a function of operating temperature. It is noteworthy that it varies only from 0.4 atm to 0.1 atm as the absorption length is increased from 1 cm to infinity.

A measure of the dissociation losses may be obtained as the ratio of h_e (from Eq. (III-36)) to the kinetic energy $1/2\, c^2$ per unit mass in the exhaust:

$$2h_e/c^2 = \frac{2p_1}{T*(2p_1 + M_s p_s)}\left[(1 - \beta*)\, T_v\Big/\left(e^{T_v/T} - 1\right) + 2\beta*\, T'_d\right] \tag{III-46}$$
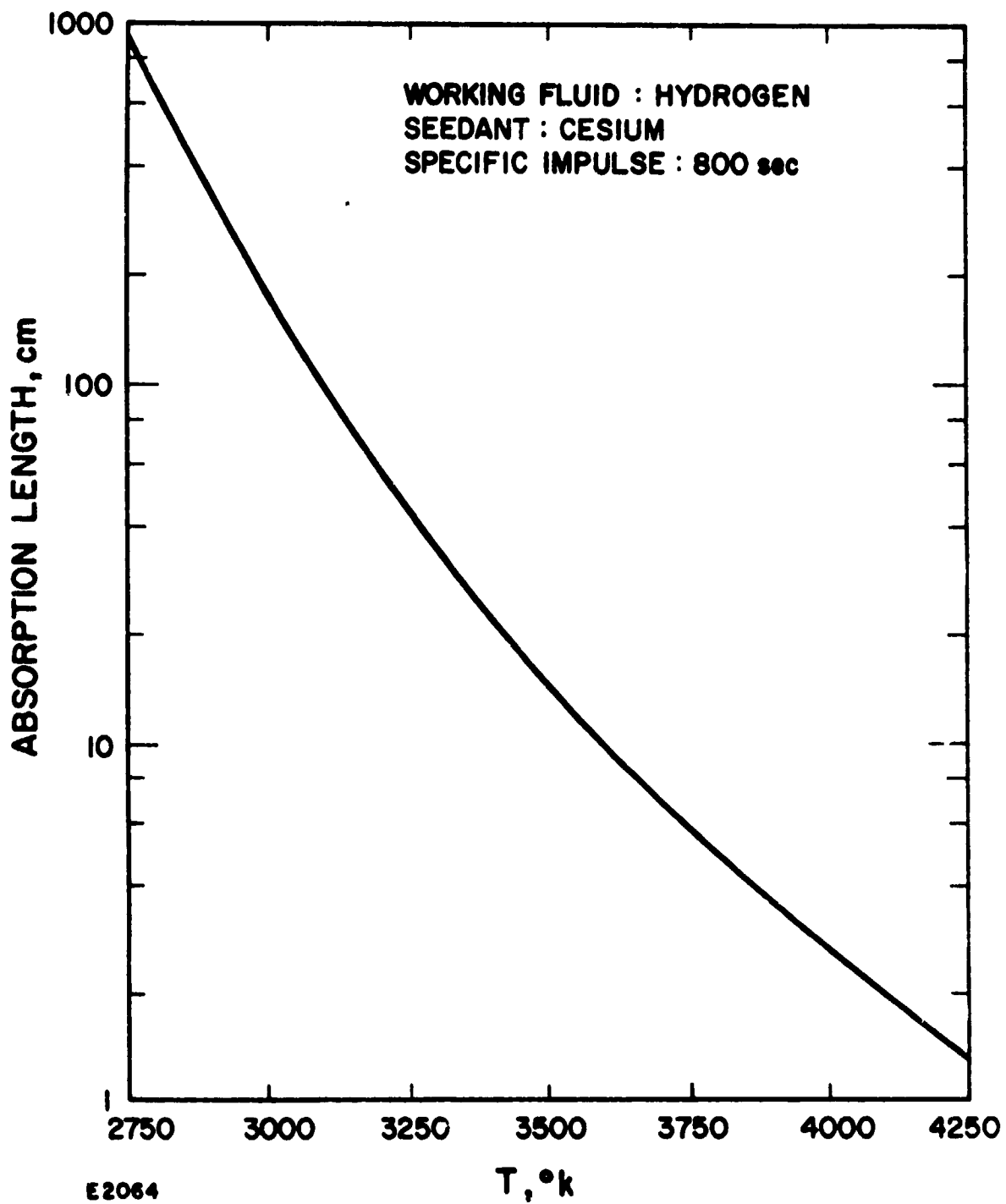
Fig. III-13   Absorption Length vs Chamber Temperature

WORKING FLUID: HYDROGEN
SPECIFIC IMPULSE : 800 sec
SEEDANT : CESIUM

E2063

Fig. III-14   Seedant Partial Pressure

This expression is plotted as a function of temperature in Fig. III-15, for I_{sp} = 800 sec., p_c = 30 atm. A value of unity means that, under the assumption that the exhaust composition freezes at the chamber temperature, half the exhaust energy is wasted. Comparison with Fig. III-13 shows that small engines can suffer serious inefficiencies from this effect. In larger engines, where the exhaust can be expected to freeze at a lower temperature, this analysis greatly overestimates the losses. In large engines, as a matter of fact, the capability of hydrogen to store enthalpy in the form of vibration and dissociation energy is a positive advantage, as it allows the desired specific impulse to be achieved at a lower chamber temperature.

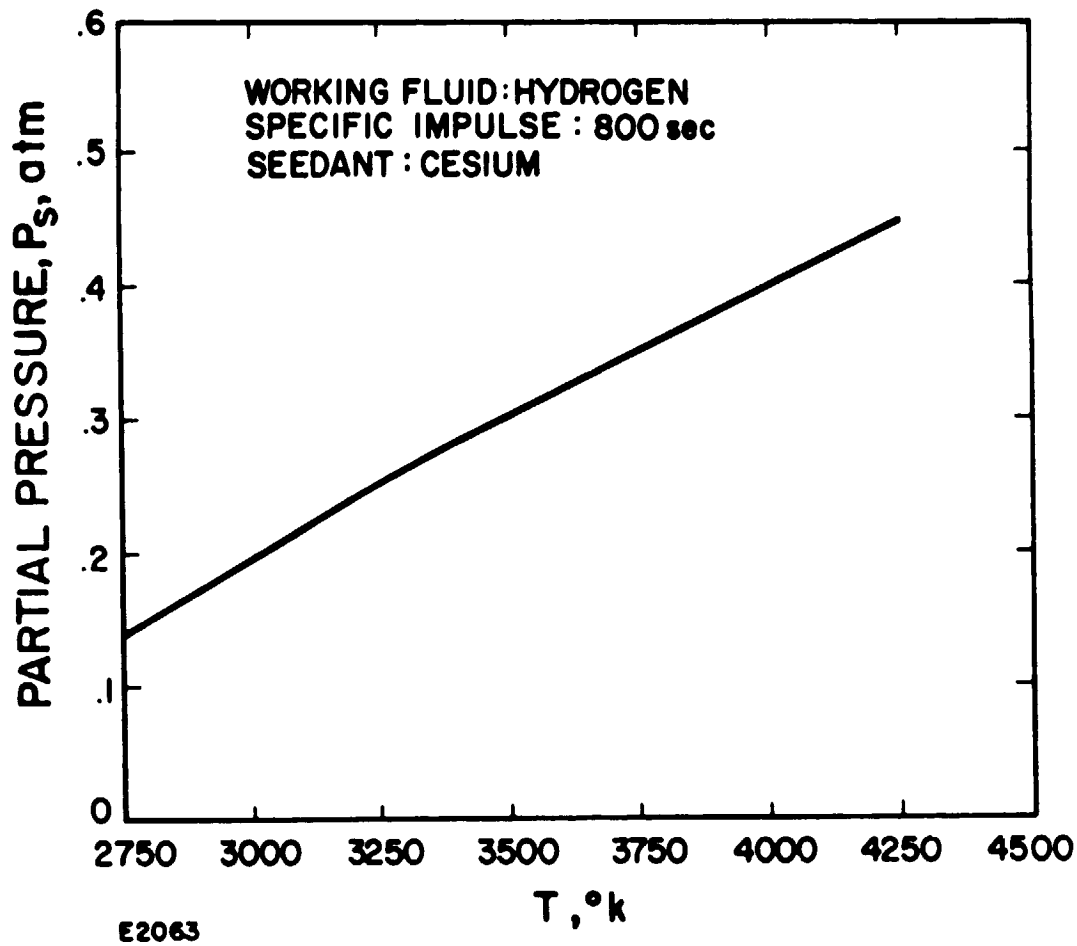One other possible problem with hydrogen as a working fluid should be mentioned at this point. The operating temperatures are generally below that for a minimum in the partial pressure of seedant [cf. Fig. III-9] . This means that, if the temperature of a small parcel of gas in the laser beam increases slightly, its opacity will increase and the rate of deposition of energy will also increase. If the time constant for mixing of the gases in the thrust chamber is long compared to that for heating the gas, it is thus possible for a hot spot to be generated where the seeded gas enters the laser beam. In such a case, the engine would operate in a fashion similar to an arcjet, the working fluid being passed through a small region of very high temperature, which could be expected to increase radiative power losses to the walls of the chamber. Whether or not this phenomenon will occur depends on the details of the mixing process, and its significance depends on the power level, chamber wall reflectivity, etc. These effects have not yet been studied in detail.

c. Thermal Losses

Heat losses to the chamber walls caused by (forced) convection depend on the transport of gas of high enthalpy from the central region of the chamber, and hence on the details of the mixing process. In conventional rockets, changing the injector design can change the local wall flux by an order of magnitude.[14] As noted above, radiative losses also depend on the rapidity of mixing. Truly satisfactory analytical techniques do not exist for estimating the magnitude of these effects, and the problem is certainly quite intractable until the design of effects, and the problem is certainly quite intractable until the design of the seeded-propellant injector has been determined. However, in the test engine, it is clear that convective losses can be minimized by attempting to maintain laminar flow in the chamber, to the extent which is compatible with the absorption conditions in the laser beam. In the design discussed in Section III.2, unlike a chemical rocket, turbulent mixing in the chamber is required only to overcome the dilution due to the stream of unseeded propellant emerging from the window isolation tube, and to distribute the enthalpy deposited by the laser beam, if the absorption region is localized.

WORKING FLUID : HYDROGEN
SEEDANT : CESIUM
SPECIFIC IMPULSE : 800 SEC

E2065
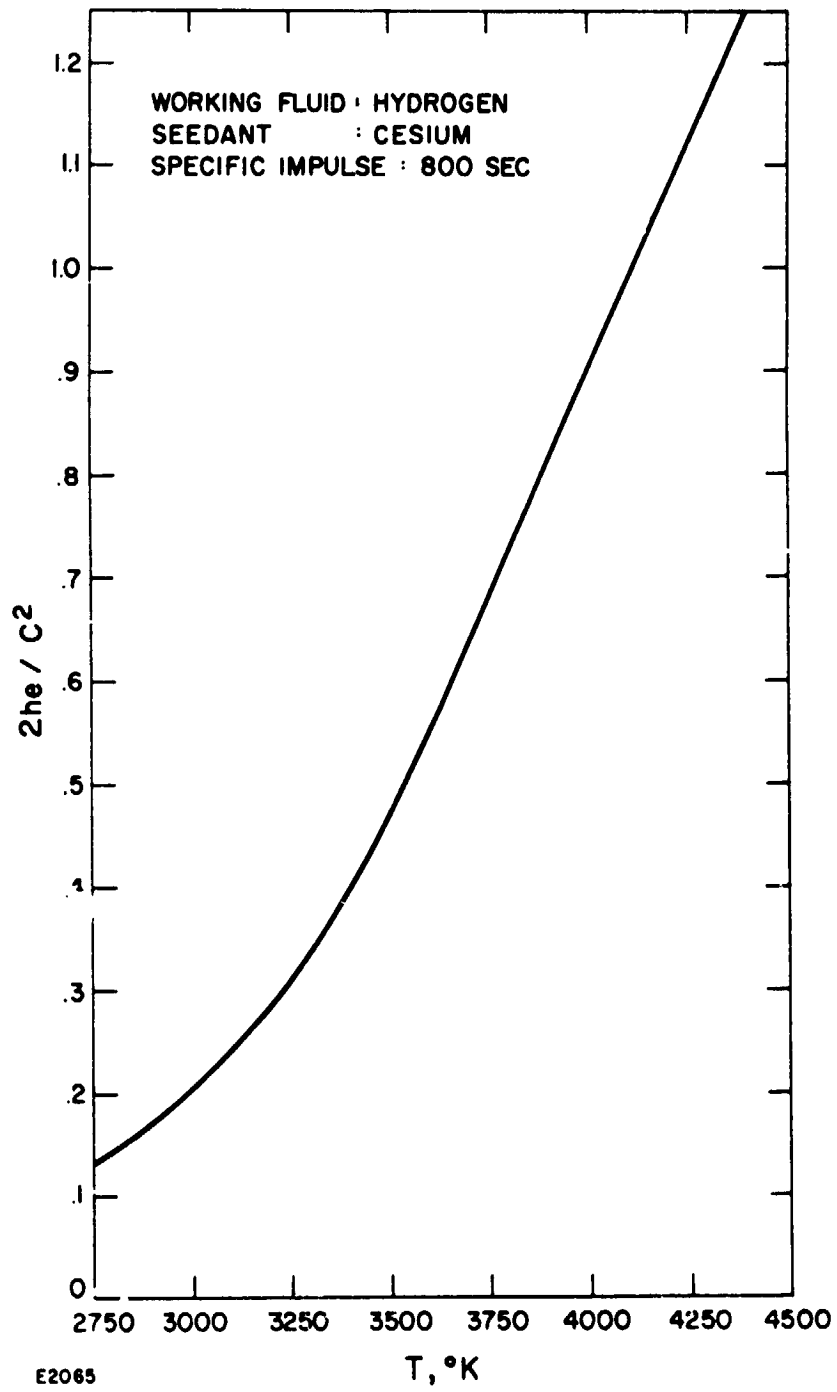
Fig. III-15   Dissociation Losses

-63-

For present purposes, a lower bound to the total heat transfer through the walls may be obtained by assuming laminar flow. In this case, the heat transfer mechanisms are conduction and diffusion through the boundary layer at the chamber wall, with recombination of dissociated hydrogen in the cooler regions there. In order to avoid undue optimism, worst-case conditions will be assumed in the analysis: for example, the boundary layer will be considered to be in local thermodynamic equilibrium everywhere.[15]

The local heat transfer across streamlines, due to conduction and diffusion, is given by[16]

$$J = -\frac{\lambda}{\overline{c}_p} \left[\frac{\partial h}{\partial r} + (Le - 1) \sum h_1 \frac{\partial k_i}{\partial r} \right] \qquad \text{(III-47)}$$

where k_i is the local mass fraction and h_i the local enthalpy/unit mass of the ith species present, h is the total local enthalpy, λ is the thermal conductivity, the mean constant-pressure specific heat is given in terms of the individual specific heats c_{pi} by

$$\overline{c}_p = \sum k_i c_{pi} \qquad \text{(III-48)}$$

and Le is the Lewis number

$$Le = \rho D_{12} \overline{c}_p / \lambda \qquad \text{(III-49)}$$

where ρ is the density and D_{12} the binary diffusion coefficient.

A very convenient approximation, and one that has been shown usually to introduce little error,[17] is to assume that the Lewis number is unity. Some justification for this assumption may be obtained by calculating Le for a binary mixture of hydrogen atoms and molecules, for which

$$\rho = (2\beta* + 2(1 - \beta*)) nm = 2 nm \qquad \text{(III-50)}$$

where n is the number density of hydrogen molecules before dissociation, m is the mass of a hydrogen atom, and β^* is the fractional dissociation. The conductivity is given by the Eucken formula[18]

$$\lambda = \frac{1}{4} (9\gamma - 5)\mu c_v \qquad (III-51)$$

where μ is the viscosity and c_v the constant-volume specific heat. The viscosity is[18]

$$\mu = m' <v>/(8^{1/2} \pi d^2) \qquad (III-52)$$

where m' is the mass of a molecule (or atom), the average thermal velocity is

$$<v> = (8kT/\pi m')^{1/2} \qquad (III-53)$$

and d is the effective molecular (or atomic) diameter.

According to the Wassiljewa approximation to the conductivity of gas mixtures,[19] the conductivity may be taken as that of the hydrogen molecules alone, in regions where the dissociation is small.

The diffusion coefficient is[18]

$$D_{12} = 3<g> / (32n\overline{d}^2) \qquad (III-54)$$

where $\overline{d}$ is an effective collision diameter and

$$<g> = (8kT/\pi m_{12})^{1/2} \qquad (III-55)$$

with

$$m_{12} = (1/m + 1/2\ m)^{-1}$$
$$= \frac{2}{3} m \qquad (III-56)$$

as the reduced mass for collisions between the two species.

Finally, for a mixture of hydrogen atoms and molecules,

$$\overline{c}_p = (1 - \beta^*)c_{p1} + \beta^* c_{p2} \tag{III-57}$$

where the suffixes 1, 2 refer to hydrogen molecules, atoms, respectively.

Inserting all these results in Eq. (III-49) gives

$$Le \simeq 1.06\left(\frac{d}{\overline{d}}\right)^2 (1 + 0.43\beta^*) \tag{III-58}$$

The assumption of $Le \simeq 1$ is borne out by more detailed calculations by Rosner.[20]

In any case, with this approximation, Eq. (III-47) takes the simple form

$$J = -\frac{\lambda}{\overline{c}_p} \frac{\partial h}{\partial r} \tag{III-59}$$

Because of cylindrical symmetry in the chamber, J is actually a radial vector. The equation of continuity for the energy flow is then

$$\nabla \cdot \underline{J} = \frac{1}{r} \frac{\partial}{\partial r} (rJ) = q \tag{III-60}$$

where q is the net rate of absorption of heat (from the laser beam) per unit volume. The total power lost through the wall is, by Gauss's theorem,

$$P_w = P_o - P_e$$

$$= \int_{A_w} \underline{J} \cdot d\underline{A} = \int_{V_c} \nabla \cdot \underline{J} \, dV$$

$$= \int_{V_c} q \, dV \tag{III-61}$$

where P_o is the total power received from the laser, P_e is that carried away through the nozzle and A_w is the chamber wall area. The average value of q is thus the total thermal losses through the wall divided by the chamber volume. In order to solve the differential equation, it is assumed that this is the value of q everywhere in the chamber -- i.e., that it does not vary with position. This is again a worst-case assumption, for the heat

-66-

transfer will be less if the heating is confined to the laser beam, in the central part of the chamber.

For this approximate calculation, it is sufficient to give λ and $\bar{c}_p$ in Eq. (III-59) average values, to be computed later. Then Eq. (III-60) reads

$$\frac{1}{r} \frac{\partial}{\partial r} \left(r \frac{\partial h}{\partial r} \right) + \frac{q\bar{c}_p}{\lambda} = 0 \qquad \text{(III-62)}$$

which has the solution

$$h = \frac{q\bar{c}_p}{4\lambda} \left[B - r^2 \right] \qquad \text{(III-63)}$$

The value of the constant B is determined by requiring that the enthalpy at the wall, h_w, have a specified value, corresponding to the design wall temperature. More specifically, the wall flux is

$$J_w = -\frac{\lambda}{\bar{c}_p} \left(\frac{\partial h}{\partial r}\right)_{r=a} = \frac{1}{2} qa = H_w (T_w - T_s) \qquad \text{(III-64)}$$

where H_w is the wall conductance and T_s the coolant temperature. The assumption of local thermodynamic equilibrium requires that h_w be specified as soon as T_w is given. Thus

$$B = a^2 + \frac{4\lambda}{q\bar{c}_p} h_w \qquad \text{(III-65)}$$

On the center line, Eq. (III-63) gives

$$h_c = \frac{q\bar{c}_p}{4\lambda} a^2 + h_w$$

or

$$q = \frac{4\lambda}{\bar{c}_p a^2} \left[h_c - h_w \right] \qquad \text{(III-66)}$$

so that the wall heat flux is given by Eq. (III-64) as

$$J_w = \frac{2\lambda}{\bar{c}_p a} \left[h_c - h_w \right] \qquad \text{(III-67)}$$

In order to define an average temperature, at which to calculate λ and $\overline{c}_p$, it will be adequate to neglect the contributions of ionization, dissociation and vibration energy to the total enthalpy/unit mass. In this approximation

$$h = \sum k_i c_{pi} T = \overline{c}_p T \tag{III-68}$$

and Eq. (III-63) becomes

$$T = \frac{q}{4\lambda}\left[a^2 - r^2\right] + T_w \tag{III-69}$$

so that the average temperature is

$$\overline{T} = \frac{1}{a} \int_0^a T dr$$

$$= \frac{2}{3} \frac{q}{4\lambda} a^2 + T_w = \frac{1}{3}(2T_c + T_w) \tag{III-70}$$

where T_c is the center-line temperature, which will be taken as the chamber temperature, derived in the previous Section.

Strictly speaking, this analysis is applicable only to a very long, thin chamber, as end effects have been neglected. However, a rough approximation to the contribution to the thermal losses due to the ends of the chamber may be included by taking A_w as the total surface area of the cylindrical chamber:

$$A_w = 2\pi a (L + a) \tag{III-71}$$

Because of the optical design discussed in Section III. 2, the absorption length y in the chamber is related to its length by

$$L \simeq \frac{3}{2} y \tag{III-72}$$

so that, with Eq. (III-67), the total wall losses may be written

$$P_w = J_w A_w \simeq \frac{6\pi\lambda y}{\overline{c}_p}(1 + a/L)\left[h_c - h_w\right] \tag{III-73}$$

The five species present in the chamber are listed above in Eq. (III-27). For each species,

$$k_i c_{pi} = \frac{n_i m_i \gamma_i R}{M_i (\gamma_i - 1) \sum n_i m_i} = \frac{n_i \gamma_i R}{(\gamma_i - 1) \sum n_i M_i} \tag{III-74}$$

where n_i is the number density, m_i the molecular (or atomic) mass, M_i the atomic weight and γ_i the ratio of the specific heats. Since all species present are monatomic except the first (molecular hydrogen, which is diatomic), we take

$$\gamma_1 = 1.4$$

$$\gamma_i = 1.67 \ (i \neq 1) \tag{III-75}$$

Thus

$$\bar{c}_p = \left[\frac{7}{2} (1 - \beta^*) p_1 + \frac{5}{2} \left[2\beta^* p_1 + (1 + \beta) p_s \right] \right] R \Big/ \left[2 p_1 + M_s (1 + \beta) p_s \right]$$

$$= \left[\frac{1}{2} (7 + 3\beta^*) p_1 + \frac{5}{2} (1 + B) p_s \right] R \Big/ \left[2 p_1 + M_s (1 + \beta) p_s \right] \tag{III-76}$$

$$= \left[\frac{1}{2} (7 + 3\beta^*) p_c - (1 - \beta^*)(1 + \beta) p_s \right] R \Big/ \left[2 p_c + (M_s - 2(1 + \beta))(1 + \beta) p_s \right]$$

from Eq. (III-22). In using this expression, the value of p_s is to be determined by the methods of the last Section, but β and β^* are to be evaluated at $\bar{T}$, as given by Eq. (III-70).

For simplicity, it is again assumed that the conductivity is due to the molecular hydrogen alone. From Eqs. (III-51) and (III-53).

$$\lambda = \frac{1}{4\pi} \ 3/2 \left(\frac{9\gamma - 5}{\gamma - 1} \right) k \left(\frac{R}{M} \right)^{1/2} \frac{T_2^{1/2}}{d} \tag{III-77}$$

The effective diameter d of a hydrogen molecule is[18]

$$d \simeq 4.90 \times 10^{-8} \ T^{-0.1} \ \text{cm} \tag{III-78}$$

so that, in c.g.s. units (ergs/sec-cm-°K),

$$\lambda \simeq 315 \ T^{0.7} \tag{III-79}$$

The average temperature (Eq. (III-70)) should be used in this expression when it is inserted in Eq. (III-73).

Using Eq. (III-37), the thermal loss may be written

$$P_w = \frac{3\pi\lambda yc^2}{\bar{c}_p} (1 + a/L) (1 + 2h_e/c^2 - 2h_w/c^2) \qquad \text{(III-80)}$$

In the design shown in Fig. III-3, $a/L \simeq 0.13$. If we now consider variation in the length of the engine (and hence, by Eq. (III-72), the design absorption length), while keeping the shape of the chamber constant, Eq. (III-80) allows calculation of the variation in wall losses. Figure III-13 shows the absorption length required to give a specific impulse of 800 seconds as a function of the chamber temperature. Equation (III-46), with $T = T_c$, gives the dissociation and vibrational losses in the exhaust, and Eq. (III-35) with $T = T_w$ gives h_w. It is therefore convenient to calculate P_w as a function of the chamber temperature and then use Fig. III-13 to plot the wall losses as a function of absorption length. The results are shown in Fig. III-16, for $p_c = 30$ atm, $I_{sp} = 800$ sec., and $T_w = 1100^\circ K$. Also shown for comparison is the wall loss for a helium engine, which is discussed in Section III.6.

d. Optimum Size of the Test Engine

We are now in a position to compare the thermal and dissociation losses. The overall efficiency of the engine, taking into account only these losses, is

$$\eta = \frac{1}{2} \frac{\dot{m}c^2}{P_o} = 1 - \frac{1}{P_o}\left[P_w + \dot{m}h_e\right] \qquad \text{(III-81)}$$

which may be solved to give the propellant mass flow rate

$$\dot{m} = (P_o - P_w) / (\tfrac{1}{2} c^2 + h_e) \qquad \text{(III-82)}$$

Substituting this in the RHS of Eq. (III-81) gives

$$\eta = (1 - P_w/P_o)/(1 + 2h_e/c^2) \qquad \text{(III-83)}$$

which is plotted as a function of the design absorption length in Fig. III-17, for an input power level of 15 kW (Curve I). The optimum absorption length is seen to be about 3 cm.

The parameters of this engine are shown in Table III-1.

The low mass flow rate and thrust exhibited by this engine are, of course, a consequence of the low input power level. It is noteworthy that the calculated thermal flux through the chamber wall is only 180 watts/cm^2,
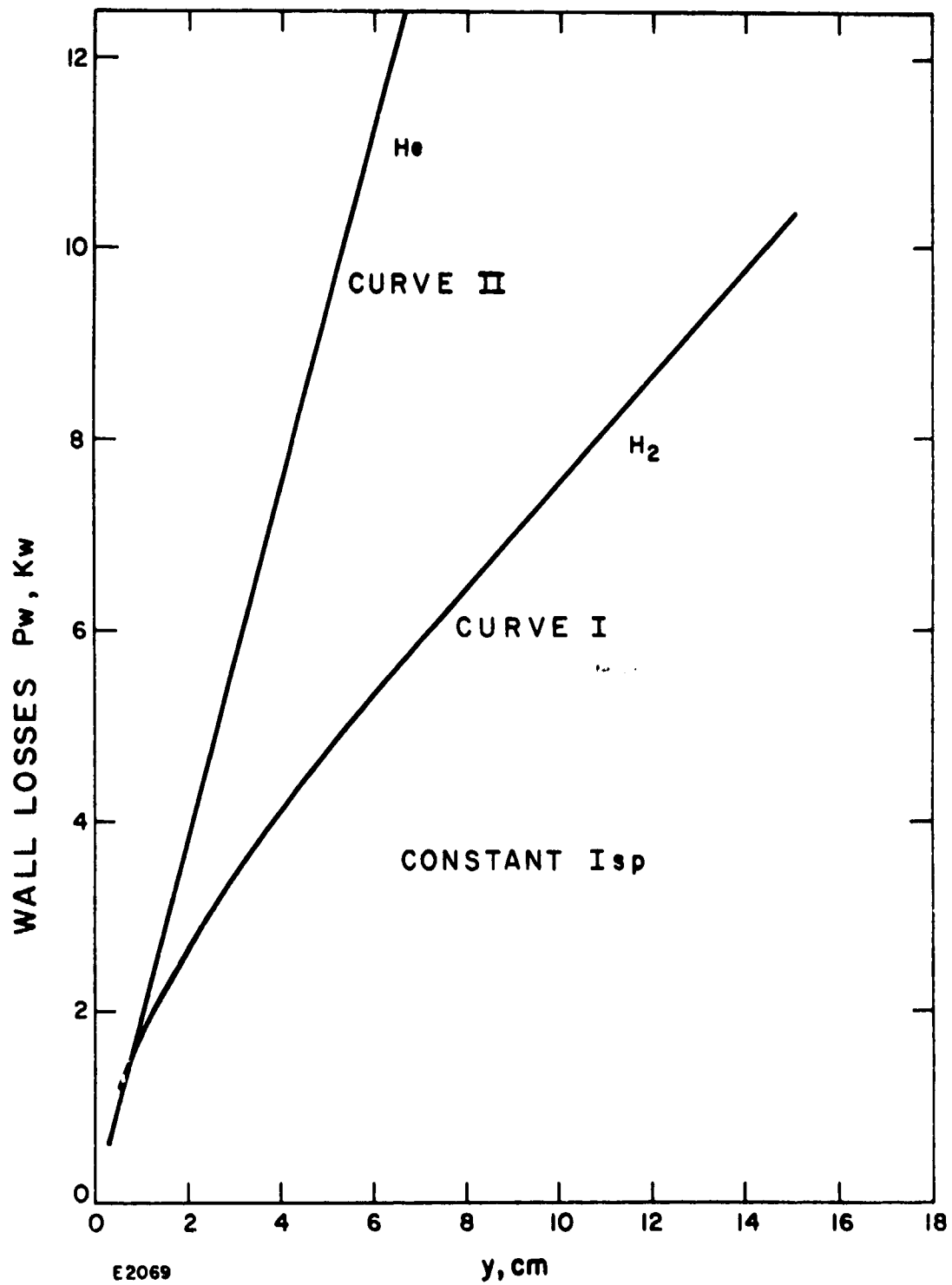
Fig. III-16   Wall Thermal Losses vs Absorption Length, Hydrogen
and Helium Engines
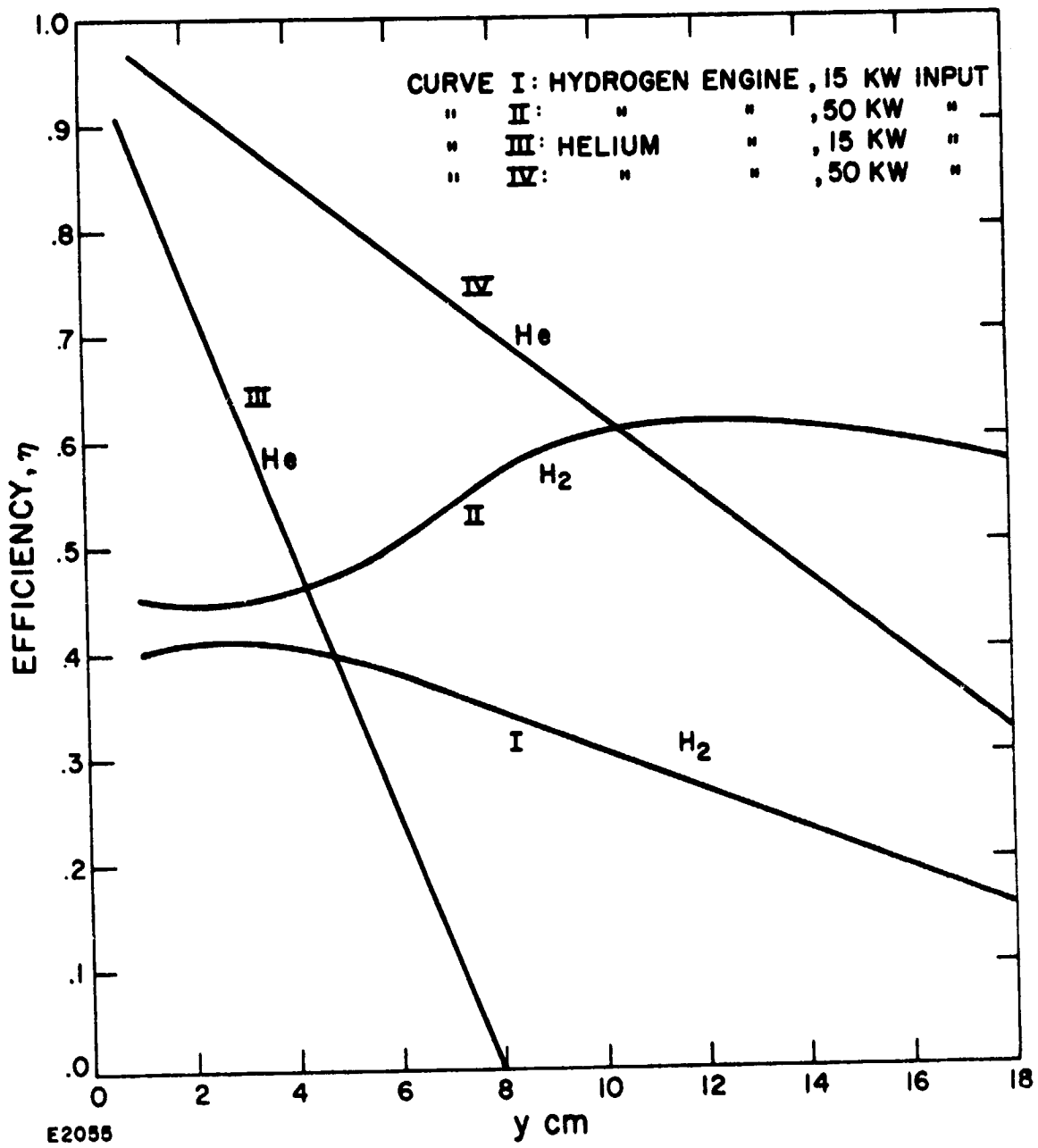
Fig. III-17   Efficiency of Engines vs Absorption Length

TABLE III-1

PARAMETERS OF THE HYDROGEN ENGINE

Input Power	15 kW
Specific Impulse	800 sec
Mass Flow Rate	0.2 gm/sec
Chamber Pressure	30 atm
Chamber Temperature	$3950^{\circ}K$
Wall Thermal Losses	3.4 kW
Dissociation Losses	5.4 kW
Power Efficiency	41%
Thrust	1.5 N = 0.35 lbw
Absorption Length	3 cm
Chamber Length	4.5 cm
Throat Area ($C_F = 1.7$)	$0.31 \ mm^2$
Throat Diameter	0.63 mm
$L^* = V_c/A_t$	53 cm
Wall Thermal Flux	$180 \ watts/cm^2$
Maximum Wall Thickness (Copper)	17 cm
Seedant Partial Pressure	0.39 atm

so that there should be no difficulty in cooling it. The wall thickness shown in the table was derived on the basis of 800°K drop across copper; the large value obtained raises the possibility of providing a copper heat sink rather than active cooling.

For comparison, the efficiency of an engine with an input power of 50 kW is also shown in Fig. III-17 (Curve II). The optimum efficiency is considerably higher and occurs at an absorption length of 13 cm, resulting in a reduction in the operating temperature of 400°K.

It should be noted that a more complete treatment of the thermal losses, taking into account the effect on the conductivity of the chamber gases of species other than molecular hydrogen and also convective losses, would increase the estimate of wall losses at any operating temperature, which would lower the efficiency and shift the optimum to shorter absorption lengths. However, since the maximum in Curve I, Fig. III-17 is broad and the dissociation losses are considerably larger than the wall losses, it is expected that these effects will affect the observed efficiency but not invalidate the calculation of the chamber dimensions.

As the input power is increased, the wall losses rapidly become insignificant. The exhaust products will freeze at a temperature well below chamber temperature if the nozzle throat is sufficiently large, greatly reducing the dissociation losses. For example, it is expected that the losses considered here would have a negligible effect on the overall efficiency at a power level of one megawatt.

The other curves in Fig. III-17 are discussed below.

6. USE OF HELIUM AS PROPELLANT

The analysis of operating conditions in the test engine is very much simplified if helium instead of hydrogen is used as the working fluid, because of the lack of dissociation and internal energy of the He atom. However, because of the increased atomic weight, the chamber temperature required for a given exhaust velocity will now be higher; it will, in fact, be above the minimum in the opacity map for cesium (Fig. III-9), for most exhaust velocities of interest. While this means that, in a cesium-seeded helium engine, the bulk heating process must be stable, it also suggests consideration of an alkali seedant of higher ionization temperature but lower atomic weight.

The alternative seedants are:

i) Rubidium, atomic weight 85.48, ionization temperature $T_i = 48,460°K$;

ii) Potassium, atomic weight 39.1, $T_i = 50,354°K$; and

iii) Sodium, atomic weight 22.99, $T_i = 59,625°K$

The best compromise between atomic weight and ionization temperature is probably potassium, although mixtures with sodium (NaK) could also be used. To obtain the ionization and partial pressure of these seedants as a function of temperature, for a given absorption length, the only change required in the analysis of Section III.4 is the substitution of the new value of T_i. The results for potassium are given in Fig. III-18, which is to be compared with Fig. III-9 for cesium.

The enthalpy/unit mass in the thrust chamber is given by Eq. (III-26), where now the species present are:

    i) Helium atoms

    ii) Seedant atoms

    iii) Seedant ions

    iv) Electrons

Since all of these are monatomic, the total thermal energy of the ith species is

$$E_i = \frac{3}{2} N_i kT \tag{III-84}$$

where N_i is the number present. In addition, each seedant ion carries an ionization energy

$$\epsilon_3 = kT_i \tag{III-85}$$

where $T_i = 45,178^{\circ}K$ (cesium) or $50,354^{\circ}K$ (potassium).

In Eq. (III-84),

$$N_1 kT = p_1 V_c$$

$$N_2 kT = (1 - \beta) p_s V_c$$

$$N_3 kT = N_4 kT = \beta p_s V_c \tag{III-86}$$

where, as before, p_s is the partial pressure of seedant, before ionization, and p_1 is the partial pressure of helium. Adding up the partial pressures,

$$p_c = p_1 + (1 + \beta) p_s \tag{III-87}$$

and

$$\sum_i M_i p_i = 4 p_1 + M_s p_s \tag{III-88}$$

-75-
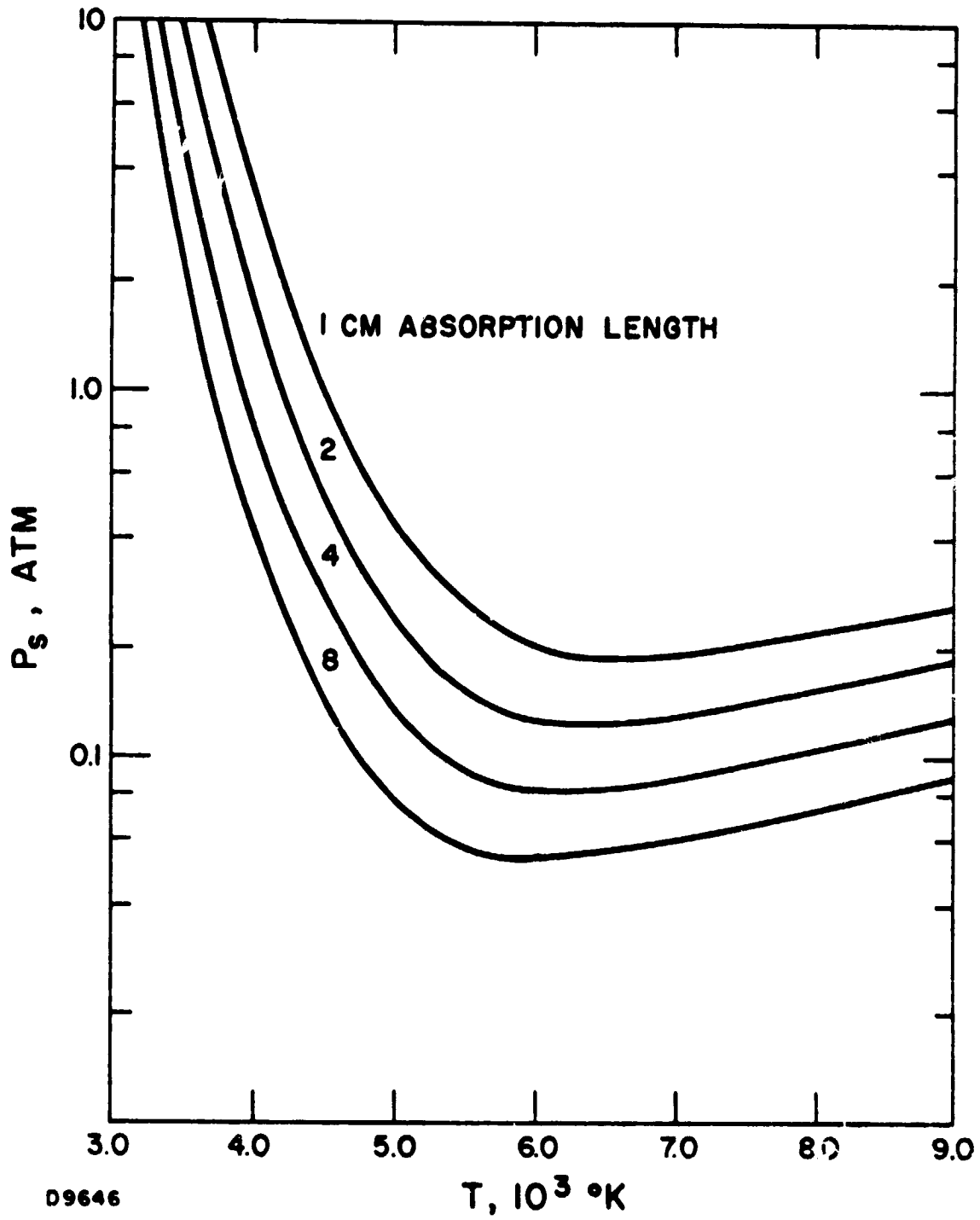
Fig. III-18   Opacity Map for Potassium

where the weight of electrons has again been neglected.

Since there are no dissociation losses, the ideal exhaust velocity is given by

$$c^2 = 2h_c$$

$$= \frac{2RT}{[4p_c + (M_s - 4 - 4\beta)p_s]} \left[\frac{5}{2} p_c + \left(\frac{T_i}{T}\right)\beta p_s \right] \qquad \text{(III-89)}$$

where Eq. (III-84) to Eq. (III-88) have been used in Eq. (III-26).

The exhaust velocity vs temperature curves are shown in Fig. III-19 for a helium engine with p_c = 30 atm and an absorption length of 2 cm, for both potassium and cesium seedants. At higher specific impulses, the use of potassium results in a chamber temperature which is 700°K to 1000°K lower than if cesium is used. Comparison with the "He alone" curve (which gives the exhaust velocity if helium is heated by some other means, in the absence of seedant) shows that, for specific impulses above about 700 sec, potassium is practically an ideal seedant for a helium engine. The reason for the improvement over cesium is seen in Fig. III-20, which shows the mass fraction of seedant required. The very much lower values for potassium at higher temperatures are due to its much lower atomic weight, compared to cesium.

As in the case of the hydrogen engine (cf Eq. (III-12) et seq), Eq. (III-89) may be solved, using Eq. (III-13), to give the ionization of potassium required to give a specified specific impulse, as a function of temperature, and then Eq. (III-14) gives the corresponding absorption length. At I_{sp} = 800 sec, however, Fig. III-19 indicates that the operating temperature is almost independent of absorption length. Carrying out the calculation shows, in fact, that the required temperature decreases only from 6150° to 5925°K as the absorption length is increased from 1 cm to infinity. For practical purposes, therefore, the chamber temperature of a potassium-seeded helium engine operating at the design specific impulse may be taken as approximately 6000°K, regardless of its size.

For use in the design of propellant feed systems for small helium engines, Fig. III-21 shows the partial pressure of potassium required for p_c = 30 atm and I_{sp} = 800 sec.

Turning now to the thermal design, the conductivity of helium is given by Eq. (III-77), with γ = 1.67 and[18]

$$d = 4.07 \times 10^{-8} \, T^{-0.14} \, \text{cm} \qquad \text{(III-90)}$$

or, in c.g.s. units (ergs/sec-cm-°K),

$$\lambda \simeq 260 \, T^{0.78} \qquad \text{(III-91)}$$
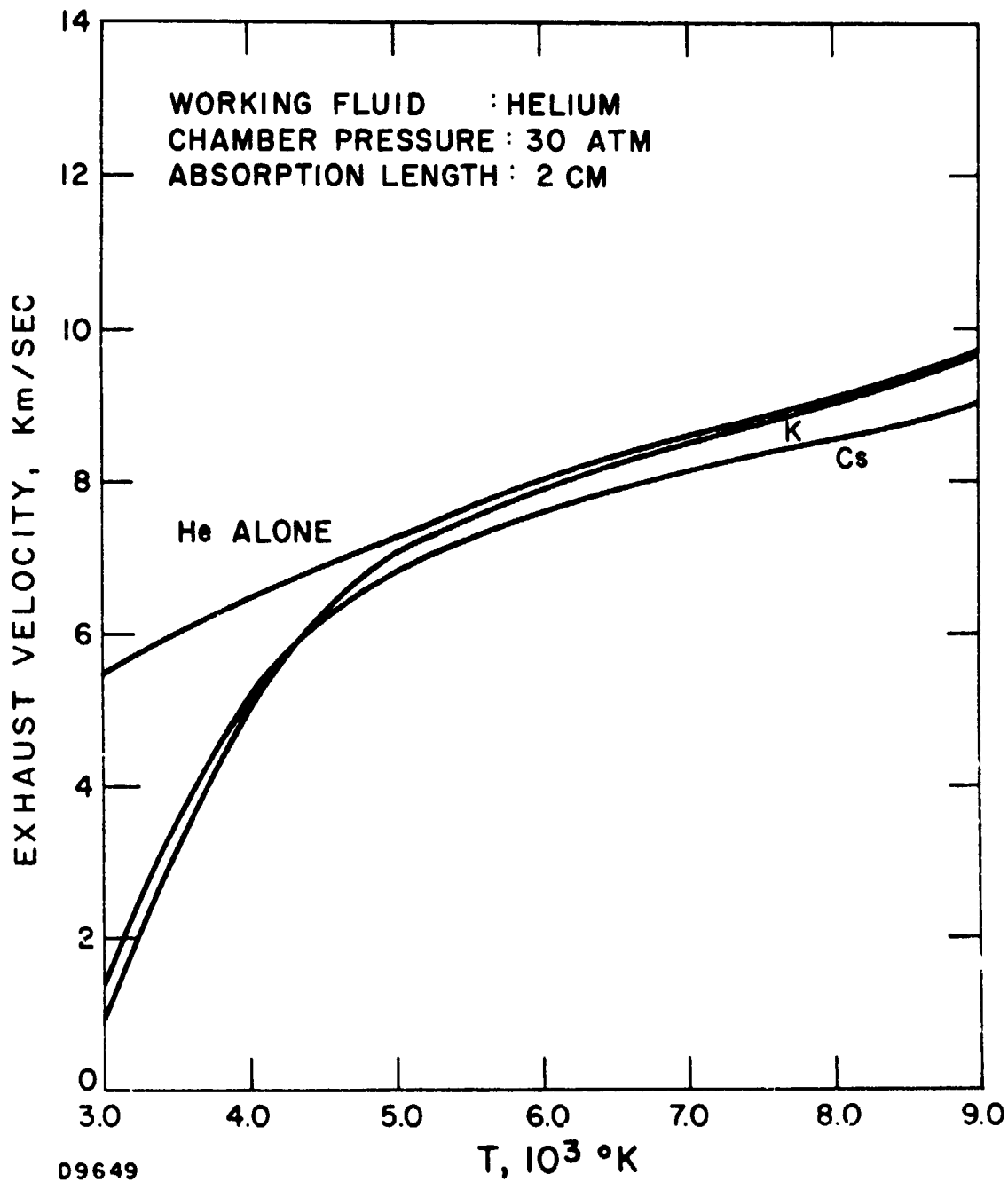
Fig. III-19   Exhaust Velocity vs Temperature
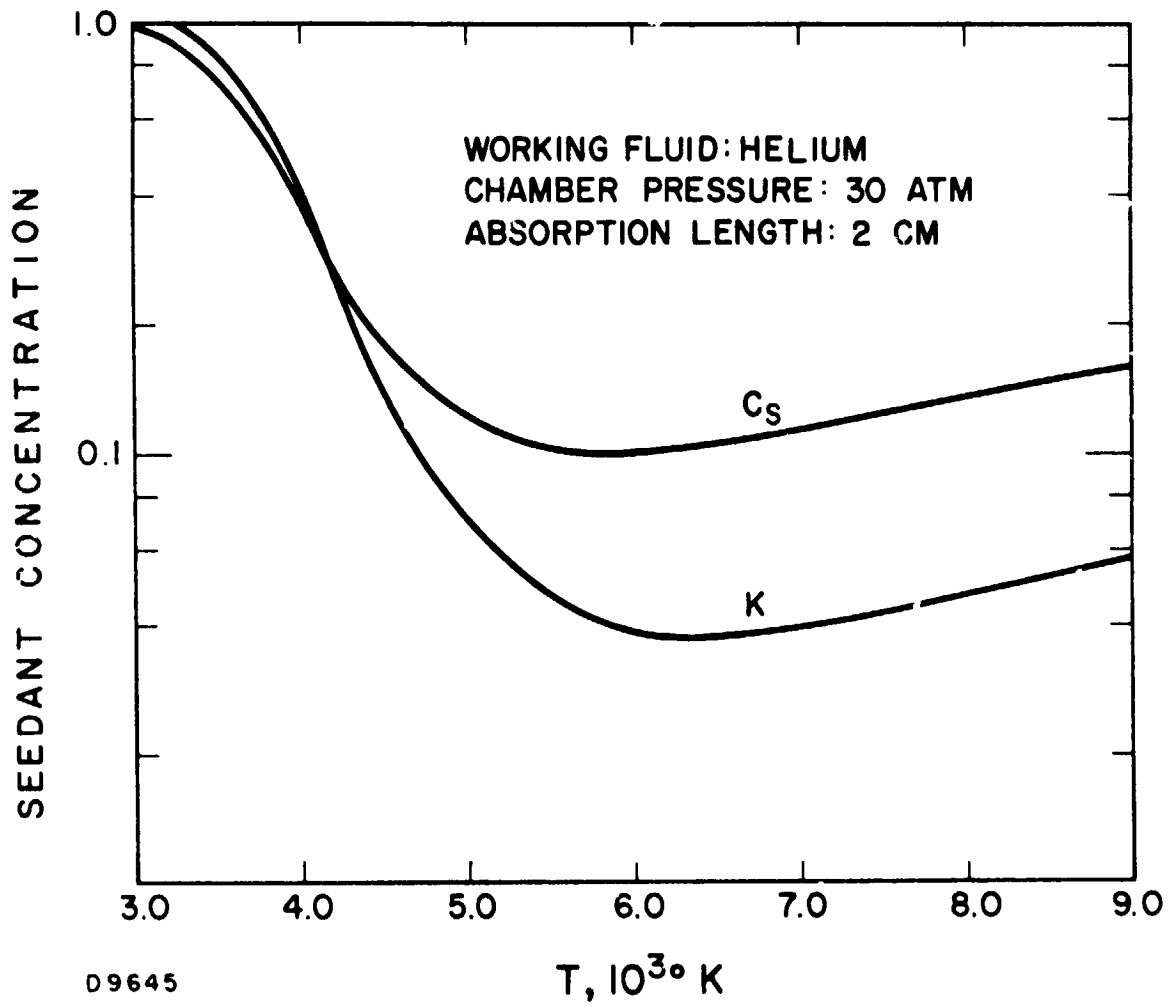
Fig. III-20   Seedant Mass Fraction
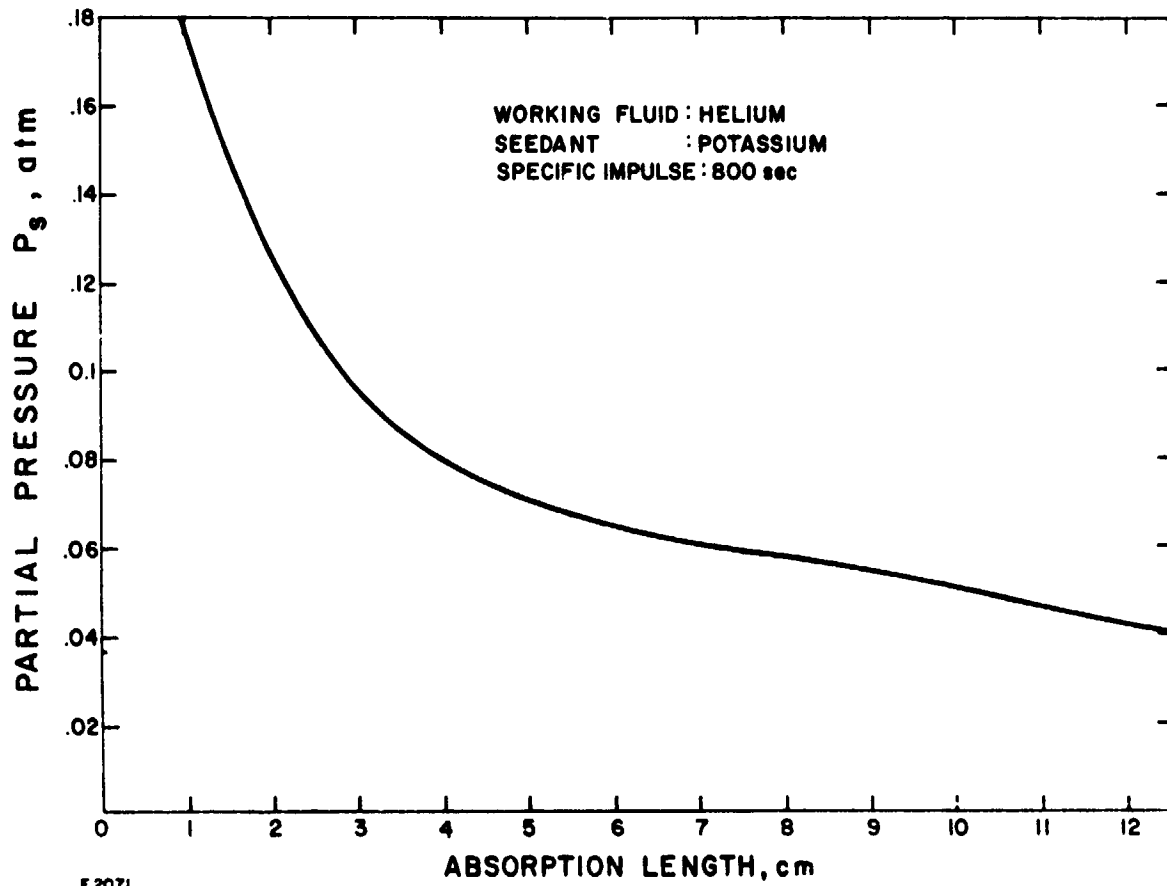
Fig. III-21   Seedant Partial Pressure

The average temperature defined by Eq. (III-70) should be used in this expression.

Since helium is monatomic (no dissociation losses), the wall thermal loss is now (cf. Eq. (III-80)).

$$P_w = \frac{3\pi\lambda yc^2}{\bar{c}_p} (1 + a/L)(1 - 2h_w/c^2) \qquad \text{(III-92)}$$

Since all species present are monatomic, the average constant-pressure specific heat is

$$\bar{c}_p = \frac{1}{\gamma-1} RP_c / \left[4p_c + (M_s - 4(1+\beta))p_s\right] \qquad \text{(III-93)}$$

In this expression, the seedant partial pressure p_s is again to be calculated at the chamber temperature, but β is to be calaulated at $\bar{T}$.

The enthalpy/unit mass at the wall is given by (cf. Eq. (III-89)).

$$h_w = RT_w\left[\frac{5}{2}p_c + \left(\frac{T_i}{T_w}\right)\beta p_s\right] / \left[4p_c + (M_s - 4(1+\beta))p_s\right] \qquad \text{(III-94)}$$

where p_s is fixed but β is to be calculated at the wall temperature.

Equation (III-92) is plotted as a function of the absorption length, y as Curve II of Fig. III-16 for p_c = 30 atm, I_{sp} = 800 sec, and T_w = 1100°K. Except for very small engines, the wall losses are higher for helium than for hydrogen: the higher chamber temperature required with helium for a given specific impulse results in a higher thermal conductivity of the working fluid. The efficiency, however, is now given simply by

$$\eta = 1 - P_w/P_o \qquad \text{(III-95)}$$

which, for an input power of 15 kW, is shown as Curve III of Fig. III-17. Comparison with Curve I, for a hydrogen engine with the same power input, shows that the efficiency is considerably higher at small absorption lengths. The reason for this is that the losses in small hydrogen engines are dominated by the effects of dissociation.

It is clear that, to minimize losses, a helium engine should be physically as small as possiole. Table III-3 gives the design parameters for an engine with an absorption length of 2 cm, which is as small as seems at all feasible. Comparison with the hydrogen engine shows that helium offers better performance, because smaller chamber lengths may be

TABLE III-2

PARAMETERS OF THE HELIUM ENGINE

Input Power	15 kW
Specific Impulse	800 sec
Mass Flow Rate	0.36 gm/sec
Chamber Pressure	30 atm
Chamber Temperature	$6000^{\circ}K$
Wall Thermal Losses	3.8 kW
Power Efficiency	74%
Thrust	2.8 N = 0.64 lbw
Absorption Length	2 cm
Chamber Length	3 cm
Throat Area (C_F = 1.7)	0.55 mm^2
Throat Diameter	0.84 mm
$L* = V_c/A_t$	8.7 cm
Wall Thermal Flux	460 watts/cm^2
Maximum Wall Thickness (Copper)	6.7 cm
Seedant Partial Pressure	0.15 atm

employed. It should be noted, however, that the characteristics length L*
for the helium engine is only 8.9 cm, which is very short compared to
conventional rocket practice. The requirement for an adequate L* in a
chemical rocket is based on combustion dynamics, so that it is possible
that it can be relaxed in the laser-powered engine. If it must be increased,
the performance of the helium engine rapidly decreases.

Also shown in Fig. III-17 (Curve IV) is the efficiency of a helium
engine with an input power of 50 kW, demonstrating again the rapid increase
in efficiency as the power level is increased.

In comparing the two propellants, it should be remembered that the
present analysis neglects convective heat transfer. The thermal flux due
to convection may be written

$$J = \rho(h_c - h_w)v_c \qquad \text{(III-96)}$$

where

$$\rho = P_c \frac{M}{RT} \qquad \text{(III-97)}$$

is the gas density and v_c is the convective velocity. For the same exhaust
velocity, the chamber enthalpy/unit mass is higher in the hydrogen engine
than in the helium engine, in the ratio $(1 + 2h_e/c^2):1$. If the convective
velocities are comparable in the two cases, as determined by mixing pro-
cesses, the convective heat transfer may be roughly compared as

$$J_{H_2}/J_{He} \simeq (\frac{2}{3950})(\frac{6000}{4})(1 + 2h_e/c^2) \simeq 1.4 \qquad \text{(III-98)}$$

so that the convective losses are expected to be slightly higher in the hydro-
gen engine.

Radiative losses, on the other hand, are expected to be higher in
the helium engine, because of the higher temperature of the chamber gases.
If as a first approximation, one assumes a blackbody (T^4) law for the radia-
tion losses, they should be about 5 times higher. The magnitude of these
losses has not yet been determined, however, and it is likely that they are
insignificant.

The overall conclusion is that helium is probably the best propell-
ant, if a sufficiently small test engine can be constructed. This is expected
to remain true for engines up to an input power of perhaps 100 kW, but it
is clear that hydrogen becomes the propellant of choice in sufficiently large
engines (and certainly in those of operationally useful size). In any case,
it is clear that the efficiency increases so rapidly as the power level and
size of the engine is increased that maximizing the efficiency of the test
engine is not worth major effort.

IV. EXPERIMENTAL HARDWARE

1. OVERVIEW OF EXPERIMENTAL SETUP

A photograph of the Laser Propulsion experimental hardware, installed at Workstation No. 1 of the HPL-10 Laser, is presented in Fig. IV-1. The laser propulsion experiments were performed inside a stainless steel, vacuum tight dump tank which was mounted on top of a portable stand. The tank was originally employed as a dump tank for a shocktube facility at AERL, and it was extensively modified under the laser propulsion contract.

A sketch of the dump tank/support stand assembly is shown in Fig. IV-2 and indicates the modifications which were required for the laser propulsion program. First, one head of the tank was cut off and reattached by means of a large flange as shown in Fig. IV-2. Secondly, six (6) flanged access ports were fabricated and installed on the tank. The purpose of each access port is shown in Fig. IV-2. Quartz windows (3/4-inch thick) were installed in special holders and mounted on the horizontal pair of access port flanges. The windows provided a view of the thrust chamber nozzle exit, so that breakdown could be monitored visually and photographically recorded. The side access port (rotated approximately 45° below the horizontal) shown in Fig. IV-1 was used as the mounting flange for the cesium seeder. The opposite flange on the other side of the tank (see Fig. IV-5) housed a nonporous protective glove. The glove provided safe, mechanical access to the experimental hardware and protected the user from contamination by residual cesium. The glove was primarily intended to be used to change thrust chamber nozzles. A number of nozzles were placed inside the tank prior to the test period. A special wrench was designed that could be used easily with one hand. The nozzles were then changed using the protective glove and wrench while viewing the thrust chamber through the observation port. Using this technique, the laboratory test area was never subjected to possible cesium contamination during a test period.

2. DIAMOND WINDOW HOLDER

The assembly drawing for the diamond window and fuel manifold is presented in Fig. IV-3. In addition, a photograph of the diamond window holder is shown in Fig. IV-4 installed on the propulsion tube and dump tank. The photograph shows the right side of the experimental setup with the HPL-10 welding laser. The laser and F 21 telescope mounted on its air table are shown to the right, and are enclosed by a lucite cage which provides containment of stray IR radiation. The ignition test-rig is located inside the dump tank at the front end, with the window isolation tube and diamond window assembly protruding towards the laser.
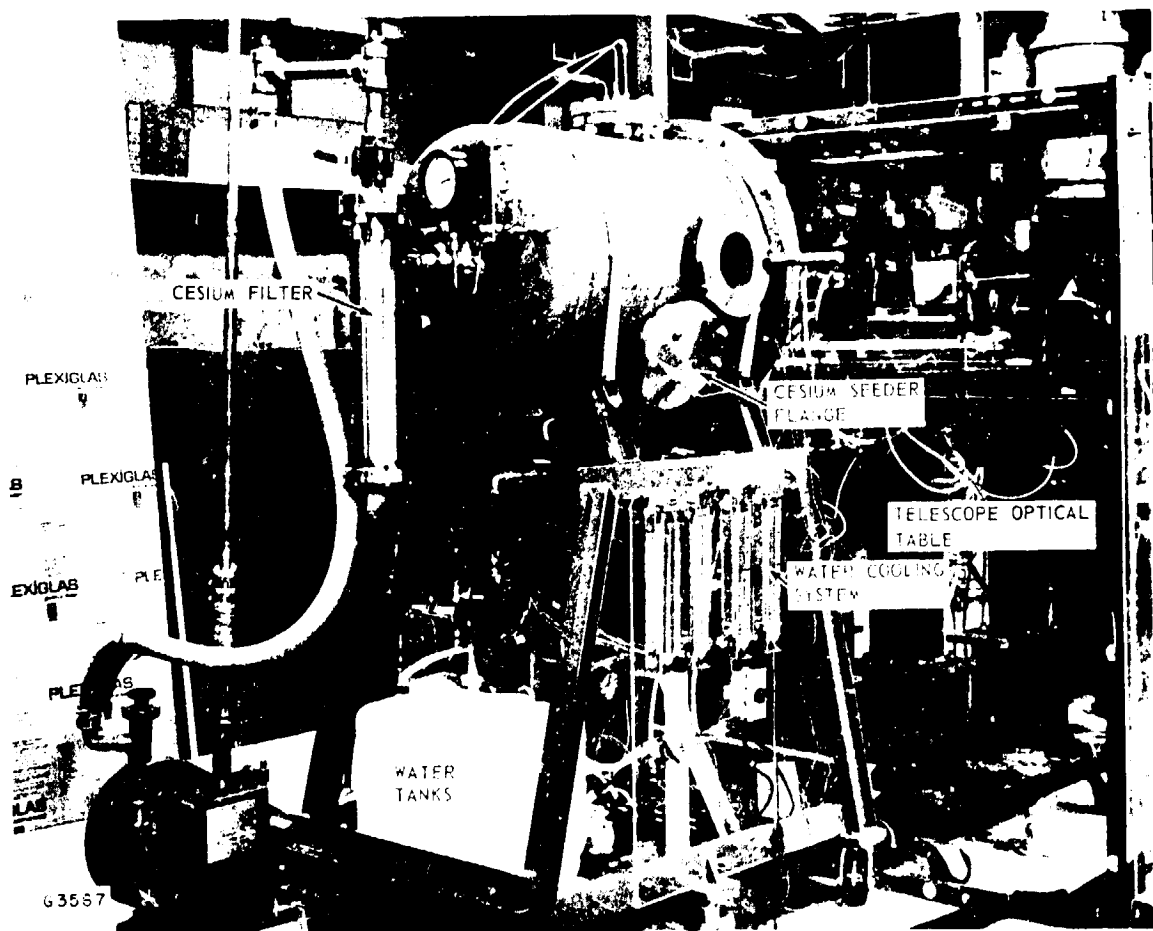
Fig. IV-1   Photograph of the Laser Propulsion Experimental Hardware
             installed at Work Station No. 1
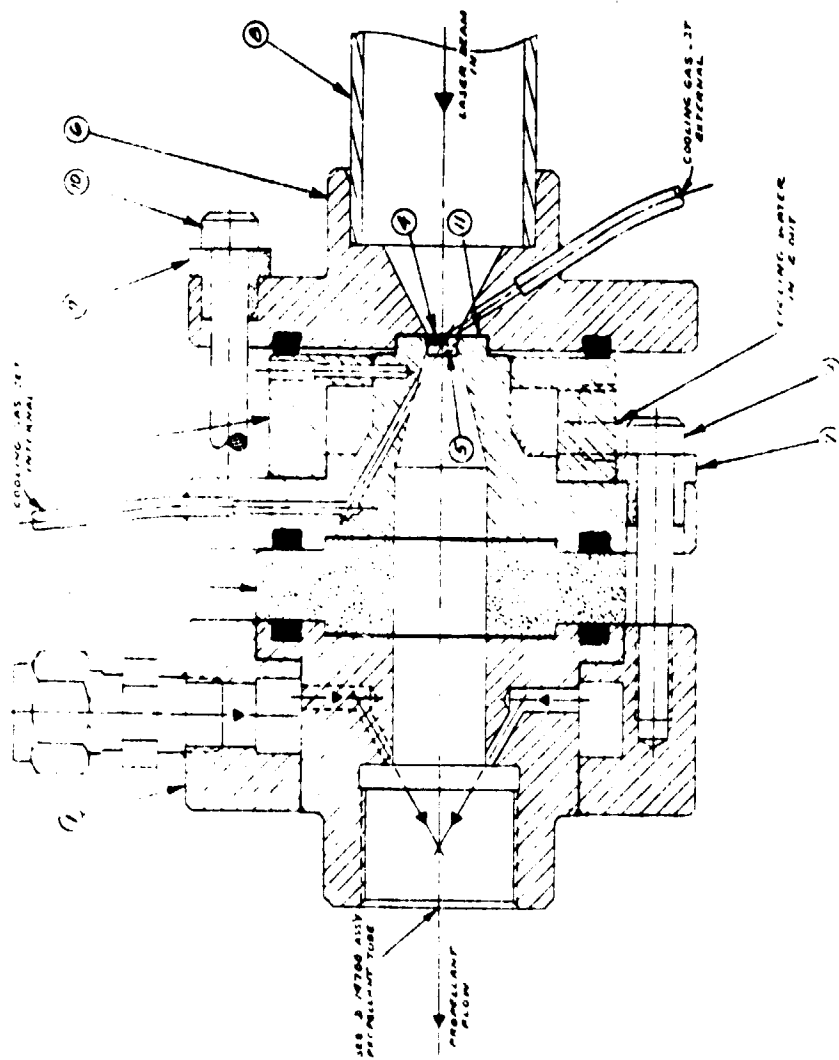
Fig. IV-2   Outline and Dump Tank Assembly Laser Propulsion

Fig. IV-3   Assembly of Diamond Window and Fuel Manifold for Laser Propulsion Test
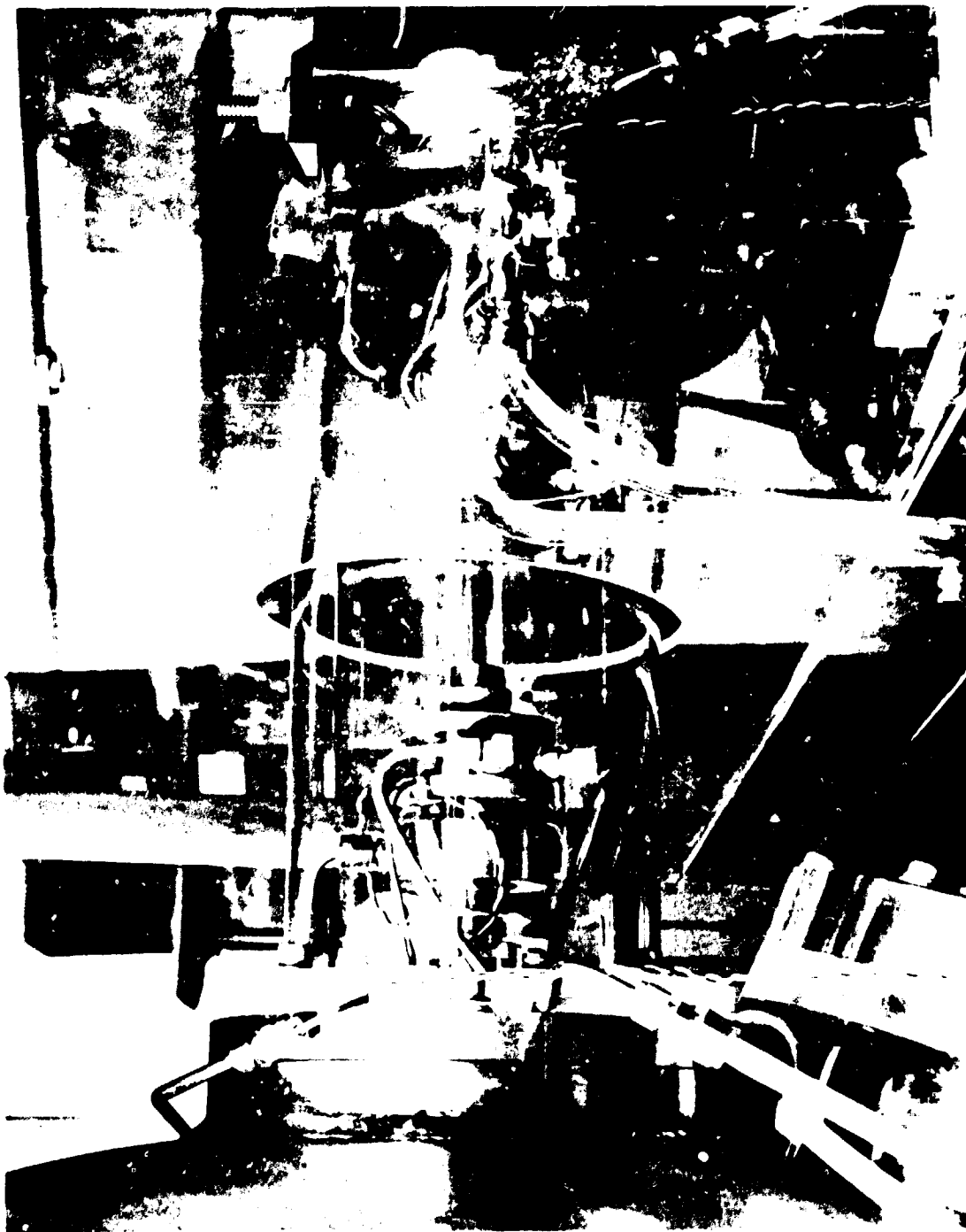
G 3565

Fig. IV -4   Photograph of the Diamond Window Assembly

Fig. IV-5   Nozzle Insert

The diamond window and fuel manifold assembly consists of the following parts:

Part Nomenclature	Item No. (Ref. Fig. IV-3)
Retainer	6
Window Holder Assy	3
Insulator	2
Fuel Manifold Assy	1
Dust Shield	8

The window holder assembly was fabricated from OFHC copper. The diamond for the window was cut into the shape of a cone frustum as shown. The diamond was wrapped in a 5 mil layer of gold foil and pressed in place by the retainer. The retainer was fabricated from molybdenum and was electrically insulated from the window holder assembly, as shown in Fig. IV-3. In this manner a gold/molybdenum thermocouple was formed to measure the temperature of the diamond window directly. The gold foil also acted as a pressure gasket.

The sides of the diamond were in contact with the window holder assembly through the gold foil. The window holder assembly was designed with an internal annular ring through which cooling water flowed. In addition two (2) cooling gas jets were directed onto the diamond surface from both sides, as shown. The diamond window holder assembly was bolted to the fuel manifold assembly as shown in Fig. IV-3. An insulator was sandwiched between the two assemblies to act as a heat break in order to minimize the heat load flowing into the diamond window assembly. The diamond window/fuel manifold assembly was threaded onto the propulsion tube as shown in the photograph presented in Fig. IV-4.

3. THRUST CHAMBER

The propulsion tube was attached to the thrust chamber and the whole assembly was supported by the internal dump tank cover flange, as shown in Fig. IV-2. Two thrust chambers were fabricated and used in the laser propulsion experiment. The first thrust chamber, called the ignition test rig, had 1-in. diameter x 5/8-in. thick quartz windows located one on each side of the chamber. The purpose of these windows was to provide a means of viewing breakdown during the preliminary testing phase. The second thrust chamber was built without windows and had a better designed cesium mixing manifold.

Both thrust chambers were fabricated from OHFC copper and consisted of thick-walled copper cylinders. A threaded hole in the end of each

thrust chamber was used to mount the nozzle and focusing mirror assembly. A 40:1 expansion ratio supersonic nozzle was designed with a 3-mm throat diameter, and a special contoured cutter was made in order to fabricate these nozzle in quantity at a reasonable cost. Small copper inserts were used to reduce the throat diameter to that required for tests, depending on the power level, intended chamber pressure and exhaust velocity. In addition, several 30-degree half angle diverging sonic nozzles were fabricated for the preliminary hardware checkout phase conducted with the ignition test rig. A drawing of this nozzle is presented in Fig. IV-5 and shows the general arrangement of both nozzle designs. The nozzles were fabricated from OFHC copper and the inside face contained a highly polished 2.0-in. spherical mirror. When the nozzles are installed in the thrust chambers, the mirrors provide a feedback of the incident radiation from the HPL-10 device transmitted through the F 21 telescope. The spot size of the radiation filled the mirror and back focused the beam into the center of the thrust chamber.

4. COOLING SYSTEMS

The laser propulsion experiment required water cooling for the diamond window holder and the F 21 telescope mirrors. In addition, these systems require the inlet temperature of the water to be at room temperature to prevent sweating of the copper parts. Since the HPL-10 facility did not have sufficient cooling water capacity to completely support the laser propulsion experiment, a portable system was designed and fabricated. This system was built into the dump tank stand as shown in the photograph presented in Fig. IV-1.

The water cooling system consisted of a 20-gallon supply of room temperature distilled water which was stored in two 10-gallon plastic jugs as shown. The water was pumped from the supply tanks to a switching manifold, up through a series of flowmeters to three (3) independent cooling lines. These lines were connected to the systems to be cooled and the return heated water was passed through a heat exchanger on its way back to the supply tanks. The heat exchanger consisted of a small automobile radiator core and a variable speed fan. The fan was mounted on the backside of the radiator and pumped room air through the core. The switching manifold was configured in such a way as to allow the cooling water to circulate in a loop without passing through any elements. When one of the three cooling systems was activated, the return loop path was throttled by means of a control valve. The system was designed to provide a cooling capacity of approximately 1.5 gal/min for each of the three independent systems.

5. FLOW SYSTEMS

The photograph presented in Fig. IV-6 shows the left side of the experimental setup with the HPL-10 welding laser. The gauges and vernier controls shown at the bottom of the photograph are part of the control panel for the various flow systems. The flow systems were designed so that high pressure lines (2000 psi) could be connected directly to the control panel as shown. The high pressure gas was then stepped down to 600 psi by means of the three regulators and the operating pressures were displayed on the three pressure gauges. Each system had an electrically operated solenoid
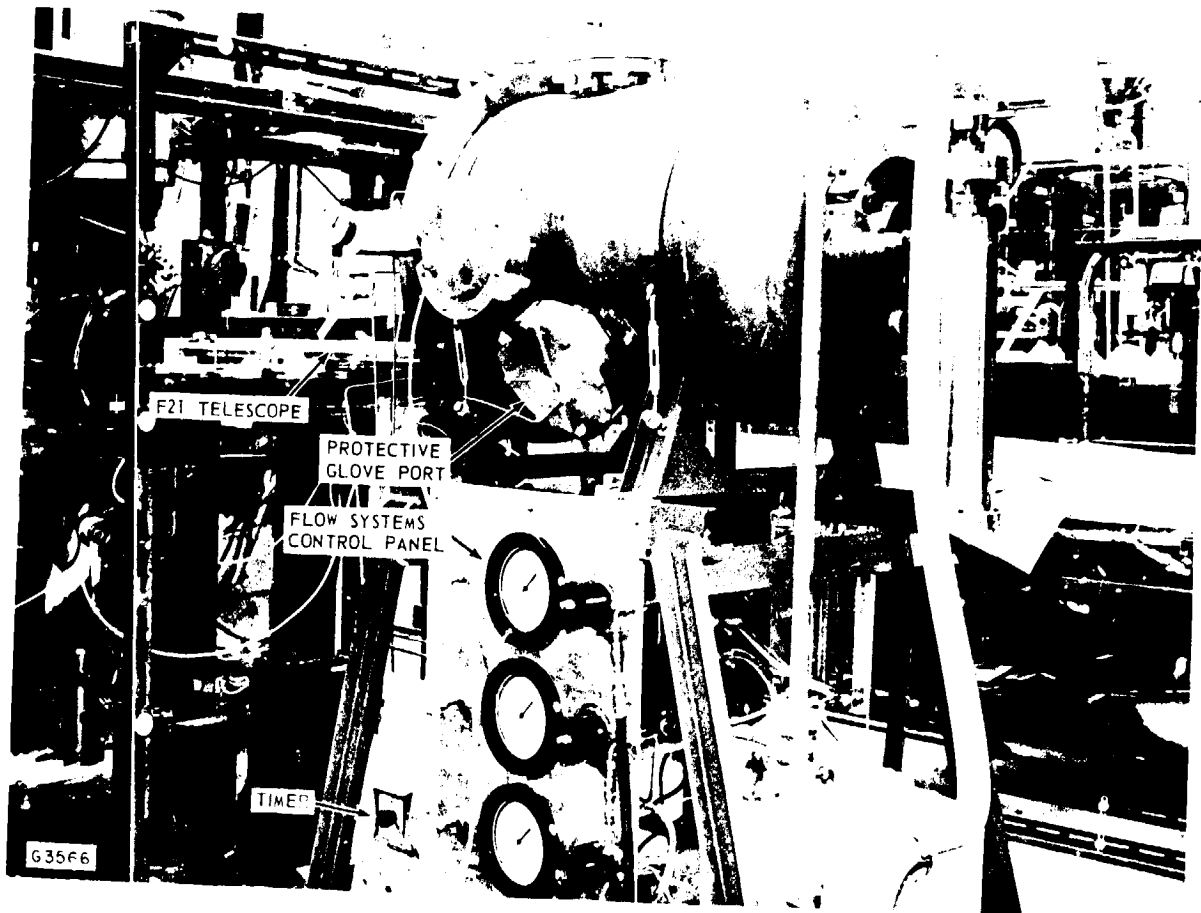
Fig. IV-6   Photograph of the Laser Propulsion Experimental Hardware
Showing the Flow Systems Control Panel

valve and a vernier controlled needle valve which was set to the desired flow rate. The system was designed so that the control orifices were always choked independent of the operating pressure in the thrust chamber. The three flow systems supplied propellant feeds to the inside of the diamond window, to the main fuel manifold and to the cesium seedant manifold. In addition, a low pressure system provided helium for jet cooling on the outside of the diamond window.

The electrical solenoids for all flow systems were interconnected. The main power cord was connected to the solenoids through a timer and a manual switch. In operation, all flow systems were preset to the desired pressures and flow rates. The timer was preset to the desired total run time of up to ten (10) seconds. The manual switch was then closed to activate all flow systems simultaneously, and the timer automatically terminated the run by closing all the solenoids.

6. SEEDANT INJECTOR

The seedant injector used in this program was an adaptation of a device which has been used successfully at AERL, Inc., to inject cesium seed in shock tube experiments. The principle of operation is that chilled gas flowing across a bath of molten cesium will produce an aerosol of fine cesium particles, which can then be transported with the gas flow to the thrust chamber. To avoid contact between the cesium and the atmosphere, it is loaded in a sealed glass ampoule into a closed chamber, where it is broken by a piston driven by compressed nitrogen. The cesium then flows down into an elbow made from stainless steel pipe, which is wrapped in electrical heating tape to allow control of the cesium bath temperature. The seedant manifold propellant gas flow, from the flow system described in the previous section, passes through a copper coil immersed in a dewar of liquid nitrogen and then over the cesium bath. The concentration of cesium aerosol particles produced can be varied by changing the bath temperature.

This system is also adaptable to use with sodium or potassium as seedants.

This seedant injector worked well in the experiments to be described here, but it should be noted that calibration difficulties exist if it is desired to control quantitatively the seedant concentration in the thrust chamber. In particular, it is possible for the aerosol particles to accumulate in bends and crevices in the piping between the cesium bath and the thrust chamber. Some of the particles may also melt and adhere to the injector manifold walls. For quantitative work, it would probably be necessary to monitor the seedant concentration in the exhaust of the thrust chamber, for example by spectroscopic means.

7. FURTHER DETAILS

The above brief description of the experimental hardware is intended to provide sufficient information for understanding the experiments

described in the next chapter. A more detailed description will be provided with the hardware when it is delivered to NASA Lewis Research Center, together with an operations manual which is in preparation.

Provisions were made for diagnostic instrumentation (especially thrust and exhaust velocity measurement) but were not fully implemented because the experiments described here were concerned with establishing reliable inverse Bremsstrahlung absorption in the thrust chamber and achieving substantial chamber pressure increases when the laser was initiated. The diagnostic instrumentation would not be useful until these goals had been realized.

V. EXPERIMENTS

1. INITIAL TESTS

The first tests were intended as a shakedown of the system components and especially as a checkout of the optical alignment procedures. To allow adjustments to the system, it was desired to operate initially with the access ports to the dump tank open, and this meant that neither hydrogen gas nor alkali metal seedants could be employed. The seedant injector system was therefore not installed for these tests, being replaced by a piece of straight pipe. During runs the access ports were covered by lucite sheet, in order to prevent the escape of stray infrared radiation.

Because of the cost of occupying the work station of the HPL-10 welding laser ($125 per hour) the equipment had been designed, as described in the previous chapter, to allow as rapid installation at the laser as possible. The test cell and diamond window assembly, the dump tank, cooling water supply, and gas metering equipment were assembled on a single cart which could be rolled up to work station No. 1 of the welding laser. Figures IV-1 and IV-5 are photographs of the system at the work station. The telescope for focusing the laser beam inside the diamond window was mounted on a separate wheeled table at the work station, and the lucite enclosure around the work station was extended with additional lucite sheeting so as to surround this table. The diamond window assembly was enclosed in a lucite tube, as shown in Fig. IV-4, which penetrated the lucite shield.

Assembly of the equipment at the laser for the first time, including installation of ancillary gear such as the vacuum pump, gas supplies, etc., took about 6 hours. Much of this time was spent in optical alignment. This task would have been difficult, if not impossible, without the He-Ne laser which is boresighted with the HPL-10 welding laser; in practice, however, it proved necessary to check the boresighting before each alignment by taking a burn pattern on a lucite sheet in front of the diamond window and observing whether the spot from the He-Ne laser fell into the center of the pattern. The procedures involved in setting up the equipment are discussed in more detail in Ref. 21. With experience it became possible to install the complete system at the laser within about 3 hours.

The initial tests which were carried out are summarized in Table V-1. The first two tests were intended merely to verify that laser radiation was passing through the diamond window and entering the thrust chamber. For this purpose the nozzle was removed from the thrust chamber and replaced by a piece of lucite sheet. Apart from the helium flow over the outside of the diamond window the only gas flow in the system for these tests consisted of nitrogen at maximum flow rate through the window

TABLE V-1
INITIAL TESTING

Run Number	Laser Power, kW	Duration Seconds	Gas & Flow Rate Seedant Manifold	Gas & Flow Rate Window Manifold	Gas & Flow Rate Main Manifold	Remarks
1	1	1/2	None	N_2 max flow	None	Nozzle removed and replaced by lucite sheet. Burn pattern asymmetric - probably reflecting from walls. Realigned optics.
2	1	1/2	None	N_2 max flow	None	As above - burn pattern now fairly symmetric.
3	2	1	N_2 max flow	N_2 max flow	N_2 max flow	Nozzle installed. Cold chamber pressure 10 psi. No flash observed, no pressure rise.
4	5	1	Same	Same	Same	Same
5	10	1	Same	Same	Same	No pressure rise. Sparks from nozzle. No detectable damage on inspection of nozzle, chamber and diamond window.
6	2	1/2	Argon, max flow	N_2 max flow	N_2 max flow	No flash or sparks observed, no pressure rise.
7	5	1/2	Same	Same	Same	Same
8	10	1/2	Same	Same	Same	Same
9	5	1/2	Argon, max flow	N_2, 20 gm/sec	None	No flash or sparks observed, no pressure rise.
10	10	1/2	Same	Same	None	Same
11	5	1/2	Argon, max flow	N_2, 10 gm/sec	None	No flash or sparks observed
12	10	1/2	Same	Same	None	Sparks from nozzle.
13	10	1	Same	Same	None	No flash or sparks observed
14	5	1/2	Argon, max flow	He, 28 gm/sec	None	No flash or sparks observed
15	10	1/2	Same	Same	None	Same
16	5	1/2	Argon, max flow	He, 11 gm/sec	None	Same
17	10	1/2	Same	Same	None	Same
18	5	1/2	Argon, max flow	He, 6 gm/sec	None	Same
19	10	1/2	Same	Same	None	Same
20	2	1	Argon, max flow	He, 22 gm/sec	None	Lucite tube burn test - see text.

manifold, to assist in cooling the window. The laser power employed was 1 kW for 0.5 second and, with adjustment, a reasonable burn pattern was obtained even at this low laser power, demonstrating that operation of the window was satisfactory.

With the nozzle and focusing mirror reinstalled, a series of tests was now run to determine whether breakdown in the chamber could be obtained in unseeded gas. While gaining confidence in the use of the diamond window, the gas flows were generally maintained at a high rate, especially through the window manifold. In the first of these tests nitrogen was used in all three manifolds, but thereafter argon gas was introduced through the seedant manifold, because it is known that laser-induced breakdown occurs more readily in this gas than in nitrogen. Eventually the gas flow through the main manifold was turned off and nitrogen or helium flowed through the window manifold. No breakdown was observed in the focal region through the sight tube in any of these tests, although in some of them, generally at high laser power, sparks were observed leaving the nozzle exit. The highest laser power employed was 10 kW for one second.

Because of these negative results, a simple test rig was used to determine whether a high flux density was being obtained in the focal region. A thin lucite tube was glued to the inner side of the nozzle, so that it was along the chamber axis when the nozzle was installed but did not block the focussing mirror. This device permitted gas flow through the test chamber but provided a highly absorbing target at the focus. At a power level of 2 kW for one second, with argon and helium flowing through the test cell, a bright yellow flame was observed through the sight tube. On inspection the lucite tube proved to have been burned quite symmetrically, giving confidence in the operation of the system.

Since all systems appeared to be working well this test series was terminated to allow installation of the seedant injection apparatus.

2. SECOND TEST SEQUENCE

With the seeder installed the system was assembled once again at work station No. 1 of the HPL-10 welding laser. A cesium ampoule was loaded into the seeder and broken with the air hammer. The seeder temperature was adjusted to $500^\circ C$.

The experiments carried out in this sequence are summarized in Table V-2. The first test was a check of operation of the seeder. With maximum helium flowing through the seeder and minimal flow through the window and main manifolds (to prevent seedant penetrating up the window isolation tube) an aerosol cloud was observed emerging from the nozzle. It thus appeared that the seeder was working as predicted.

The first run with the laser in this sequence (run No. 22) was at a power level of 10 kW for 0.5 second. No results were observed but it was then discovered that there was a serious misalignment between the

TABLE V-2

SECOND TEST SEQUENCE

Run Number	Laser Power, kW	Duration Seconds	Gas & Flow Rate Seedant Manifold	Gas & Flow Rate Window Manifold	Gas & Flow Rate Main Manifold	Seedant & Seedant Temp	Remarks
21	Off	-	He, max flow	He, 18.5 gm/sec	He, 18.5 gm/sec	C_g, 500°C	Aerosol cloud emerged from nozzle.
22	10	1/2	He, 7.4 gm/sec	He, 3.7 gm/sec	He, 3.7 gm/sec	C_g, 500°C	No breakdown observed - see text.
23	10	1/2	Same	Same	Same	"	Bright flash observed in chamber. Sparks from nozzle.
24	10	1/2	Same	Same	Same	"	Results reproducible. Diamond window becoming discolored.
25	10	1/2	Same	Same	Same	"	Same
26	10	1	He, 3.7 gm/sec	He, 1.9 gm/sec	He, 1.9 gm/sec	"	Bright flash in chamber, luminous jet with sparks.
27	10	1	He, 1.9 gm/sec	He, 0.9 gm/sec	He, 0.9 gm/sec	"	Same
28	10	1	He, 0.9 gm/sec	He, 0.5 gm/sec	He, 0.5 gm/sec	"	Jet appeared brighter
29	10	1	He, 0.5 gm/sec	He, 0.2 gm/sec	He, 0.2 gm/sec	"	Same
30	10	1	None	Ne, 0.2 gm/sec	He, 0.2 gm/sec	None	Run with seeder closed to check for residual C_g. Breakdown observed.
31	10	1	None	He, 0.2 gm/sec	He, 0.2 gm/sec	None	Same
32	10	1	H_2, 1.3 gm/sec	H_2, 0.7 gm/sec	H_2, 0.7 gm/sec	C_g, 500°C	Test with hydrogen: bright flash with luminous jet and sparks.
33	10	1	H_2, 0.7 gm/sec	H_2, 0.3 gm/sec	H_2, 0.3 gm/sec	C_g, 500°C	Same. Diamond window burned out.

CO_2 laser beam and the boresighted He-Ne laser. Alignment had been carried out using the He-Ne beam and it was found that the CO_2 beam was missing the diamond window and burning the molybdenum housing. The boresighting of the two lasers was adjusted and the optical system realigned.

At the same laser power and duration (10 kW for 0.5 second) and with the same gas flow conditions a bright flash was now observed in the chamber and sparks were noted coming from the nozzle. Several runs with the same conditions produced the same results. Figure V-1 is a photograph taken through the viewing port of the dump tank during one of these runs. The sparks from the nozzle are presumed to be cesium particles which have not been fully vaporized. It thus appeared that breakdown became possible as soon as cesium seed was added to the gas mixture.

At this time it was noted that the diamond window was becoming discolored. The outside surface of the window was cleaned, but, because the system now contained cesium, cleaning the inside the surface of the window would have required removal of the system from the HPL-10 welding laser room and disassembly. The time at the laser station lost in these activities would have cost more than the diamond was worth, and so the decision was made to continue.

The next series of runs (26 thru 29) were all carried out at 10 kW laser power for one second, and were intended to investigate how far the gas flows could be reduced while maintaining breakdown. Successful operation was achieved at gas flow levels down to the minimum available from the metering system.

At this point the seeder manifold was closed and the test chamber was flushed several times with helium, through the main and window manifolds. Two successive runs with the seeder closed using laser powers of 10 kW for one second gave breakdown results similar to the previous ones. It therefore appeared that cesium had accumulated in the thrust chamber, but it was not expected that this would cause any significant problem.

Finally a series of tests using hydrogen instead of helium was started, in order to see whether this changed the breakdown conditions. Unfortunately, the diamond window broke on the second of these runs. This necessitated removal of the apparatus from the laser room and the test sequence was therefore terminated.

3. THIRD TEST SEQUENCE

Experiments carried out in the third test sequence are summarized in Table V-3. At the beginning of this sequence some difficulties were encountered in obtaining breakdown and a number of checks were carried out to determine whether the seeder was operating correctly and whether the optical alignment was satisfactory. Eventually, however (run 44), breakdown was achieved at a laser power level of 10 kW for 0.5 second with helium

Fig. V-1   Firing the Test Engine

TABLE V-3

THIRD TEST SEQUENCE

Run Number	Laser Power, kW	Duration Seconds	Gas & Flow Rate Seedant Manifold	Gas & Flow Rate Window Manifold	Gas & Flow Rate Main Manifold	Seedant & Seeder Temp	Remarks
34	Off	-	H_2, max flow	H_2, max flow	H_2, max flow	C_s, 450°C	Seeder check: no aerosol cloud observed leaving nozzle.
35	Off	-	Same	Same	Same	C_s, 500°C	Faint cloud leaving nozzle.
36	Off	-	Same	Same	Same	C_s, 550°C	Denser cloud leaving nozzle.
37	5	5	H_2, max flow	H_2, max flow	H_2, max flow	C_s, 500°C	No flash or exhaust noted. Re-aligned laser to diamond window. Lucite burn pattern outside window somewhat asymmetric. aligned He-Ne laser with peak intensity.
38	10	1	H_2, max flow	H_2, max flow	H_2, max flow	C_s, 500°C	Nothing observed. Removed nozzle, found focusing mirror dirty.
39	2	1/2	Off	H_2, max flow	H_2, max flow	None	Lucite burn at nozzle exit. Good pattern, alignment good. Installed clean nozzle.
40	Off	-	He, 18.5 gm/sec	None	None	C_s, 500°C	Felt exhaust with gloved finger; strong flow through seeder.
41	10	1	He, 1.9 gm/sec	He, 0.9 gm/sec	He, 0.9 gm/sec	C_s, 500°C	Nothing observed.
42	1	1/2	Off	He, max flow	Off	None	Plastic tube inserted through nozzle to check focus. Burned off tube, but appeared asymmetric. Realigned optics.
43	1	0.3	Off	He, max flow	Off	None	Same, but more symmetric burn.
44	10	0.5	He, 1.9 gm/sec	He, 0.9 gm/sec	He, 0.9 gm/sec	C_s, 500°C	Bright flash in chamber.
45	10	0.5	Same	Same	Same	Same	Check for reproducibility - same result.
46	10	0.5	He, 1.9 gm/sec	He, 3.7 gm/sec	He, 3.7 gm/sec	C_s, 500°C	Bright breakdown flash observed.
47	5	1	He, 1.9 gm/sec	He, 3.7 gm/sec	He, 3.7 gm/sec	C_s, 500°C	No breakdown.
48	10	1	He, 1.9 gm/sec	He, 3.7 gm/sec	He, 3.7 gm/sec	C_s, 500°C	Good breakdown.
49	7	1	Same	Same	Same	Same	No breakdown.
50	10	1	Same	Same	Same	Same	Good breakdown.
51	7	1	Same	Same	Same	Same	No breakdown.
52	10	1	He, 1.9 gm/sec	He, 3.7 gm/sec	He, 3.7 gm/sec	C_s, 500°C	Dump tank at 1 atm. No breakdown observed
53	10	1	Same	Same	Same	C_s, 500°C	Dump tank 100 torr. Good breakdown.
54	10	3	Same	Same	Same	C_s, 500°C	Bright breakdown, streaks in exhaust.
55	10	3	Same	Same	Same	C_s, 500°C	Same
56	10	3	Same	Same	Same	C_s, 500°C	Same
57	10	3	He, 18.5 gm/sec	He, 15 gm/sec	He, 18.5 gm/sec	C_s, 500°C	1/16" nozzle installed. No breakdown.
58	10	3	He, 18.5 gm/sec	He, 15 gm/sec	He, 22 gm/sec	C_s, 500°C	No breakdown.
59	10	3	He, 18.5 gm/sec	He, 15 gm/sec	He, 26 gm/sec	C_s, 500°C	No breakdown. Diamond becoming discolored.
60	10	2	He, 1.9 gm/sec	He, 3.7 gm/sec	He, 3.7 gm/sec	C_s, 500°C	1/32" nozzle installed. No breakdown.
61	13	2	He, 1.9 gm/sec	He, 3.7 gm/sec	He, 3.7 gm/sec	C_s, 500°C	Nozzle installed. Breakdown, but diamond popped.
62	10	2	He, 1.9 gm/sec	He, 3.7 gm/sec	He, 3.7 gm/sec	C_s, 500°C	New diamond and 1/32 nozzle installed. No breakdown.
63	12	2	Same	Same	Same	C_s, 500°C	Sparks in chamber, but no breakdown flash.
64	15	2	Same	Same	Same	C_s, 500°C	Same
65	15	2	Same	Same	Same	C_s, 500°C	Bright flash, strong pressure rise, but diamond popped.

flowing through all manifolds. Note that apart from the duration from the run, the conditions in run 44 were the same as those in run 27 in the second test sequence when breakdown was also achieved.

The next question addressed was that of the minimum power required for breakdown. Several runs were undertaken at lower power levels, alternating with runs at 10 kW to check that conditions did not change. It was found that breakdown could not be achieved at power levels as high as 7 kW, and it appeared that the threshold was in fact close to 10 kW. This was confirmed by the finding that relatively small changes in the conditions (for example, changes in the pressure in the dump tank) could prevent breakdown at 10 kW. It does seem probable that satisfactory operation of the test cell at elevated temperatures and pressures would require the maximum power of which the HPL-10 laser is capable (approximately 20 kW).

One possible explanation of this result was that less power than predicted was actually reaching the thrust chamber, due to reflections at the diamond window, etc. For this reason it was decided to install a nozzle of small throat diameter, in order to allow pressure rises to occur at low mass flow and low power levels. A nozzle insert restricting the throat to 1.5 mm diameter therefore was installed. Unfortunately it appeared that this change was sufficient to prevent breakdown at 10 kW. After several runs with this nozzle it was noted that the diamond was again becoming discolored. In order to make as rapid progress as possible before losing the diamond, a nozzle insert with an even smaller diameter (0.8 mm) was installed and, when no breakdown was observed at 10 kW, the laser power level was turned up to 12 kW. At this power level breakdown occurred but the diamond window broke. It seems probable that the diamond window could have transmitted 12 kW had it not been that it was already becoming discolored.

Only one more diamond window was available. When it was installed with the 0.8 mm nozzle, no breakdown was observed at 10 kW. At 12 kW laser power, sparks were observed in the chamber but there was no breakdown flash. The laser power was therefore increased to 15 kW which produced a bright flash in the chamber and a strong pressure rise but once again the diamond window broke.

Since no more windows were available, the experimental program was terminated at this point.

4. EXPERIMENTAL RESULTS

The first two diamond windows used in these tests each lasted for thirty runs or more at power levels up to 10 kW. Their eventual failure was apparently due to gradual discoloration and consequent absorption of laser radiation. Examination of the second diamond with a lens before it failed seemed to indicate that some of the discoloration was internal to the stone; if it is true that diamonds undergo an internal degradation of transparency with exposure to intense 10.6μ radiation, a fundamental limit

to the endurance of diamond windows would clearly be indicated. The long-term response of diamonds to CO_2 laser radiation is the subject of a separate study which will be reported elsewhere.[22]

In any case cleanliness of the window is essential to its durability in this application. The experimental apparatus was deficient in this respect, in t' at it was impossible to clean the inner surface of the diamond window without major disass(.bly. In future experiments of this type, the window isolation tube should incorporate a shut off valve so that the window assembly may be isolated from the rest of the system and can readily be removed for cleaning.

A second major problem which was discovered with this apparatus was that a laser power of 10 kW was only marginally sufficient to cause breakdown in the test chamber, but higher laser powers caur 'd rapid window degradation. For example, the third diamond window, e· en though clean, failed quickly at 15 kW. This margin is rather too narrow for satisfactory, flexible operation of the system. If the original design of the test chamber (Fig. V-4) had been used, instead of the single mirror design (Fig. V-5), with its focusing mirror of shorter focal length, it is probable that breakdown would not have been achieved at laser power levels which could be sustained by the diamond window. In this connection it should be noted that in other experiments[22], CO_2 laser powers in excess of 20 kW for up to 20 seconds have been transmitted through diamond windows. In these experiments, however, the diamond was fresh and clean and the window holder was of an improved design in which cooling water made contact with the diamond itself. Better cooling can increase performance in these windows, but this design feature is probably not as important as those which permit maintenance of high cleanliness.

5. CONCLUSIONS

Although the experimental program was terminated prematurely because of diamond window failures, significant progress was achieved towards the goal of demonstrating a laser-powered thruster. The device for injecting alkali metal seedant into the thrust chamber has been demonstrated, and breakdown and inverse bremsstrahlung absorption has been achieved. Apart from window problems, no reason has been found to doubt the feasibility of the design approach.

Power levels in the 10 kW range are quite low by rocket thruster standards. For future experiments with thrusters using diamond windows, it is suggested that more work is needed to optimize the window design for maximum power transmission. This should include checkout of any proposed window assembly at the highest power available from the laser to be used, under steady state conditions, before proceeding to tests of the thruster itself. It is essential to have confidence in the durability of the window, in order to be able to concentrate on the laser absorption and gas dynamic phenomena which will determine the feasibility of this type of engine.

The modular test apparatus built under this program has proven convenient and flexible in operation. It can provide the basis for a continued program of laser-powered thruster development at relatively low cost. The system is adaptable to other types of window (e.g., zinc selenide, aerodynamic etc.) and to the use of other absorption mechanisms (molecular, dust, etc.).

REFERENCES

1. Kantrowitz, A. R. , "Propulsion to Orbit by Ground-Based Lasers" Astronautics and Aeronautics Vol 10, #5, May 1972, pp. 74-76.

2. Rom, F. E. and Putre, H. A. , "Laser Propulsion", NASA TM-X-2510, April 1972.

3. Pirri, A. N. and Weiss, R. F. , "Laser Propulsion", Paper # 72-719, AIAA 5th Fluid and Plasma Dynamics Conference, Boston, Mass., June 1972.

4. Bridges, W. B. , et. al, "Coherent Optical Adaptive Techniques (COAT)", Technical Report #1, Hughes Research Laboratories, July 1973.

5. Minovitch, M. A. "Performance Analysis of a Laser Propelled Inter-orbital Transfer Vehicle", NASA CR-134966 February 1976.

6. ARPA

7. Battin, R. H. "Astronautical Guidance", McGraw-Hill, N. Y. , 1964, p. 36.

8. Under IRAD Funding: to be reported elsewhere.

9. Douglas-Hamilton, D. H. and Hoag, E. , "Natural Diamond as a High-Power Laser Window", JOSA, January 1974.

10. Reilly, D. A. , Avco Everett Research Laboratory, Inc. , private communication.

11. Chapman, P. V. , Monsler, M. and Pirri, A. , "Laser-Powered Rocket Propulsion Study (U)", Final report, ARPA Contract # DAHC60-73-C-0098 (SECRET), May 1974, Avco Everett Research Laboratory, Inc.

12. Sedov, L. L. "Effects of High-Power Lasers", Academic Press, 1969.

13. Fay, J. A. "Molecular Thermodynamics", Addison Vesley, 1965, p. 234.

14. Bartz, D. R. in "Advances in Heat Transfer", Vol II. (Harnett, J. P. and Irvine, I. F. , Ed.) Academic Press. N. Y. 1968 p. 84.

15. Bartz, D. R. , loc cit, pp. 45 et seq.

16. Seifert, H.S. (Ed.) "Space Technology", Wiley, N.Y. 1959, p. 12-23.

17. Lees, L., in "Recent Advances in Heat and Mass Transfer", (Hartnett, J.P., Ed.), McGraw-Hill, N.Y. 1961, pp 161-207.

18. Fay, J.A., loc cit, ch. 20.

19. Chapman, S., and Cowling, T.G. "The Mathematical Theory of Non-Uniform Gases", Cambridge U.P., 1970, p. 256.

20. Rosner, D.E. "Convective Heat Transfer with Chemical Reaction", Aerochem Research Labs, ARL 99, Part 1, 1969.

21. Chapman, P.K. and Otis, J.H., "Operational Manual for Laser Absorption Test Facility", in preparation.

22. Zar, J.L., Avco Everett Research Laboratory, Inc., Private communication.

APPENDIX A

GRAVITY COMPONENTS IN RECTILINEAR BOOST

From Fig. (A-1), the geocentric radius at range ρ along a rectilinear trajectory of initial zenith angle γ_o is

$$r^2 = \rho^2 + r_o^2 + 2\rho r_o \cos \gamma_o \qquad (A-1)$$

For $\gamma_o \approx 60°$, this gives Eq. (II-24).

The zenith angle (angle between the trajectory and the local vertical) at range ρ is given by

$$\cos \gamma = \frac{\rho^2 + r^2 - r_o^2}{2r\rho}$$

$$= \frac{\rho + r_o \cos \gamma_o}{r} \qquad (A-2)$$

The acceleration due to gravity at ρ is

$$g = g_o \left(\frac{r_o}{r}\right)^2 \qquad (A-3)$$

and the component of gravity along the trajectory is

$$g_{\parallel} = g_o \cos \gamma$$

$$= g_o \frac{r_o^2 (\rho + r_o \cos \gamma_o)}{r^3}$$

$$= g_o \frac{r_o^2 (\rho + r_o \cos \gamma_o)}{\left[\rho^2 + r_o^2 + 2\rho r_o \cos \gamma_o\right]^{3/2}} \qquad (A-4)$$

This equation is plotted in Fig. II-1, for several values of γ_o. It is seen that $g_{\parallel}$ is almost constant out to ranges of several thousand kilometers if $\gamma_o \approx 60°$.
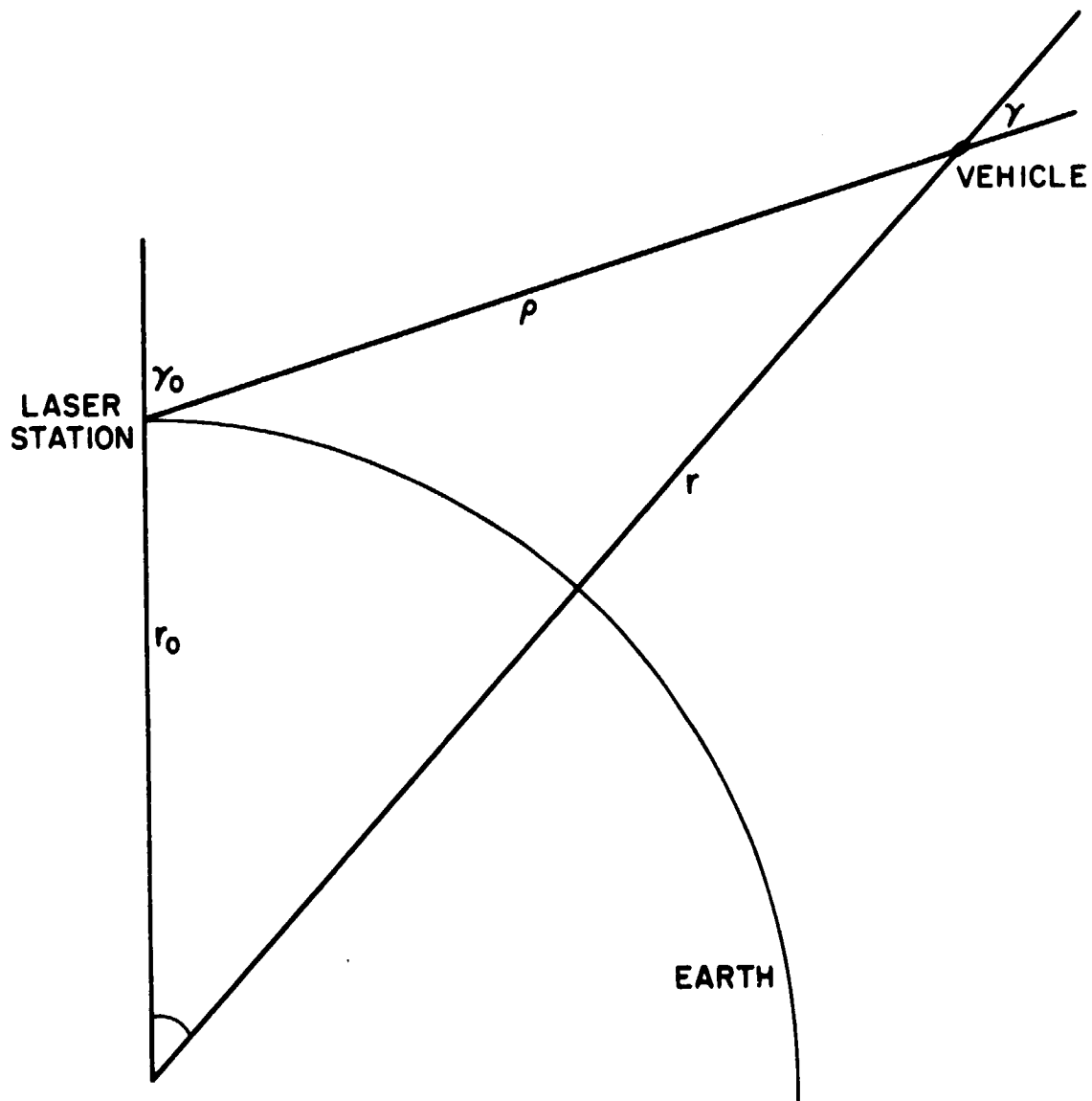
Fig. A-1   Rectilinear Trajectories

G3511

APPENDIX B

GLOSSARY OF SYMBOLS

SECTION II

Symbol

a	specific force (force per unit mass)
c	exhaust velocity
g	acceleration due to gravity (9.81 m/sec^2)
g	component of gravitation along trajectory
m	instantaneous mass of vehicle
m_o	lift-off mass of vehicle
m_1	burnout mass of vehicle
$\dot{m}$	rate of change of vehicle mass
P	exhaust power
R_1, R_2	mass ratio
r_o	radius of earth, 6378 nm
r	geocentric radius
t	time
$\dot{v}$	acceleration
v_1	burnout velocity
V_{co}	low circular orbit velocity (7.91 km/sec
γ	flight path angle
ρ_1	range at burnout
τ	duration of boost
μ	gravitational constant of Earth, 3.99×10^{14} m^3/sec^2

SECTION III

Symbol

A	cross ectional area
A_t	nozzle throat area
A_w	wall area
c	exhaust velocity
$\bar{c}_p$	mean constant-pressure specific heat
c_v	constant-volume specific heat
D_{12}	binary diffusion coefficient
$\bar{d}$	effective collision diameter
d_t	nozzle throat diameter
E_i	internal energy of species i
F	thrust
G_F	thrust coefficient
H_c	total enthalpy in thrust chamber
H_w	wall thermal conductance
h	Planck's constant
h_c	enthalpy/unit mass in chamber
h_e	enthalpy/unit mass at exit plane
h_i	enthalpy/unit mass of species i
I	flux density
I_c	chamber mirror flux density
J	heat flux
J_w	wall heat flux
k	Boltzmann's constant
k_i	mass fraction of species i

Symbol

L	chamber length
L_e	Lewis number
l_2	length of window isolation tube divided by length of chamber
M_i	molecular weight of species i
M_s	molecular weight of seedant
$\dot{m}$	mass
m	mass flow rate
m_{12}	reduced mass
N_i	number density of species i
n_a	number density of atoms
n_m	number density of molecules, after dissociation
n_1	number density of molecules, before dissociation
P_e	exhaust power
P_o	laser power
P_w	power lost to walls
p_s	seedant partial pressure
P_c	chamber pressure
P_1	propellant partial pressure, before dissociation
P_2	propellant partial pressure, after dissociation
p_i	partial pressure of species i
R	gas constant
T	temperature
T_b	$h\nu/k$
T_i	ionization temperature
T_v	vibrational energy temperature

Symbol

T_d	dissociation energy temperature
T_w	wall temperature
T_s	coolant temperature
V_c	chamber volume
$\langle v \rangle$	average thermal velocity
x_F	position of focus
y	absorption length
y_c	chamber radius
β	fractional ionization
β	fractional dissociation
Γ	flux concentration factor
γ	ratio of specific heats
η	efficiency
λ	thermal conductivity
μ	viscosity
ν	laser frequency
ρ	density

1. Report No. NASA CR 135129	2. Government Accession No.	3 Recipient's Catalog No.
4. Title and Subtitle Laser Absorption Phenomena in Flowing Gas Devices		5. Report Date June 1976
		6. Performing Organization Code
7. Author(s) P. K. Chapman and J. H. Otis		8. Performing Organization Report No.
9. Performing Organization Name and Address Avco Everett Research Laboratory Everett, MA 02149		10. Work Unit No. YOR6569
		11. Contract or Grant No. NAS3-18559
12. Sponsoring Agency Name and Address NASA Lewis Research Center 21000 Brookpark Road Cleveland, Ohio 44135		13. Type of Report and Period Covered Final Report
		14. Sponsoring Agency Code 6344 301-2

15. Supplementary Notes

Project Manager, Stephen M. Cohen, Laser Systems Section, NASA Lewis Research Center, Cleveland, OH

16. Abstract

A theoretical and experimental investigation is presented of inverse Bremsstrahlung absorption of CW CO_2 laser radiation (wavelength 10.6 μm) in flowing gases seeded with alkali metals. In order to motivate this development, some simple models are described of several space missions which could use laser-powered rocket vehicles. Design considerations are given for a test cell to be used with the Avco Everett Research Laboratory, Inc., HPL-10 welding laser, using a diamond window for admission of laser radiation at power levels in excess of 10 kW. A detailed analysis of absorption conditions in the test cell is included. The experimental apparatus and test set-up are described and the results of experiments presented. Injection of alkali seedant and steady-state absorption of the laser radiation were successfully demonstrated, but problems with the durability of the diamond windows at higher powers prevented operation of the test cell as an effective laser-powered thruster. Improved designs for diamond window holders are now available and should be used in future experiments of this type.

17. Key Words (Suggested by Author(s)) Plasma Seeding Plasma Absorption Laser Breakdown Laser Propulsion Laser Windows	18. Distribution Statement Unlimited		
19. Security Classif. (of this report) Unclassified	20. Security Classif. (of this page) Unclassified	21. No. of Pages 114	22 Price*

* For sale by the National Technical Information Service, Springfield, Virginia 22161

NASA-C-168 (Rev. 10-75)